UNIVERSITY OF CALIFORNIA

RIVERSIDE

A Measurement of $t\bar{t}$ Production Cross Section in $p\bar{p}$ Collisions at $\sqrt{s} = 1.8$ TeV Using Neural Networks

A Dissertation submitted in partial satisfaction

of the requirements for the degree of

Doctor of Philosophy

in

Physics

by

Harpreet Singh

December, 1999

Dissertation Committee:

Professor Stephen Wimpenny, Chairperson

Professor John Ellison

Professor Richard Seto

The Dissertation of Harpreet Singh is approved:

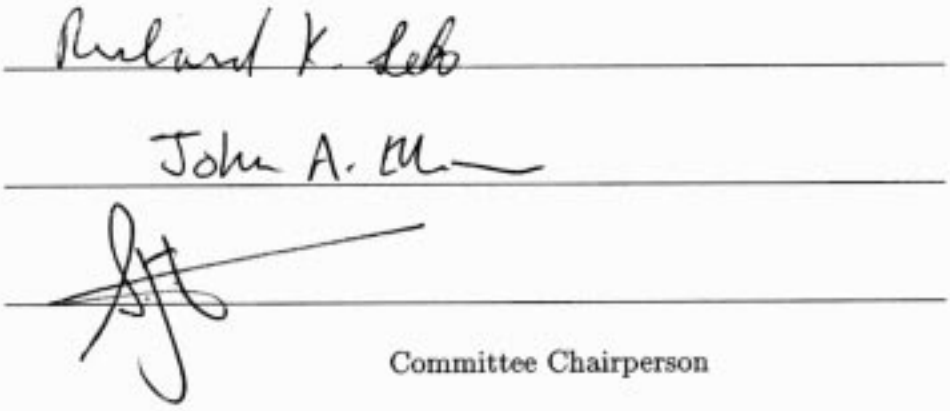

Committee Chairperson

University of California, Riverside

This work is supported by the United States Department of Energy under the grant number DE-FG03-94ER40837.

I dedicate this dissertation to my parents who gave me life and dreams.

Acknowledgments

It is matter of great pleasure for me to reach somewhere in life where I can thank all the people who influenced my life in one way or other. I would like to express my particular thanks to my supervisor, Professor Stephen Wimpenny who has been guiding and generously supporting my efforts during graduate school. The stories of his intelligence, hard work and dedication always inspired me. I would also like to acknowledge his assistance in reading and correcting this manuscript.

Taste, experience and judgment in experimental high energy physics come slowly with time. Working in big experiment like DØ has been a fascinating experience for me. I am greatly indebted to my collaborators for building and operating the DØ detector and to all the staff of Fermilab for the excellent quality of their work in running the Tevatron. Many thanks to Professor P. Grannis, R. Raja, H. Montgomery and G. Fisk for their support.

My very special thanks go to Professor Jim Cochran for being a good friend and my advisor at Fermilab. I learnt a great deal from his knowledge and intuition about high energy physics. His patience in the pursuit of the beauty of physics have always been an example for me.

I am thankful to Professor J. M. Kohli, Dr. S. Beri and Dr. J. B. Singh of the high energy group at Panjab University where I started my research career. Thanks to the faculty and staff of Tata Institute of Fundamental Research, Mumbai for helping me learn detector hardware.

I am greatly indebted to Dr. Pushpa Bhat and Professor Harrison Prosper for their everyday help in clearing my concepts for this analysis. Their contributions to Neural Network analyses in DØ are immeasurable. I am also thankful to Herb Greenlee for all the help he provided. I want to express my utmost gratitude to Professor Tom Ferbel for his comments on analysis and the wonderful St. Croix summer school. Special thanks to Dhiman Chakraborty for providing many useful suggestions and ideas.

At Riverside, I would like to thank Professor John Ellison, Ann Heinson and Krish Gounder for providing a rich environment for high energy physics research. I owe Mrs. Yvonne Ayers an incredible amount of thanks for the countless time she has helped me with administrative work, often putting aside her crushing workload. Also my fellow graduate students at Riverside, Martin and Patrick, have been great and supportive friends.

At Panjab, I have enjoyed the company of fellow students, Vipin and Raman. Many thanks to my friends Satish, Avinash and my M.Sc. class fellows Amit, Sanjay, Pardeep, Manish, Baldy, Yoga, Manu and Sunil for all the fun we shared.

During my stay at Riverside I met some wonderful people. I can't forget the time spent with Jason, Tabitha and Greg. I remember those days (nights) when we

studied for qualifying examinations and the day Tabitha cried when I left for Fermilab (that touched me a lot). Jason deserves a special mention here for being my beer/wine/whiskey buddy. I would also like to thank Tora, Esmeal, Brian, Michelle, Kim, Gretchen, Nils and Nick for being very good friends.

My stay at Fermilab was made enjoyable by lot of people. Mrinmoy, Bornali, Prem and Prajakta were always there for me and fed me with lots of good food. Mrinmoy and Sailesh always helped and shared their knowledge of physics with me. An advice from Brajesh was always valuable. Thanks to Dhiman, Shankar, Satyadev, Ashutosh, Jeff, Wendy, Emanuela, Frederic, Vishnu, Scot, John Rha and Suyong for keeping my spirits up. I very much appreciated the presence of my office neighbors Darien, Pierrick, Neeti, Steve and Matt.

I am thankful to my swimming coaches and water-polo team who taught me how to fight and win.

Finally, I would like to express my gratitude to my parents Jagdev and Ranjit, uncle Mohinder, aunt Amrit and my brothers Manjeet and Darshan for their love and support. I am also thankful to my sister Gurdip and brother Manjinder for their support. My parents have always encouraged and inspired me to achieve high in academics. This dissertation would not have been possible without them. My last special thank goes to my fiancee Navgeet who came as a new song in my life.

September, 1999 Harpreet Singh

Main Entry: **quark**
Pronunciation: kwôrk, kwärk
Function: *noun*
Etymology: coined by Murray Gell-Mann
Date: 1964
: Any of several elementary particles that are postulated to come in pairs (as in the up and down varieties) of similar mass with one member having a charge of + 2/3 and the other a charge of - 1/3 and are held to make up hadrons

Abstract of the Dissertation

A Measurement of $t\bar{t}$ Production Cross Section in $p\bar{p}$ Collisions at $\sqrt{s} = 1.8$ TeV Using Neural Networks

by
Harpreet Singh
Doctor of Philosophy, Graduate Program in Physics
University of California, Riverside, December, 1999
Professor Stephan Wimpenny, Chairperson

We present the results of a new measurement of the $t\bar{t}$ production cross section using $e\mu$ channel in $p\bar{p}$ collisions at $\sqrt{s} = 1.8$ TeV. This study corresponds to an integrated luminosity of 108.3 ± 5.7 pb^{-1} acquired by the DØ detector during the Fermilab Tevatron Collider Run I (1992-1996). By using neural network techniques instead of the conventional analysis methods, we show that the signal acceptance can be increased by 10% (for $m_t = 172$ GeV/c^2) while the background remains constant. Four $e\mu$ events are observed in data with an estimated background of 0.22 $\pm$ 0.14 corresponding to a $t\bar{t}$ production cross section of 9.75 $\pm$ 5.53 pb.

Contents

List of Tables

List of Figures

Preface

In fundamental research, the most basic question one can ask is "What is matter made up of?" Had no one asked this question, or similar ones, we would not now have transistors, the laser, nuclear energy and many other practical developments. Researchers worked long and hard, merely to satisfy their scientific curiosity. Much of their work has consisted of breaking open matter just to see what is inside, and perhaps grinding it up for a good measure. This scientific curiosity gave birth to High Energy Physics, which is more commonly referred to as Particle Physics.

Intensive and vigorous research in the past few decades by scientists throughout the world has resulted in tremendous advancement in this field. The study proceeds by probing the structure of matter, from molecules to atoms to nuclei to proton/neutron to quarks. The most powerful microscopes is still far above even the size of atom. In order to reach down into the interior of the nucleus, we need "microscopes" which can resolve objects which are as close as 10^{-13} cm apart. High energy particles from cosmic rays and particle accelerators are the only things which can penetrate into this sub-nuclear domain. The first particle accelerators built in 1930's were very different in size and capability from their modern counterparts. Today these machines are huge in size, often miles in length, and they are high in cost both in terms of money and the highly skilled technical manpower needed to run them.

This dissertation is devoted to the analysis of High Energy Physics data collected at Fermi National Accelerator Laboratory (Fermilab) with the D-Zero (DØ) detector. The Fermilab accelerator is the most powerful particle accelerator in the world. It consists of two rings of conventional and super-conducting magnets, four miles in circumference, which are used to collide highly relativistic beams of protons and anti-protons. Collisions occur at two points in the accelerator ring, each of which is surrounded by a massive piece of detection apparatus, which is used to study the results of these collisions. The DØ detector, located at one of the collision points is a multipurpose collider detector with almost 4π coverage. This is maintained and operated by an international collaboration of 400 physicists from 45 institutes around the world.

The DØ apparatus was designed to explore an energy regime which had not been explored in earlier experiments. Its goals were to search for the evidence of

new massive particles and to test the modern theory of particle physics known as the Standard Model. A major triumph came in 1995 when DØ experiment together with the CDF experiment (situated at the second interaction region at Fermilab) made the joint announcement of the discovery of a new quark, known as the top quark.

The subject of this dissertation is a measurement of the production cross section of the $t\bar{t}$ pairs at $\sqrt{s} = 1.8$ TeV. The analysis used artificial neural network logic instead of the conventional methods used in previous studies. These are multivariate analysis tools with the potential to give excellent signal to background discrimination in complex environments. They have been used previously with great success in the analyses of large cross section processes and for particle identification. This is the first analysis to attempt their application to the dilepton decays of a $t\bar{t}$ pair.

The dissertation is arranged as follows. Chapter 1 gives a brief introduction to the field of High Energy Physics and a sketch the present day theory of the fundamental particles and forces of nature. Chapter 2 focuses on the significance of the top quark and how it is produced and decays in the $p\bar{p}$ environment. This chapter discuss the signal and relevant background to the production of $t\bar{t}$ process studied for this dissertation. Chapter 3 gives a brief overview of the Fermilab accelerator complex and the apparatus at DØ where the measurements were performed. Chapter 4 describes the process of event reconstruction and particle identification. The basic concepts and theorems of neural networks are discussed in Chapter 5. In Chapter 6, we define the data samples, detection efficiencies and Monte Carlo simulations used in our study. In Chapter 7, we explain the training and optimization of neural networks we used in the study and describes the neural network analysis. Chapter 8 compares the results of this analysis to the conventional style analysis. Finally, Chapter 9 summarizes the results and conclusions of the study.

Chapter 1

The Riddle of Matter

...This supreme science was thus received through the chain of disciplic succession.

- Bhagavad Gita

1.1 From Antiquity to the 20th Century

Some tens and thousands of years ago, when ancient man created tools for his needs, he had to experiment with various materials and configurations, such as different kinds of wood and stone for bows and arrows and useful arrangements for traps to achieve success. Thus, it was necessary that he perform research tasks to satisfy certain needs. His curiosity motivated him to accumulate information from observations and this led him to ask questions such as why the universe exists and of what it is made up of.

The ancient Indians, believed in five elements: space, earth, air, fire, and water. Likewise, the ancient Chinese counted five fundamentals: earth, wood, metal, fire, and water. Similarly, ancient Greeks chose: air, fire, water, and earth as the four basic elements. At some point, people began to think that things were made up of microscopic particles called atoms. About 600 B.C., an Indian philosopher named Kanada formulated some ideas about the atom. These were further pursued by the Greek philosophers Leucippos and Democritus (about 400 B.C.), who argued that everything consists of tiny atoms - a bone is made of bone-atoms, wood is made of wood-atoms, and so on. Much later, scientists began to understand some of the underlying patterns to the structure of matter and the field of chemistry was born. Atoms (not Democritus's kind) were first grouped into a periodic table by Dmitri Mendeleyev between 1869 and 1871. By arranging the elements in a specific way, many of their physical and chemical properties could be predicted quite accurately.

By the end of the nineteenth century it was recognized that the atoms of

chemical elements were not indestructible and could be modified or perhaps even broken up if heated enough. The problem was to find right method of heating atoms. The answer was found in the newly discovered science of electricity. German physicists, Plücker, Hittorf and Goldstein learnt to pull atoms apart into two components by causing electric discharge in low-pressure gases. J. J. Thomson in England then studied the two parts and found in 1897 that one part consists of negatively charged particles called electrons.[1] He identified the other component as positively charged particles more massive than the electron. The lightest of these heavy positive particles, called the proton, is the heavy part of the hydrogen atom.

In 1911, Ernest Rutherford showed from his experiments that the heavy positive part is the center of the atom (nucleus) and it is surrounded by a number of negatively charged particles (electrons) which orbit around it and are bound to it by the electro-magnetic force. Soon afterwards, the Danish physicist Niels Bohr built a mathematical description of the atom using the Planck's theory of quantization of energy. In his model, electrons move around the nucleus in fixed orbits and can only switch between orbits when a certain discreet amount of energy is absorbed or emitted. This amount of energy is the energy of the photon of specific wavelength. The picture of atom became more transparent, when Heisenberg in Germany predicted that a neutral heavy counterpart of the proton should exist. In 1932, Chadwick in England discovered this particle which he called the neutron.

The existence of positron (e^+) was predicted by Paul Dirac in 1928. This is the anti-particle of electron- a particle with the same mass but opposite electric charge. This was established in experimentally 1933 and was followed shortly afterwards in 1938 by another charged particle, the muon (μ) which has mass 206 times larger. The energy loss problem in radioactive β decay was solved by the Italian, Enrico Fermi, who predicted a new particle called the neutrino, which was later observed in 1947 in cosmic ray experiments.

By the middle of twentieth Century, only a few elementary particles namely the electron, proton, neutron, photon, muon and neutrino were known. These are the building blocks of our universe. However, the study of cosmic rays and the nuclear force led to the inference of new elementary particles which were not needed to build matter. This led to the construction of particle accelerators and the subsequent observation of many hundreds of new particle states. These states were called "hadrons", meaning heavy, and were further divided into lighter "mesons" and heavier "baryons".

The increasing number of hadrons suggested that there was something more fundamental than the hadrons. In 1964, Murray Gell-Mann and George Zewig proposed the static quark model [1]. In this picture the hadrons are made out of three more fundamental constituents called *quarks*, which come in three types called up,

[1]The existence of the electron and the name had been first suggested by Stoney in 1874, also in England.

down and strange (u, d and s). The quarks are believed to be bounded together inside the hadrons by the exchange of quanta of strong interaction known as "gluon". The static quark model was very successful in explaining the known "hadronic" particle states. It was further supported by the first results from a new accelerator at SLAC in the early 1970s which demonstrated the existence of a internal structure to the proton and neutron.

In 1974, a new particle called the tau (τ) was discovered at SLAC. This together with electron (e), muon (μ) and three corresponding types of neutrinos (ν_e, ν_μ, ν_τ[2]) form a different family of the fundamental particles which are collectively known as *leptons*. The charged leptons interact via the electro-magnetic and weak interactions, while neutrinos are distinguished by having only weak interactions. The unification of electro-magnetic and weak interactions by Weinberg, Glashow and Salam [2] predicted the existence and masses of the bosonic particles (W^+, W^- and Z^o) believed to be the mediators of electroweak force. This picture was verified in 1984 when these particles were discovered by the CERN S$\bar{p}p$S collider experiments UA1 and UA2 [3].

Since the static quark model was proposed, three more quarks have been discovered, the charm (c) quark in 1974, the bottom (b) quark in 1977 and the top (t) quark in 1995 [4]. The theoretical picture that describes how these elementary particles are organized and how they interact with one another via the forces is known as the Standard Model.

1.2 The Standard Model

Over the last century the field of particle physics had developed through the efforts of experimentalists and theorists. The physical world we live in, is governed by four fundamental forces:

1. Electro-magnetic force
2. Weak force
3. Strong force
4. Gravitational force

High energy physics is concerned with the first three of these. Gravity is so much weaker than the other three that it has no influence on subatomic processes and can be excluded from the following discussion.

There are two basic types of particles in the Standard Model: fermions and bosons. The fermions have spin $\frac{1}{2}$ and are the building blocks of matter. These adhere to the Pauli Exclusion principle so that only one fermion can occupy a particular quantum state. The bosons are either spin 0 or 1 particles and are believed to be the carrier of the force between the particles. The fermionic constituents in

[2] ν_τ has not been directly observed yet.

the Standard Model are further divided into quarks and the leptons. The leptons interact via electro-magnetic and weak force and the quarks engage in the strong interaction as a consequence of their color charge.[3]

In the case of the strong and electro-magnetic interactions the bosons are massless whereas the weak interaction they are quite massive ($M_W \approx 80$ GeV, $M_Z = 91$ GeV). The eight gluons (strong interaction), the photon (electro-magnetic) and the W and Z (weak interaction) are assumed to be elementary. There is no experimental evidence for quark and lepton compositeness, such as excited states and form factors and so these are also assumed to be the fundamental particles.

Table 1.1 and Table 1.2 summarize the properties of the particles of the Standard Model. Mass values are in units of GeV/c^2 and electric charges are given as multiples of the proton charge e.

The Standard Model Lagrangian embodies our knowledge of the strong and electroweak interactions. It contains as fundamental degrees of freedom: the quarks and leptons, the spin 1 gauge bosons and a spin 0 Higgs field.[4] Symmetry plays the central role in determining its dynamical structure. The Lagrangian exhibits invariance under $SU(3)$ gauge transformations for the strong interactions and under the $SU(2) \otimes U(1)$ gauge transformations for the electroweak interactions. Thus, the gauge group for the Standard Model is $SU(3)_C \otimes SU(2)_L \otimes U(1)_Y$ [5].

The weak isospin complex doublet of spin-zero Higgs fields $\Phi = \binom{\phi^+}{\phi^0}$ with the potential function:

$$V(\Phi) = \mu^2(\Phi^\dagger\Phi) + |\lambda|(\Phi^\dagger\Phi)^2. \tag{1.1}$$

breaks the electroweak and flavor symmetry in the Standard Model. Here λ is the self interaction(coupling) of the Higgs scaler field. Mass generation for fermions and gauge bosons proceeds by means of spontaneous breaking of the $SU(2)_L \otimes U(1)_Y$ symmetry. The potential V of Equation 1.1 is minimized to obtain ground state Higgs configuration.

$$\Phi(\mu^2 + 2\lambda\Phi^\dagger\Phi) = 0 \tag{1.2}$$

The Equation 1.2 has two solutions, the trivial solution $\langle\Phi\rangle_0 = 0$ and the nontrivial solution

$$\langle\Phi^\dagger\Phi\rangle_0 = -\frac{\mu^2}{2\lambda} = \frac{v^2}{2} \tag{1.3}$$

with

$$v = \sqrt{\frac{-\mu^2}{\lambda}} \tag{1.4}$$

[3]Each quark carries a quantum number called color, There are three such quantum numbers namely red, blue and green

[4]Higgs boson is not observed yet.

[5]C is the color quantum number, L denotes left handed group and Y is the hypercharge.

Generation	Particle Name	Mass (GeV/c^2)	Charge (e)	Force
	Quarks (spin 1/2)			
1	Down (d)	0.005	$-1/3$	Strong, EM, Weak
	Up (u)	0.01	2/3	Strong, EM, Weak
2	Strange (s)	0.2	$-1/3$	Strong, EM, Weak
	Charm (c)	1.5	2/3	Strong, EM, Weak
3	Bottom (b)	4500	$-1/3$	Strong, EM, Weak
	Top (t)	173.8	2/3	Strong, EM, Weak
	Leptons (spin 1/2)			
1	Electron (e)	5.1×10^{-4}	-1	EM, Weak
	Electron neutrino (ν_e)	$< 0.8\times10^{-8}$	0	Weak
2	Muon (μ)	0.105	-1	EM, Weak
	Muon neutrino (ν_μ)	$< 2.7\times10^{-4}$	0	Weak
3	Tau (τ)	1.777	-1	EM, Weak
	Tau neutrino (ν_τ)	< 0.035	0	Weak

Table 1.1: The particles of the Standard Model-the Fermion Sector

Particle	Name	Mass (GeV/c^2)	Charge (e)	Force
Gauge Bosons (spin 1)				
γ	Photon	0	0	Electro-magnetic
g	Gluon	0	0	Strong
W	W	80.2	1	Weak
Z	Z	91.2	0	Weak
Fundamental Scalar (spin 0)				
H	Higgs	?	?	Couples to matter

Table 1.2: The particles of the Standard Model-the Boson Sector

Choosing μ^2 to be negative would make the nontrivial solution of Equation 1.3 real and this equation not only respects the conservation of charge but also spontaneously breaks the $SU(2)_L \otimes U(1)_Y$ symmetry.

A consequence of the spontaneous breaking of the electroweak symmetry is that the $W^{\pm}$ and Z^0 acquire mass according to:

$$M_W^2 = \frac{\pi\alpha}{G_F\sqrt{2}\sin^2\theta_W} \tag{1.5}$$

$$M_Z^2 = \frac{M_W^2}{\cos^2\theta_W} \tag{1.6}$$

whereas photon remains massless ($M_\gamma = 0$). This also gives rise to a spin 0 (scalar) particle called the Higgs boson. In Equation 1.5, G_F is the Fermi (weak) coupling constant, α is the fine structure constant and θ_W is the weak mixing angle. Each of the fermions (f, lepton and quark) has its own Yukawa coupling (G_f) to the Higgs boson. Thus, the fermion mass is given by

$$m_f = \frac{v}{\sqrt{2}}G_f \tag{1.7}$$

The value of v is given by $v = \sqrt{-\mu^2/\lambda} = (G_F\sqrt{2})^{-\frac{1}{2}} = 246$ GeV. Although the theory can accommodate fermions of any mass, it does not predict the mass values. Instead, the measured fermion masses are used to fix the arbitrary Higgs-fermion (Yukawa) coupling.

The Standard Model has been extremely successful so far [5]. Despite intense experimental scrutiny, this theory has displayed no experimental inconsistencies. However, the Standard Model does have several features which many physicists consider unsatisfactory. There exists no understanding of the number of families and the presence of so many free parameters (nine fermion masses, three coupling coefficients, four CKM matrix elements and one Higgs boson mass). Hence, physics beyond the Standard Model seems inevitable [6]. The mass of the top quark [7] suggests that its Yukawa coupling (G_f) to Higgs boson is ~ 1 (see Equation 1.7). It is quite possible that the top quark might provide a window to the new physics.

Chapter 2

The top quark

The truth is out there.

- The X-files

2.1 Why do we need the sixth quark?

The tau lepton (τ) was the first particle of third generation particles to be discovered [8]. Shortly afterwards, the Υ was discovered at Fermilab as a resonance in the $\mu^+\mu^-$ invariant mass spectrum [9]. This was interpreted as a $b\bar{b}$ bound state which subsequently decays into $\mu^+\mu^-$. The bottom (b) quark is a third generation quark. In the past few years a tremendous amount of experimental data on its properties has been collected. Both its charge ($Q_b = -\frac{1}{3}$) and isospin ($I_3 = -\frac{1}{2}$) are well established.

The first measurement of the charge of the b quark was done by measuring the leptonic width of the Υ resonance at the DORIS e^+e^- storage ring [10]. The Υ leptonic width is proportional to the square of the charge of the b quark. From these measurements, it was found to be $Q_b = -\frac{1}{3}$.

The weak isospin of the b quark was first determined from the measurement of forward-backward asymmetry (A_{FB}) in $e^+e^- \to b\bar{b}$ production. The definition of the asymmetry in terms of the production cross section (σ_b) is:

$$A_{FB} = \frac{\sigma_b(\theta > 90^o) - \sigma_b(\theta < 90^o)}{\sigma_b(\theta > 90^o) + \sigma_b(\theta < 90^o)} \tag{2.1}$$

where θ is the polar angle of the quark in the e^+e^- center of mass as measured from the direction of the e^-.

The production of $b\bar{b}$ pairs in e^+e^- collisions can be either mediated by a photon (γ) or a Z boson (see Figure 2.1). The contributions of the photon (γ) exchange to the angular distributions are symmetric. An asymmetry arises through

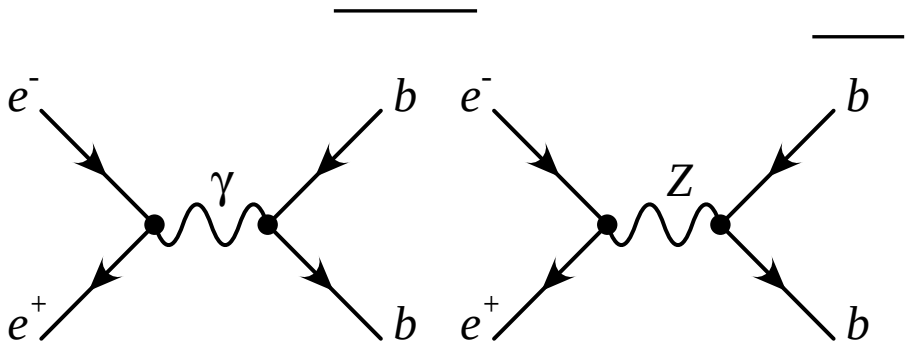

Figure 2.1: Feynman diagrams for $e^+e^- \to b\bar{b}$ via γ and Z exchange.

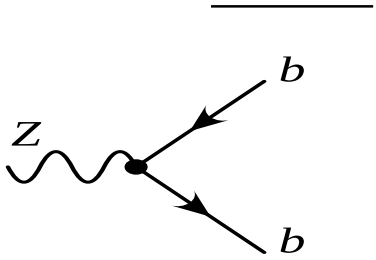

Figure 2.2: Feynman diagram for $Z \to b\bar{b}$.

the Z contributions (see Figure 2.2) because of the coupling of the Z boson to fermions, which depend on the weak isospins of the leptons. This arises through a term in the Lagrangian of the form $\bar{f}\gamma_\mu(g_V - g_A\gamma_5)Z^\mu f$, where γ_5, γ_μ are Dirac matrices, f is fermion field and g_V, g_A are the vector and axial couplings which are given by

$$g_V = 2[I_3^L(f) + I_3^R(f)] - 4Q_f \sin^2\theta_W \tag{2.2}$$

$$g_A = 2[I_3^L(f) + I_3^R(f)] \tag{2.3}$$

where $I_3^L(f)$ and $I_3^R(f)$ are the isospins for left-handed and right-handed fermion field, θ_w is the Weinberg angle and Q_f is the charge of the fermion.

The measurements of A_{FB} were found to be consistent with the Standard Model predictions assuming $I_3 = -\frac{1}{3}$ for the weak isospin of the b quark [11]. If the b quark is an $SU(2)$ weak-isospin singlet state, it cannot decay via the charge current (W) because it won't have charge current interactions. The other decay mode would be a flavor-changing neutral current (FCNC, $(b \to s(Z/\gamma) \to sl^+l^-)$. FCNC decays are suppressed for the isospin doublet quarks by GIM mechanism [12]. If the b quark is a isospin singlet state then FCNC decays should be observed at a rate well above the present experimental limits [13]. However, the charge current decay is readily observed leading to the conclusion that the b quark must be a member of

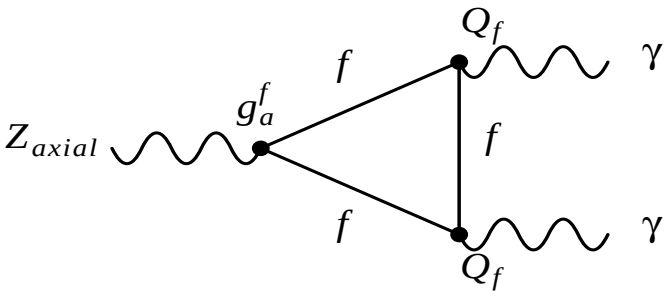

Figure 2.3: An example of the fermion diagram which give rise to chiral anomalies in the Standard Model; f is a fermion, Q_f is a fermion charge, g_a^f is fermion axial coupling to Z.

weak isospin doublet.

The establishment of a third generation isospin doublet implies the existence of an additional quark which is referred to as the top (or truth) quark (t). Furthermore, the renormalizablity of electroweak sector in the Standard Model requires cancellations of the triangle anomalies which arise from the diagram shown in Figure 2.3. The contribution of this diagram for each fermion is $n_c \times g_a^f \times Q_f^2$, where $n_c = 3$ for quarks. Equation 2.4 implies that the net contribution from a isospin doublet is zero, thereby avoiding the problem.

$$Q_f = -1 + 3 \times \left[\left(\frac{2}{3}\right) + \left(-\frac{1}{3}\right)\right] = 0 \tag{2.4}$$

There is other indirect experimental evidence which indicates the existence of top quark. The observed rate of $B_d^o - \bar{B}_d^o$ mixing is proportional to $\mid V_{td} \mid^2$, the Cabibbi-Kobayashi-Maskawa (CKM) matrix element for the t and d quark coupling [14, 15]. This implies that a massive top quark is needed in the loops so that the b quark can decay indirectly via an intermediate state containing a virtual t quark to the d quark. This indicates that the b quark has a weak isospin partner, the top quark with weak isospin $I_3 = +\frac{1}{2}$.

The precise measurements of Z width by experiments at the LEP and SLAC rule out the existence of fourth generation neutrino with a mass $M_\nu \leq M_Z/2$ [16]. Thus, unless the additional neutrinos are really massive, no additional generations in the Standard Model are allowed. Thus, the top quark is the last fermion expected in the minimal Standard Model.

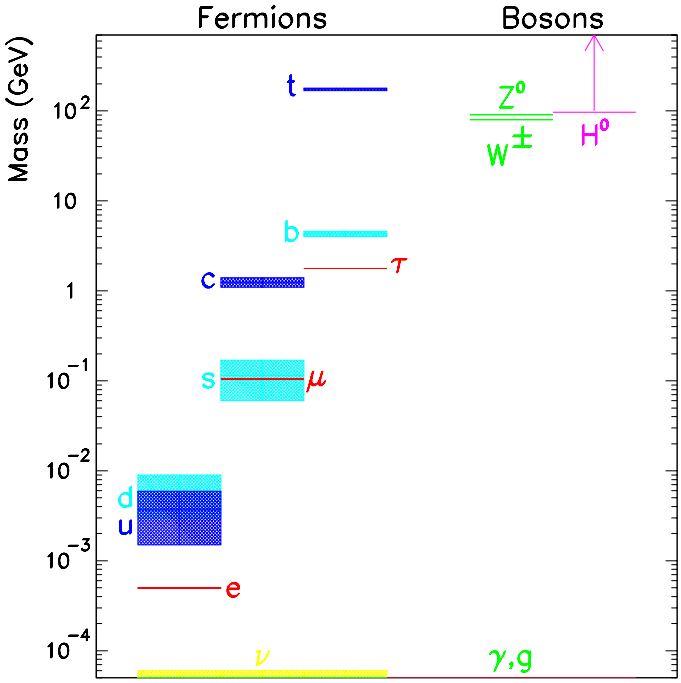

Figure 2.4: The Standard Model particle masses on logscale.

2.2 What is special about the top quark?

The Standard Model predicts the weak isospin ($I_3 = +\frac{1}{2}$) and charge ($Q_t = +\frac{2}{3}$) of the top quark but its mass remains as a free parameter in the model. The most recent measurements of the top quark mass yield $m_t = 174.3 \pm 5.1$ GeV/c^2 [17]. This a factor 40 higher than the mass of the b quark, the second heaviest fermion and almost a factor of two higher than the mass of the heaviest of the known bosons the Z^0. The masses of the particles of the Standard Model are shown in Figure 2.4. It is quite clear that its large mass sets the top quark apart.

The value of the top quark mass (m_t) enters in numerous calculations of radiative corrections to the electroweak sector in the Standard Model. The parameters α, G_F and θ_W determine the mass of weak vector bosons ($W^\pm, Z^0$) to the lowest order (see Equations 1.5, 1.6). However, the higher order radiative corrections such as those shown in Figure 2.5 depend on the mass of both the top quark and Higgs boson. One such correction is:

$$\Delta\rho = \frac{n_c g_2^2}{64\pi^2 M_W^2}\left[m_t^2 + \frac{M_W^2}{3}\left[\frac{11}{3}\ln\left(\frac{M_H^2}{M_W^2}\right) + \ldots\right] + \ldots\right] \tag{2.5}$$

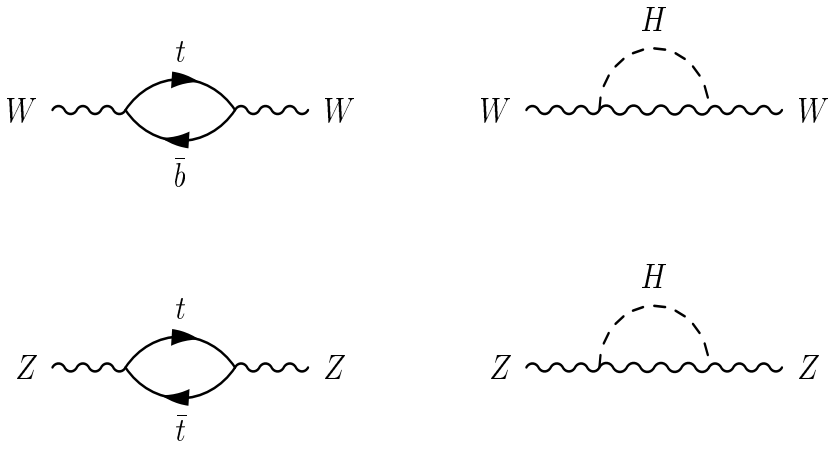

Figure 2.5: Diagram of radiative corrections to $W^{\pm}$ and Z bosons with top quark and Higgs boson in virtual loops.

where $n_c = 3$ and $g_2^2 = \frac{8G_F M_W^2}{\sqrt{2}}$. The dependence of this radiative correction is quadratic in the top quark mass whereas the dependence on Higgs boson mass is logarithmic. Because of the large value of m_t, the term containing m_t is the dominant parameter in the electroweak radiation corrections. Equation 2.5 was used to set the constrains on the top quark mass before it was measured directly. Today, since m_t has been measured, the argument has been reversed and used to test electroweak theory.

The electroweak sector of the Standard Model predicts the relationship between m_t and the masses of the W boson (M_W) and the Higgs boson (M_H). A precise measurement of m_t and M_W can be used to obtain constrains on the mass of the undiscovered Higgs. However, because of the logarithmic dependence of the M_H and the accuracy of the present measurements, this can only set a weak constraint on M_H. This is shown in the Figure 2.6, where the two ellipses represent direct (solid) and indirect (dashed) measurements. The shaded bands are the Standard Model predictions for M_H values between 90 and 1000 GeV.

The top quark production cross section can be calculated using the perturbative QCD. Thus, a precise measurement of the cross section would both test the predictive power of the theory and be sensitive to new physics in the form of enhancements to the $t\bar{t}$ production cross section. Such effects are predicted in the color octet, top color and technipion models [18, 19].

The decay of the top quark provides an opportunity to study the properties of a bare quark such as spin correlations [20] which are free from the long range effects of the strong interaction. In $p\bar{p}$ collisions $t\bar{t}$ pairs are produced via spin 1 boson (γ, Z^0, gluon) exchange. The decay time of the top quark ($\approx 10^{-25}$sec) is less

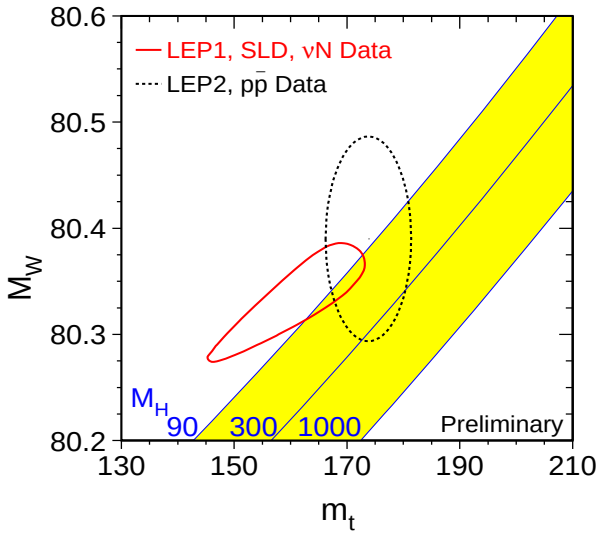

Figure 2.6: The dependence of the Higgs boson mass (bands from 90 to 1000 GeV/c^2) on the top quark mass (x axis) and the W boson mass (y axis). The contours represent the 68% (1σ) confidence level measurements.

than the QCD hadronization time-scale ($\approx 10^{-23}$sec). Thus, the spin correlation information is preserved and is reflected in the angular correlations of the decay products. Observing such correlations would confirm that the top quark has spin $\frac{1}{2}$ and that it decays before hadronizing, thereby giving a limit on the top quark lifetime. This could also be used to provide a lower bound on the CKM matrix element V_{tb} without imposing a three generation constraint [20].

Because of large mass of the top quark, it is quite possible that the new physics may manifest itself at the top decay vertex. Thus, the study of top quark production and decay is a excellent place to look for evidence of new particles such as stop, $\tilde{t}$ or charged higgs $H^{\pm}$ which exist in the extensions of the Standard Model. This can be done by comparing the ratios of the decays of the top quark with the Standard Model expectations. To date no such divergences have been observed.

The large top quark mass singles it out in several ways. It has a significant effect on electroweak physics and it may play a special role in the electroweak symmetry breaking.

2.3 Production Mechanism

Because of its large mass, the top quark can only be produced in the collisions of the particles where a sufficiently high center-of-mass energy ($\sqrt{s}$) can be achieved.

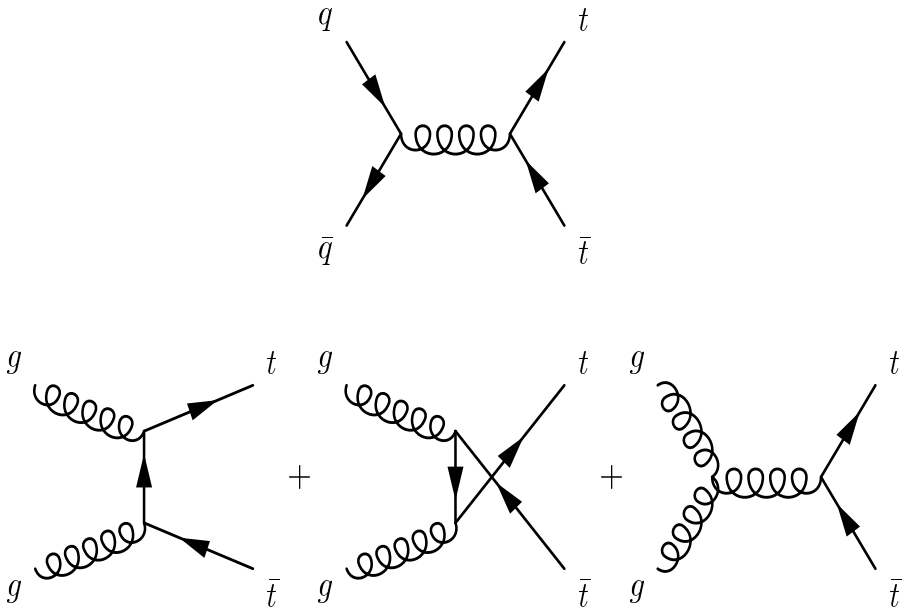

Figure 2.7: Feynman diagram for lowest-order $t\bar{t}$ production.

The proton-anti-proton ($p\bar{p}$) accelerator (the Tevatron) at Fermilab operating at $\sqrt{s}$ of 1.8 TeV is the only facility in the world where the top quarks can be and have been produced. It was here that the top quark was discovered in 1995 by the DØ and CDF experiments [4]. A new proton-proton (pp) collider called the LHC is under construction at the CERN laboratory at Geneva. With a center-of-mass energy of 14 TeV, this will be capable of producing the large number of top quark events when it comes on line in 2006. Top quark physics could also be pursued at other machines such as high energy e^+e^- and $\mu^+\mu^-$ colliders. However, these machines are still in the design stage and will not be available in the immediate future. For this dissertation, we focus on the features of the top quark production at Fermilab.

In $p\bar{p}$ collisions, there are two mechanisms for the top quark production. The pair production via strong interaction and single top production via electroweak interaction. These are discussed below:

1. Pair production of the top quarks ($t\bar{t}$ production):

Figure 2.7 shows the leading order processes which contribute to $t\bar{t}$ pair production at the Tevatron. At $\sqrt{s} = 1.8$ TeV, the $q\bar{q} \to t\bar{t}$ diagram dominates, contributing 90% of the total production cross section (see Figure 2.8). In principle, there are also $q\bar{q}$ diagrams with γ^* or Z^* propagators which could result in $t\bar{t}$ final states. However these are electroweak processes and the cross sections are much smaller.

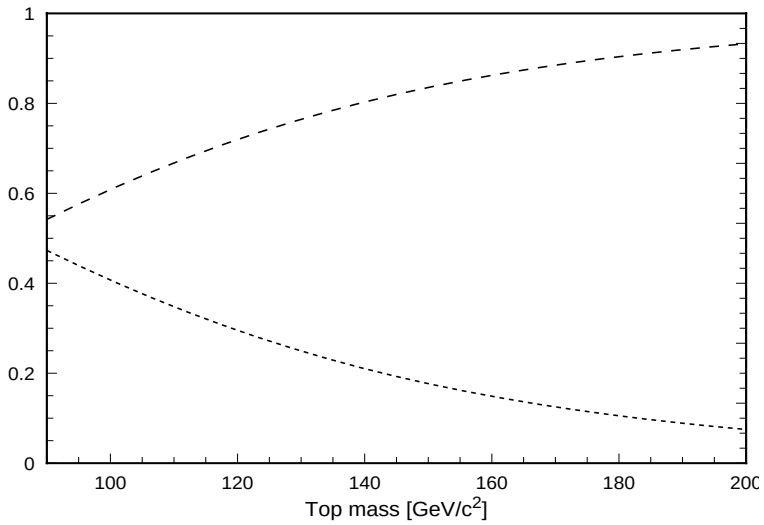

Figure 2.8: Fractional contributions of $q\bar{q}$ (dashed) and gg (dotted) NLO processes to the production of $t\bar{t}$ at $\sqrt{s} = 1.8$ TeV.

2. Single top quark production:

Single top quark production can occur through s, t or u-channel electroweak processes. At $\sqrt{s} = 1.8$ TeV, the dominant processes are s-channel production of a tb final state via off mass-shell W^* exchange and production of tqb final state via W-gluon fusion (see Figure 2.9). Although the single top production cross section is one third that of the $t\bar{t}$ production cross section [21], the detection efficiencies for single top quark events are lower and the signal is much more difficult to separate from the background. At this time there is no direct measurement of single top production cross section although some preliminary limits are available [22].

This thesis focuses on the study of the $t\bar{t}$ final state for which the detection efficiencies and the cross section are larger (see Figure 2.11).

2.4 Calculations of the $t\bar{t}$ production cross section

The production cross section for the $t\bar{t}$ process in $p\bar{p}$ collisions can be calculated in perturbative QCD. It can be written as a product of the parton distribution functions of the proton and the parton-parton point cross sections. This is then summed over all the contributions from the quark and gluon processes [23].

$$\sigma_{p\bar{p}\to t\bar{t}} = \sum_{a,b} \int dx_a F_a^p(x_a, q^2) \int dx_b F_b^p(x_b, q^2) \hat{\sigma_{ab}}(\hat{s}, q^2, m_t) \qquad (2.6)$$

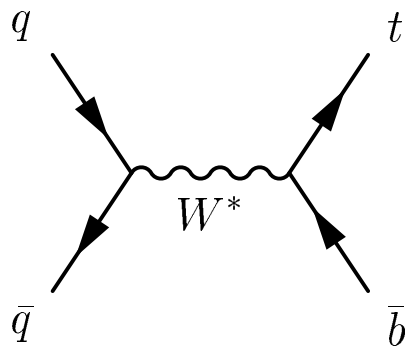

Figure 2.9: Feynman diagram for s-channel single top quark production.

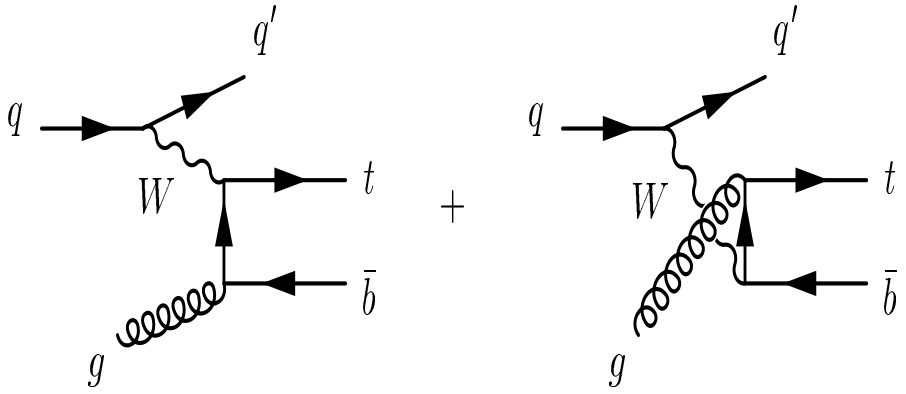

Figure 2.10: Feynman diagram for single top quark production via W-gluon fusion.

The functions F_a and F_b represents the probability densities of the light partons (u, d, s, c, b) which carry momentum fractions x_a and x_b respectively and are evaluated at scale q. $\hat{\sigma_{ab}}$ is the point cross section for the process $a + b \to t\bar{t}$ and $\hat{s} = 4x_a x_b$. While calculations to all orders of perturbative QCD would be independent of the choice of q, practical calculations are performed to a finite order so that the results can depend on the choice of the scale. This usually chosen to be $q \sim m_t$.

The first calculations of $\sigma_{t\bar{t}}$ in leading order (LO, $O(\alpha_s^2)$) were done in late 1970's [24]. About 10 years later, these were followed by the next-to-leading-order (NLO, $O(\alpha_s^3)$) calculations [25]. In perturbation theory, the NLO contribution should be small as compared to LO. However for $t\bar{t}$ production at the Tevatron the NLO contributions are still large because contributions from processes involving of soft gluon emission. This implies that still higher order calculations are needed to establish stability of the results. To incorporate these, a technique call *resummation* is used in which the dominant logarithms from soft gluon emission are calculated and summed to all orders in perturbation theory. This is problematic because the

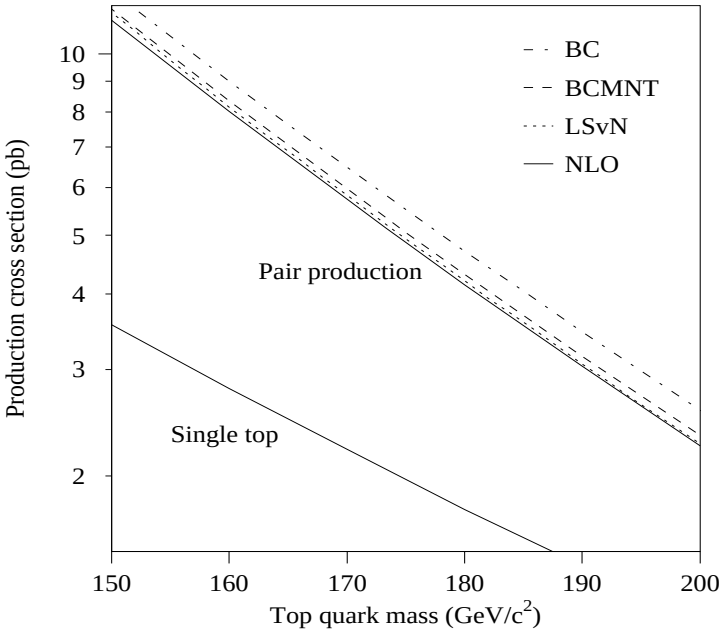

Figure 2.11: The $t\bar{t}$ and $t(\bar{t})$ production cross sections as a function of m_t at $\sqrt{s} =$ 1.8TeV.

re-summed series are divergent due to non-perturbative effects as α_s becomes large. The solution is to introduce a new scale, $q_0 >> \Lambda_{QCD}$, which can be used as a cutoff and removes the divergence. The first of these calculations were performed by Laenen, Smith and van Neerven (LSvN) [26]. Subsequent calculations was done using different techniques which avoid the need for the infrared cutoff, q_0 [27, 28]. Berger and Contopanagos (BC) [27] used a technique called principal value resummation (PVR) to include the resummation of gluon radiative correction, whereas Bonciani, Catani, Mangano, Nason and Trentadue (BCMNT) [28] used a slightly different scheme to avoid the divergence. A full discussion on the differences between these calculations are given in references [27, 28, 29] and the results are compared in Figure 2.11. Table 2.4 composes the results for $m_t = 175$ GeV and summarizes the main features of the calculations.

2.5 Decay Kinematics

According to Quantum Chromodynamics (QCD), quarks are confined and are not observed as free particles [31]. For $m_t = 175$ GeV/c^2 the decay width of

Calculation	PDF	Order	$\sigma_{t\bar{t}}(pb)$
Exact NLO (NLO)	MRSR2[30]	NLO only	$4.87^{+0.30}_{-0.56}$
Laenen, Smith and van Neerven (LSvN)	MRSD′[30]	NLO + gluon resummation	$4.94^{+0.71}_{-0.45}$
Berger and Contopanagos (BC)	CTEQ3[32]	NLO + gluon resummation	$5.52^{+0.07}_{-0.42}$
Bonciani, Catani, Mangano, Nason and Trentadue (BCMNT)	MRSR2[30]	NLO + gluon resummation	$5.06^{+0.13}_{-0.36}$

Table 2.1: Calculations of $\sigma_{t\bar{t}}$ at $\sqrt{s} = 1.8$ TeV for $m_t = 175$ Gev/c^2.

the top quark (Γ_{top}) is ≈ 1.8 GeV and its lifetime is $\simeq \frac{\hbar}{\Gamma_{top}} \simeq 10^{-25}$ seconds. In comparison, the hadronization time scale is of the order of $\approx 10^{-24}$ seconds. Since the lifetime of the top quark is shorter than the hadronization time scale, the top quark decays before the hadronization can take place.

Assuming the Standard Model couplings, the top quark decays to a b quark via W emission ($t \to W^+ b$), where the W boson is real because $m_t > M_W^+ + m_b$. This is a weak flavor changing charge current (FCCC) decay. Other FCCC decays such as $t \to W^+ s$ and $t \to W^+ d$ are also allowed, but are suppressed by factors of $\approx 10^{-3}$ (for $t \to W^+ s$) and $\approx 10^{-4}$ (for $t \to W^+ s$) by the mixing elements of CKM matrix [15]. Super-symmetric models predict the existence of a pair of charge Higgs scalers ($H^\pm$) [34]. If $M_H^+ < m_t - m_b$ then the decay $t \to H^+ b$ can also occur. Recent searches and the limits on the charged Higgs decay mode of the top quark can be found in reference [35]. Other decay modes such as flavor changing neutral currents (FCNC) are also predicted but are many orders of magnitude smaller in size [33]. These have branching fractions of BR($t \to cg$) $\sim 10^{-10}$, BR($t \to c\gamma$) $\sim 10^{-12}$, BR($t \to cZ$) $\sim 10^{-13}$ and BR($t \to cH$) $\sim 10^{-14}$. Any observation of charged Higgs decay mode or FCNC decays of the top quark would be an evidence for the new physics beyond the Standard Model.

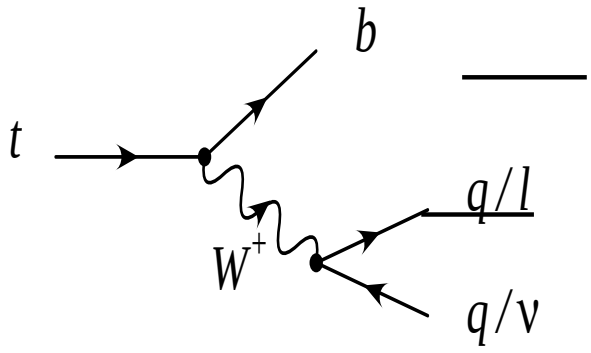

Figure 2.12: The Standard Model decay of the top quark.

It should be noted that it is not only the large mass of the top quark which gives it its short lifetime, but also the fact that the decay of t to b is not CKM suppressed.

2.6 Experimental Signature

This dissertation focuses on the Standard Model decay of the top quark ($t \to W^+b$) (Figure 2.12). The daughter b quark fragments and hadronizes to form a jet of final state particles and the W boson decays into fermions pairs $l\nu_l$ or $q\bar{q}$ (where l can be e or μ or τ and $q\bar{q}$ can be $u\bar{d}$ or $c\bar{s}$). In LO QCD, the branching ratios of W [93] into leptons and quarks are $\frac{1}{3}$, but quark decay modes get a factor of 3 enhancement because of color. For the purpose of experimental analysis, the top quark decay channels are classified using the decay modes of the W boson. In the case where $V_{tb} = 1$, the top quark will decay 100% of the time to b quark. Thus each $t\bar{t}$ event will have two b quarks and two W bosons. The decay channel classification is summarized in Table 2.2 and the relative branching fractions are shown in the Figure 2.13.

For data analysis, a $t\bar{t}$ event is classified into three broad categories which can be further subdivided by looking for semi-leptonic b quark decay involving soft e's and μ's. The latter technique is known as soft lepton b tagging.

1. The *alljets* Channel:

These are the events in which both the W's decay hadronically. The final state signature of an alljets event is six or more jets, where 2 jets come from the b decay and 4 jets come from the W decays. There may also be additional jets from the initial/final state radiation. Missing transverse energy ($\not\!\!E_T$) is not present at parton level but can arise from the mis-measurements of the energy in the event.

	$W \to e\nu_e$ (1/9)	$W \to \mu\nu_\mu$ (1/9)	$W \to \tau\nu_\tau$ (1/9)	$W \to q\bar{q}$ (2/3)
$W \to q\bar{q}$ (2/3)	12/81 $(e + jets)$	12/81 $(\mu + jets)$	12/81 $(\tau + jets)$	36/81 (all jets)
$W \to \tau\nu_\tau$ (1/9)	2/81 $(e\tau)$	2/81 $(\mu\tau)$	1/81 $(\tau\tau)$	
$W \to \mu\nu_\mu$ (1/9)	2/81 $(e\mu)$	1/81 $(\mu\mu)$		
$W \to e\nu_e$ (1/9)	1/81 (ee)			

Table 2.2: Decay modes and their branching fractions for a $t\bar{t}$ pair. Note that all the branching fractions are calculated assuming $V_{tb} \simeq 1$.

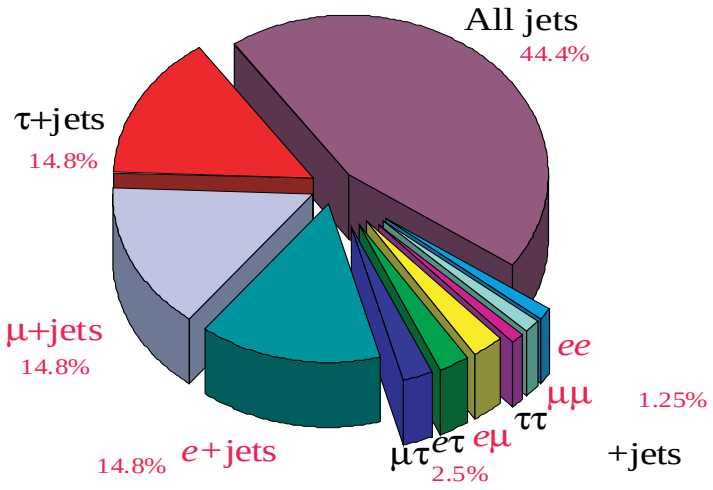

Figure 2.13: A pie chart showing the relative cross sections for various decay channels of a $t\bar{t}$ pair.

This is the channel with the largest branching ratio ($\simeq 44\%$) but it suffers from the difficulty of enormous background from QCD multijet events.

2. **The** *leptons + jets* **channel (l+ jets):**

These are the events in which one W boson decays into leptons ($e\nu_e$ or $\mu\nu_\mu$

or $\tau\nu_\tau$) and the other into quarks. The final state signature is one high p_T lepton (e or μ or τ), four or more jets (2 from b quark decay and 2 from W decay) and missing transverse energy ($\not\!\!E_T$) from the presence of the undetected neutrino in the event. As with the alljets case there may be additional jets from the initial/final state radiation. Each of the three l + jet channels has a branching fraction of about $\simeq 15$ % . There is some enhancement in the e + jets and μ + jets channels through τ + jets events in which the τ has subsequently decayed to e or μ. The main background comes from inclusive W boson production with associated jets. There is also contribution from QCD multijet events, mainly from $b\bar{b}$ production, in which one b decays to a lepton and the associated jet is not reconstructed correctly.

3. The *dilepton* Channel:

These are the events in which both the W's decay leptonically giving ee, $\mu\mu$, $\tau\tau$, $e\mu$, $e\tau$, $\mu\tau$ final states. The signature of a dilepton event is: two high p_T leptons, two (or more) jets and missing transverse energy from the neutrinos in the event. Events in which the leptons are of the same type (ee, $\mu\mu$ and $\tau\tau$) have a branching fraction of 1.25% and the events in the leptons are of distinct type ($e\mu$, $e\tau$ and $\mu\tau$) have a branching fraction of about $\simeq 2.5$ %. The τ channels are not directly observed but they contribute to the ee, $\mu\mu$ and $e\mu$ channels via the leptonic decays of the τ. Since each event contains at least two neutrinos, unlike the alljets and the lepton+jets events, events in the dilepton channels can not be fully reconstructed by the detector. Experimently, the dilepton channels are the cleanest of the top quark decay channels because of the small backgrounds.

2.7 The $e\mu$ Channel

Figure 2.14 shows the schematic diagram for the $t\bar{t} \rightarrow e\mu$ channel. This is the focus of this thesis. In the following section we summarize the characteristics of the signal events and then go on to discuss possible backgrounds from physical and instrumental effects.

2.7.1 Signal Characteristics

An $e\mu$ dilepton candidate consists of an event in which one of the W bosons has decayed to give $e\nu_e$ and other $\mu\nu_\mu$. Thus the experimental signature is:

- 1 large transverse energy electron (E_T^e) - from $W \rightarrow e\nu_e$ decay
- 1 large transverse momentum muon (P_T^μ) - from $W \rightarrow \mu\nu_\mu$ decay
- Missing transverse energy ($\not\!\!E_T$) - from the two neutrinos

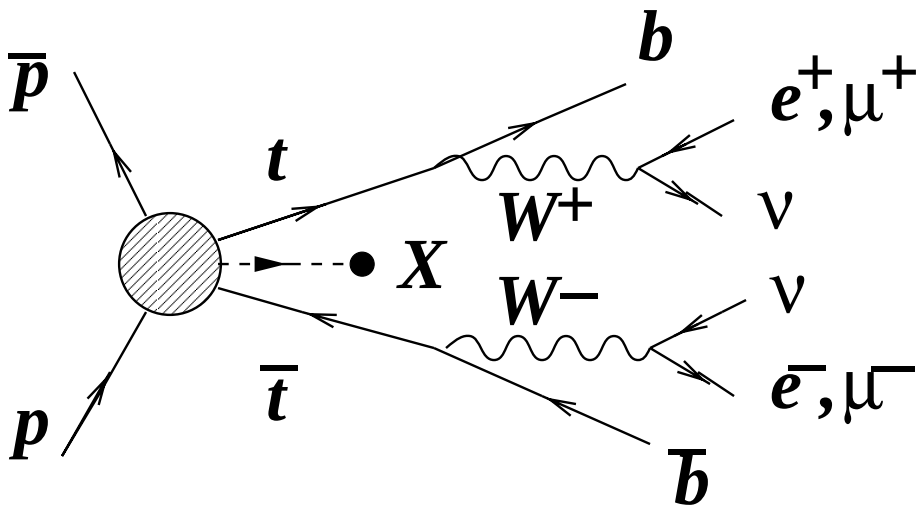

Figure 2.14: Schematic of the $t\bar{t} \rightarrow e\mu$X decay.

- ≥ 2 jets - from the fragmentation of the two b quarks (and initial/final state radiation)

The direct branching fraction for $t\bar{t} \rightarrow b\bar{b}WW \rightarrow e\nu_e\mu\nu_\mu$ + jet jet is 2.47 %. This is increased by an additional 0.96 % when the contributions from $t\bar{t} \rightarrow l\tau \rightarrow e\mu$ decays are included (where l can be e or μ or τ). However, the detection and reconstruction efficiencies for the τ events are somewhat smaller because the transverse energy (momentum) spectrum for the $e(\mu)$ from a τ decay is softer than those from the direct W decay and the presence of additional neutrinos leads to a decrease on the total missing transverse energy ($\not\!\!E_T^{cal}$).

2.7.2 Backgrounds

The background processes to the $e\mu$ channel can be divided into two main categories: physical and instrumental. These are discussed below.

Physical Backgrounds

These are the result of processes which lead to final state containing an electron and a muon with $\not\!\!E_T^{cal}$ and jets. These can mimic the signatures of top quark decay into $e\mu$ channel. The most significant of these are discussed below.

1. Z + jets production

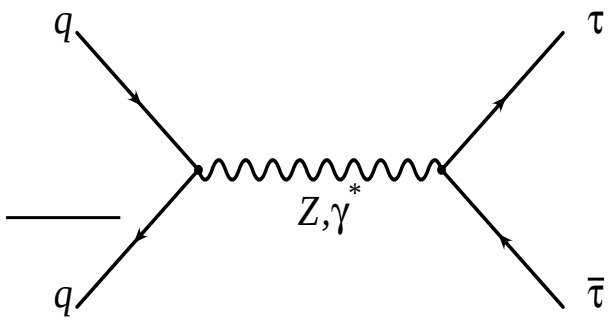

Figure 2.15: Lowest-order diagram for $\tau^+\tau^-$ production with Z or γ^* propagator.

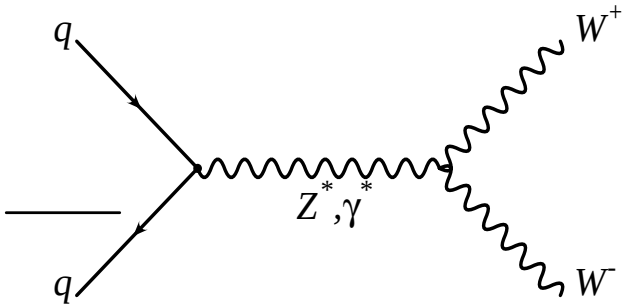

Figure 2.16: Lowest-order diagram for the Drell-Yan production of WW pairs.

The inclusive production of a Z boson with associated jets can be a source of background to $t\bar{t} \to e\mu$ events. Here the Z boson decays into $\tau^+\tau^-$ and taus further decay to give the e and μ. The Feynman diagram for the leading order production of $Z \to \tau\tau$ is shown in the Figure 2.15. The jets in these events are typically produced through radiative processes and have smaller transverse energies than those from the b jets in the top events. The production cross section of $Z \to \tau\tau \to e\mu$ is ≈ 12 pb (see appendix in [58]) which is significantly larger than the $t\bar{t} \to e\mu$ cross section. While the kinematics and topology can be use to suppress these events, they still provide significant background.

2. Drell-Yan $\tau^+\tau^-$ pair production

The Drell-Yan production of $\tau^+\tau^-$ pairs is also a source of a background. As with the $Z \to \tau^+\tau^-$ decay case, the $\tau\tau \to e\mu$ decay can mimic the signatures of a top quark event. The lowest-order Feynman diagram for this process is shown in Figure 2.15. The jets here are also produced through radiative processes and

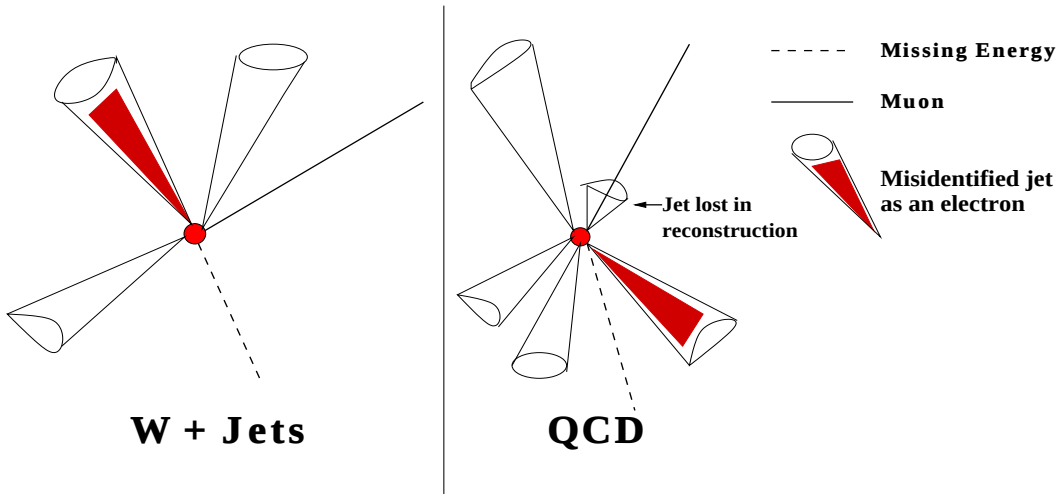

Figure 2.17: Cartoon of the instrumental fakes for W+jets and QCD events, where at least one jet in the event is misidentified as an electron.

have smaller transverse energies. Further suppression can be achieved by using the transverse energy spectra of the e (μ), which is even softer than that from $Z \to \tau\tau \to e\mu$. The cross section for this process is ≈ 6 pb [75].

3. WW pair production

The WW pairs are produced at the Tevatron through Drell-Yan process (See Figure 2.16). The final $e\mu$ state comes directly from the decays of the two W bosons. There is also a small contribution from the $W \to \tau\nu_\tau$ decay with a sequential $\tau \to e(\mu)\nu\bar{\nu}$ decay. The production cross section for $p\bar{p} \to W^+W^-$ at the Tevatron is ≈ 10 pb [36]. The branching fractions of $WW \to e\mu$ (including τ decays) is 3.43% so that the production cross section for the $e\mu$ final state is about 0.34 pb. Also, like other Drell-Yan processes, the jets in these events are produced by radiative processes and the E_T spectra are softer. However in terms of lepton final state, the transverse energy spectra of leptons are identical to those of $t\bar{t}$ events.

Instrumental Backgrounds

There are some backgrounds which are the results of instrumental effects in the detector and arise from the misidentification of jets as electrons. These can be conveniently separated into two categories depending on the source of the muon in the events.

1. W+jets production

The production of W + jets events is one of main sources of instrumental background. The measured production cross section for $p\bar{p} \to W\mathrm{X} \to \mu\nu\mathrm{X}$ is ≈ 2.42

nb [37]. If one of the associated jets is misidentified as an electron (Figure 2.17), then the final state can mimic the $t\bar{t} \rightarrow e\mu$X signature.

2. $b\bar{b}$ and $c\bar{c}$ production (QCD multi-jet processes)

This background is related to the production of QCD jets (mainly $b\bar{b}$ and $c\bar{c}$). The heavy quark (b or c) can have a semi-leptonic decay to a muon and may transfer all (most) of its energy to the muon, leaving little energy to hadronize. Such jets can easily be missed in reconstruction. If one of the other jets in the event is misidentified as an electron, then the final state would be one electron (misidentified jet), one muon (from b or c decay) and sufficient missing transverse energy (from mis-measurement). This is shown schematically in Figure 2.17. Despite heavy suppression from kinematical and topological constraints, this background can still be a source of significant problem because of the large $b\bar{b}$ and $c\bar{c}$ cross sections [38].

Chapter 3

Experimental Apparatus

Science clears the fields on which technology can build.

- Werner Heisenberg

This chapter gives a brief description of the experimental apparatus used in this study. In order to detect the particles produced in the collisions of protons and anti-protons, it is necessary to build a detector system around the collision point. One such detector, DØ, is located at one of the two collision points on the Tevatron ring located at Fermilab, Illinois.

3.1 The Tevatron, a particle accelerator

To reach the collision point inside the DØ detector the particle beams go through seven different parts of the Fermilab accelerator complex. These are: a Cockroft-Walton accelerator (pre-accelerator), the Linac (linear accelerator), the Booster synchrotron, the Main Ring, the Anti-proton Source, the Anti-proton Debuncher and the Tevatron Ring. Figure 3.1 shows the location of each part of the complex.

The source of the protons is hydrogen gas. This interacts with a hot cesium cathode to produce H^- ions. The ions are electro-statically accelerated by the Cockroft-Walton preaccelerator to an energy of 750 KeV and injected into the linac. Here, high radio frequency cavities accelerate the ions to an energy of 200 MeV. The H^- ions are then passed through a carbon foil which strips two electrons from the ion to create a beam of protons (H^+).

The next stage in the acceleration process is done by a 151 m diameter synchrotron, called the Booster. Synchrotron typically consists of three major parts: RF (radio-frequency) cavities, bending magnets, and focusing/defocusing magnets. The alternating high voltages of the RF cavities accelerate the beams of charged

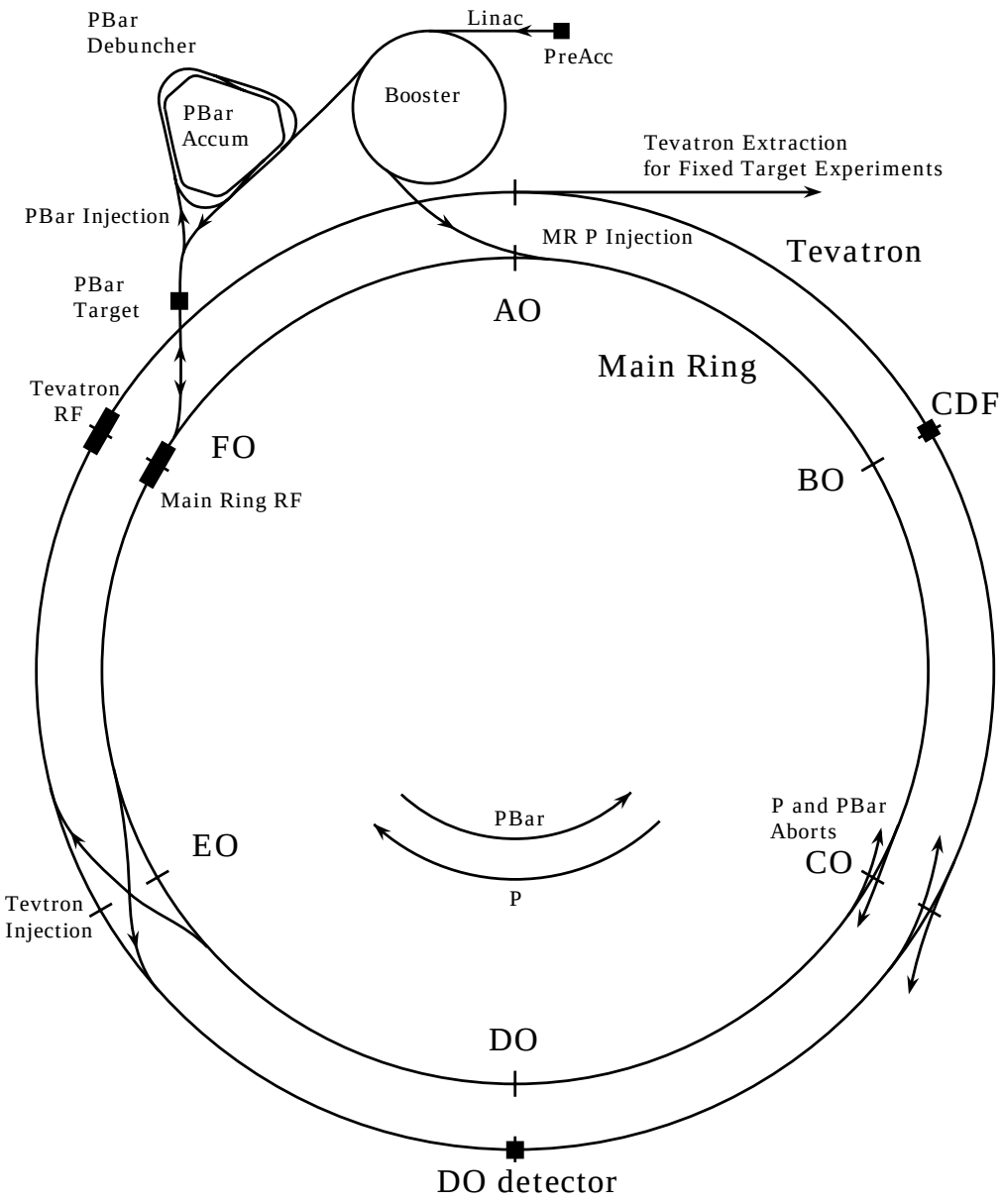

Figure 3.1: Schematic of the Fermilab accelerator complex.

particles every time they pass through the cavities and synchronize them with the RF frequency. Dipole magnets are used to bend the orbit of the beam by the Lorentz force exerted on charged particles moving in the magnetic field. Alternate quadrapole magnets are used to keep the beam focused in both transverse and longitudinal directions to ensure its stability and maintain high particle density. Protons

travel roughly 20,000 orbits inside the Booster as their energy is incremented up to 8 GeV. The booster repeats its cycle 12 times in rapid succession, delivering twelve pulses or bunches of protons for injection into the Main Ring.

The main ring is a proton synchrotron with a circumference of ≈ 6 km. It consists of a string of 774 conventional magnetic dipoles, 240 quadruples and 18 RF cavities. Once the protons have been injected into the main ring, they are accelerated to 150 GeV and then injected into the Tevatron Ring. The second task of the Main Ring is to generate 120 GeV protons, which can be extracted and used to generate anti-protons. The Main Ring beam pipe passes through the upper part of the DØ detector and proton losses can give rise to spurious signals in the detector. For this reason, events are not recorded during the time when main ring is active.

For anti-proton production, a 120 GeV proton beam extracted from the Main Ring is directed onto a nickel (or copper) target. The collisions produce a large quantity of secondary particles including anti-protons. These are selected from the other collision products by a series of magnets and transfered to the Debuncher ring. Here they are cooled and subsequently transferred to the Accumulator ring for beam storage and further cooling.

Accelerator radius	1000 m
Maximum beam energy	900 GeV
Injection energy	150 GeV
Peak luminosity	$\approx 2 \times 10^{31}$ cm^{-2} s^{-1}
Number of bunches	6 p, 6 $\bar{p}$
Intensity per bunch	$\approx 10^{11} p$, $\approx 5 \times 10^{10} p\bar{p}$
Crossing angle	0^0
Bunch length	50 cm
Transverse beam radius	≈ 25 μm
Fractional energy spread	0.15×10^{-3}
RF frequency	53 MHz
$\bar{p}$ stacking rate	$\approx 3.5 \times 10^{10}$ per hour
Beam crossing frequency	290 kHz
Period between crossings	3.5 μs

Table 3.1: Parameters of the Fermilab Tevatron collider for Run 1 (1992-1996).

The Debuncher was designed to increase the density of anti-protons using two cooling techniques. The first of these, debunching uses a computer-coded RF

voltage to speed up slower anti-protons and slow down the faster ones. The second technique, known as stochastic cooling, reduces the transverse movement of the anti-protons. Here, the particles deviated from the central orbit are detected by sensors, and signals are passed to kicker electrodes which correct the particles trajectories.

The anti-protons from the debuncher are sent to a concentric ring called the Accumulator for further cooling and beam accumulation. It takes several hours to store the hundreds of billions of anti-protons needed for injection into the Main Ring.

The Tevatron Ring is a synchrotron made from the super-conducting magnets and is located 25 cm below the Main Ring in the same accelerator tunnel. It consists of 1000 super-conducting magnets operating at liquid helium temperature ($\simeq 4.6K$) which allows acceleration of the protons/anti-protons up to 900 GeV. 150 GeV bunches of the protons are transferred from the Main Ring to the Tevatron. The anti-protons are transferred from the Accumulator to the Main Ring, accelerated upto 150 GeV and then transferred to the Tevatron on an orbit in the opposite direction to the protons. During Run I, the Tevatron was operated with six proton and six anti-proton bunches spaced by about 3.5 μs. Both beams are accelerated to 900 GeV giving a center-of-mass energy of 1.8 TeV for $p\bar{p}$ collisions. The luminosity is increased by focusing the beams with super-conducting quadrapole magnets which are located near the interaction region. The beam spot has $\sigma_{x,y} \approx 40\mu$m and $\sigma_z \approx$ 30 cm.

A summary of the Tevatron operation parameters for Run I are listed in the Table 3.1. For a more detailed discussion of the accelerator the reader is referred to references [39, 40].

3.2 The DØ Detector

The DØ detector is a multipurpose facility designed to study high mass states and large P_T phenomena in the $p\bar{p}$ collisions [40]. Some of the physics goals were: the search for the top quark, precision studies of the W and Z bosons to test of the electroweak part of the Standard Model, studies of perturbative QCD, the production of b-quarks and the search for evidence of new phenomena beyond the Standard Model. The main features of the detector are good electron and muon identification capabilities, and finely segmented calorimetry which results in good measurements of electrons, photons, jets and missing transverse energy ($\not\!\!E_T$).

The detector consists of three main subsystems: the central tracking system, the calorimeters, and the muon spectrometers. A cut-away isometric view is shown in the Figure 3.2. Before proceeding to a discussion of the detector, it is useful to review the coordinate system and angle conventions used in the DØ experiment.

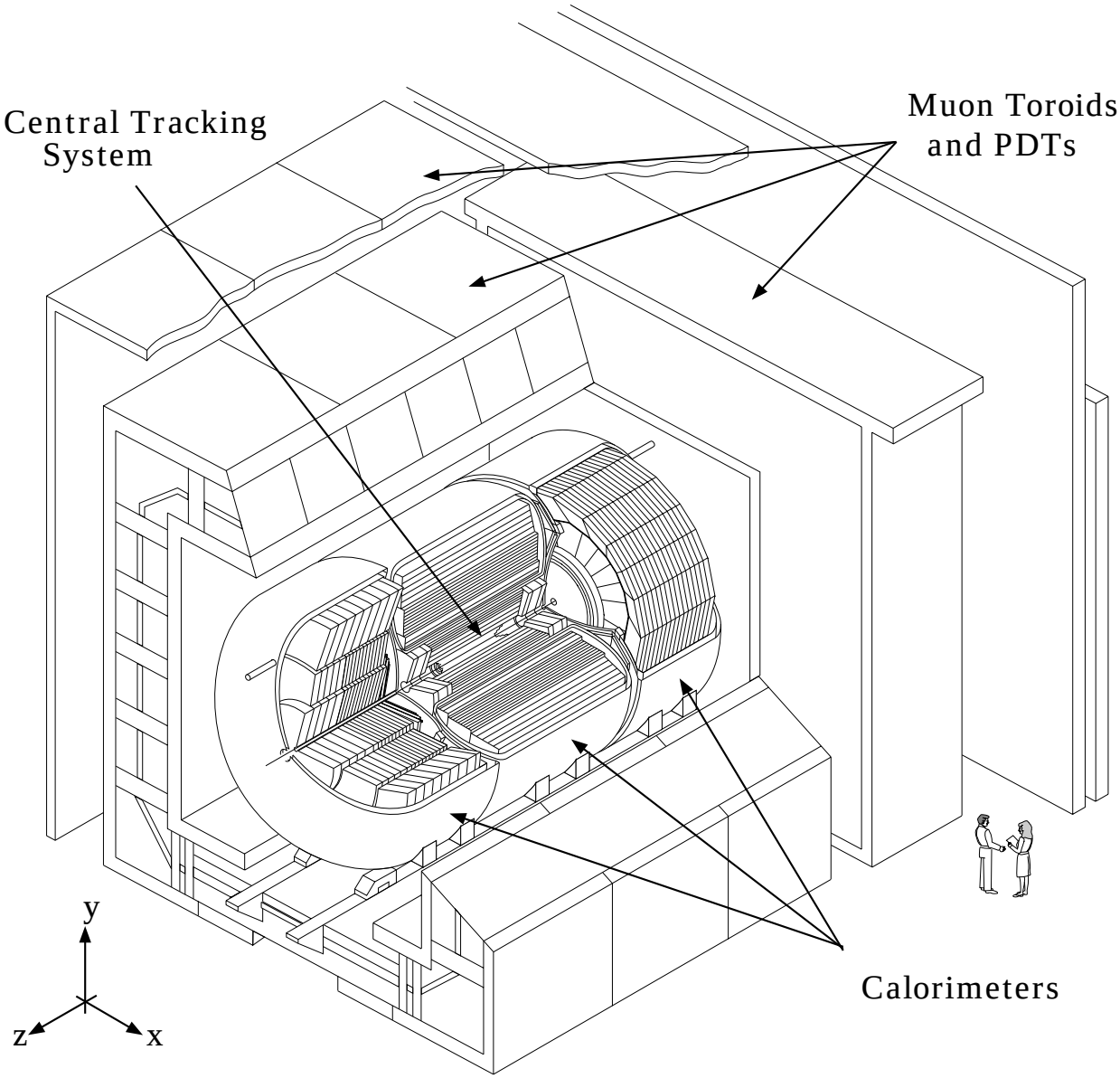

Figure 3.2: A cut-away isometric view of the DØ detector.

3.2.1 The DØ Coordinate System

DØ uses a right-handed coordinate system, where the z axis coincides with the beam-line and the positive x direction is defined as the direction of the proton beam. The x and y axes are then defined as the horizontal and vertical directions respectively (see Figure 3.3). The azimuthal angle (ϕ) is measured with respect to the $+x$ direction, and the polar angle (θ) is measured with respect to the $+z$ direction. The polar angle (θ) can be mapped to a more convenient coordinate

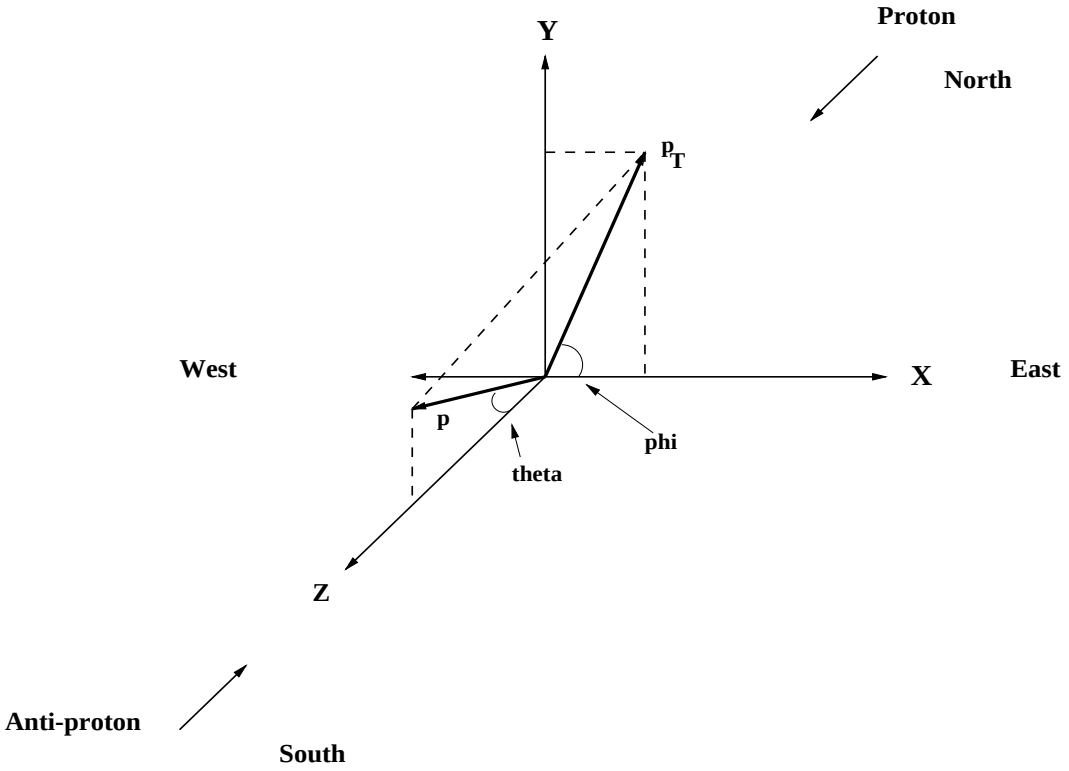

Figure 3.3: The DØ coordinate system.

called pseudorapidity (η) which is defined as

$$\eta = -\ln\left[\tan\left(\frac{\theta}{2}\right)\right] \tag{3.1}$$

In the high energy limit $m/E \to 0$ and η approaches the true rapidity (y) of the particle:

$$y = \frac{1}{2}\ln\left(\frac{E+p_z}{E-p_z}\right) \approx \eta \tag{3.2}$$

Rapidity is a useful quantity because it is invariant under longitudinal Lorentz boosts. Also, in many processes the differential cross sections are constant in rapidity. For example, in minimum bias events the quantity $\mathrm{dN}/\mathrm{d}\eta \approx$ constant.

It is often convenient to express polar angles in the detector rest frame denoted η_{det} which is computed with respect to $x = y = z = 0$. In practice, the interaction point is characterized by a Gaussian distribution centered at $z \approx 0$ with $\sigma_z \approx 30$ cm, so that η and η_{det} may differ slightly for a given particle.

3.2.2 The Central Detector

The purpose of the central detector is to measure the trajectories of the charged particles coming out from the interaction point and determine the position of the interaction vertex (collision point). The central detector system of the DØ detector has no magnetic field so momentum information is not available at this stage. Figure 3.4 shows a schematic of the system indicating the positions of the various sub-systems. These are the vertex drift chamber (VTX), the transition radiation detector (TRD), the central drift chamber (CDC) and the two forward drift chambers (FDC).

A drift chamber consists of an enclosed volume filled with gas and arrays of anode and cathode wires. These create regions of approximately uniform electric field in the gas which acts as the ionization medium. When a charged particle passes through the chamber, the electrons produced in the ionization are drawn to the anode wires and create a signal pulse on the wire. By measuring the time taken to collect the charge (drift time) and the spatial position of the hit wire, the particle position can be determined.

The concept of the TRD is derived using the principles of electrodynamics [41]. A relativistic charged particle emits light when it passes through a junction between two dielectric media. The TRD utilizes this information to distinguish between charged pions and electrons.

The length of the central detector is 270 cm and its radius is 78 cm. It provides charged particle tracking in the region $|\eta| < 3.2$ with good spatial resolution of individual particles and a good determination of the ionization (dE/dx)

Vertex Chamber (VTX)

The vertex chamber is the innermost part of the tracking detector. It is a jet topology drift chamber whose inner and outer radii are 3.7cm and 16.2 cm respectively [40]. It consists of three layers of concentric cells with 110 cm wires oriented parallel to the beam axis. The innermost layer has 16 cells in azimuth and the outer two layers have 32 cells each. Figure 3.5 shows the cell geometry in the plane transverse to the beam direction (r, ϕ). The sense wires are staggered by $\pm 100 \mu$m to resolve left-right ambiguities. The principle design and operating parameters of the vertex chamber are listed in the Table 3.2.

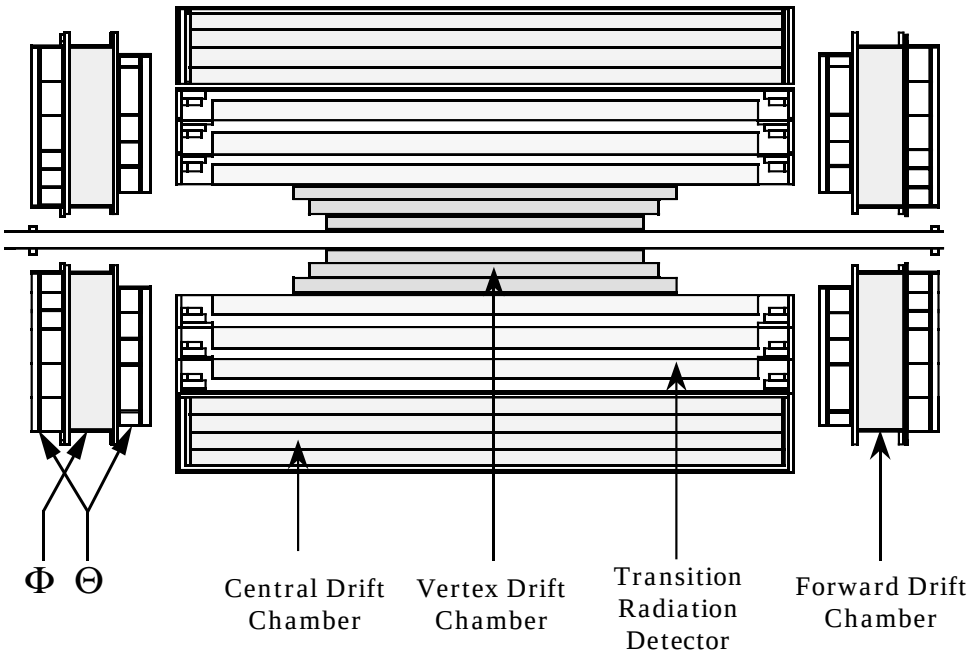

Figure 3.4: A side view of the DØ central tracking system.

Transition Radiation Detector (TRD)

The TRD is located in the space between the VTX and the CDC. It is used to provide electron identification independent of the calorimeter. When highly relativistic charged particles ($\gamma > 10^3$) traverse boundaries between media with different dielectric constants, transition radiation X-rays are produced on a cone with an opening angle of $1/\gamma$. Thus, the energy flux of the radiation is proportional to the γ of the particle. The DØ TRD consists of three separate modules, each of which contains a radiator and an X-ray detection chamber. The X-ray energy spectrum is determined by the thickness of the radiator layers and the gaps between the radiator layers.

Each of the modules contains 393 dielectric (polypropylene) foils with a mean gap of 150μm located in a gaseous nitrogen volume. Proportional drift wire chambers are used to convert the X-rays and the resulting charge is radially drifted to sensor wires for readout. Both magnitude and the arrival time of charge are used to distinguish electrons from hadrons.

Central Drift Chamber (CDC)

The central drift chamber sits between the TRD and the central calorimeter and is used to detect tracks at large angles. The CDC is a cylindrical shell of length 184 cm with a radial coverage from 49.5 cm to 74.5 cm and provides coverage for

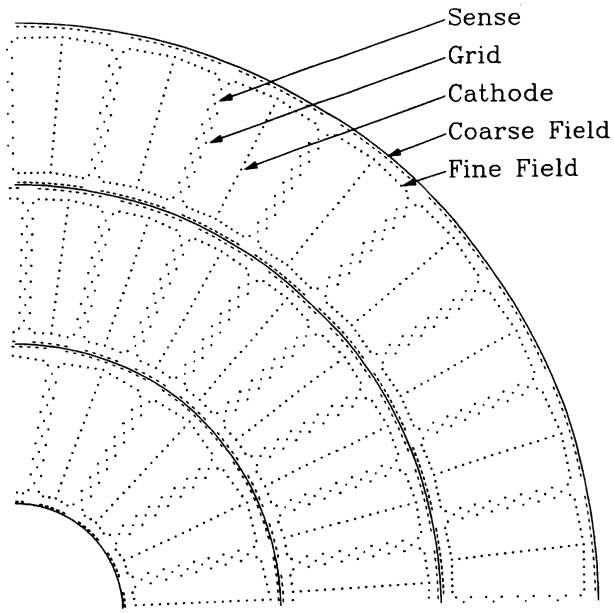

Figure 3.5: A rϕ view of one quadrant of the VTX detector

Length of the active volume:	Layer 1	96.6 cm
	Layer 2	106.6 cm
	Layer 3	116.8 cm
Radial interval (active)		3.7 - 16.2 cm
Number of layers		3
Radial wire interval		4.57 mm
Number of sensor wires/cell		8
Number of sensor wires		640
Gas composition		CO_2(95%)-ethane(5%)-H_2O(0.5%)
Gas pressure		1 atm
Drift field		1.0-1.6 kV/cm
Average drift velocity		7.6-12.8 μm/ns
Gas gain at sense wires		4x10^4
Sense wire potential		+2.5 kV
Sense wire diameter		25 μm NiCoTin
Guard wire diameter		152 μm Au-plated Al

Table 3.2: The operating parameters of the VTX chamber.

$|\eta| < 1.2$. A schematic of the CDC is shown in the Figure 3.6. It consists of four concentric rings with 32 azimuthal cells per ring. Each cell contains 7 equally spaced tungsten sensor wires of a diameter 30 μm. The wires are parallel to the z-axis and read out at one end to measure the ϕ coordinate. Delay lines embedded in the inner and outer shelves of each cell are used to propagate the signals induced from the nearest neighboring anode wire. The z coordinate of a track is measured from the difference in the signal arrival times at the two ends. The resulting r-ϕ resolution is $\approx 180\,\mu$m and the z resolution is ≈ 3 mm. Table 3.3 gives a summary of some of the parameters of the CDC.

Forward Drift Chambers (FDC)

The forward drift chambers [40] are used to increase the coverage for charged particles up to $|\eta| < 3.1$. There are two FDC modules located at the either end of the central detector and just before the end-cap calorimeters. Each FDC consists of a Φ chamber sandwiched between two Θ chambers, as shown in Figure 3.7. The Φ modules has radial sense wires and measures the ϕ coordinate and Θ chambers measures the θ coordinate. The geometric composition of the FDC cells is different from that of the CDC, but the operating principle is similar. The FDC position resolution is about 200 μm in r-ϕ and 300 μm in r-θ. Table 3.4 lists the main operating parameters of a FDC.

3.2.3 The DØ Calorimeters

Because of the absence of a central magnetic field the energy measurements at the DØ experiment rely heavily on the calorimeter. This also plays an important role in the identification of electrons/photons/jets and muons as well as the determination of the transverse energy balance in the event.

In a calorimeter, there are two types of particle showers, electro-magnetic and hadronic. An electro-magnetic shower consist of a cascade of electrons, positrons, and photons produced by bremsstrahlung and e^+e^- pair production. High energy e^- or e^+ radiate photons as they travel through material, and the photons in turn create lower energy e^+e^- pairs. The number of particles increases exponentially until electrons reach the critical energy, at which point they lose the same amount of energy by radiation and ionization. After that, the number of particles decreases and their energies gradually dissipate through the process of ionization. Such a electro-magnetic shower has a short and narrow energy profile. The longitudinal development of the showers is characterized by the radiation length (X_0) of the calorimeter material, which is the the mean distance over which an electron loses all but $1/e$ of its energy by bremsstrahlung.

Hadronic showers are caused by the strong (nuclear) interactions between the hadrons and the nuclei of the calorimeter material. In such an interaction most of the energy is transferred to the nucleus resulting in the production of secondary

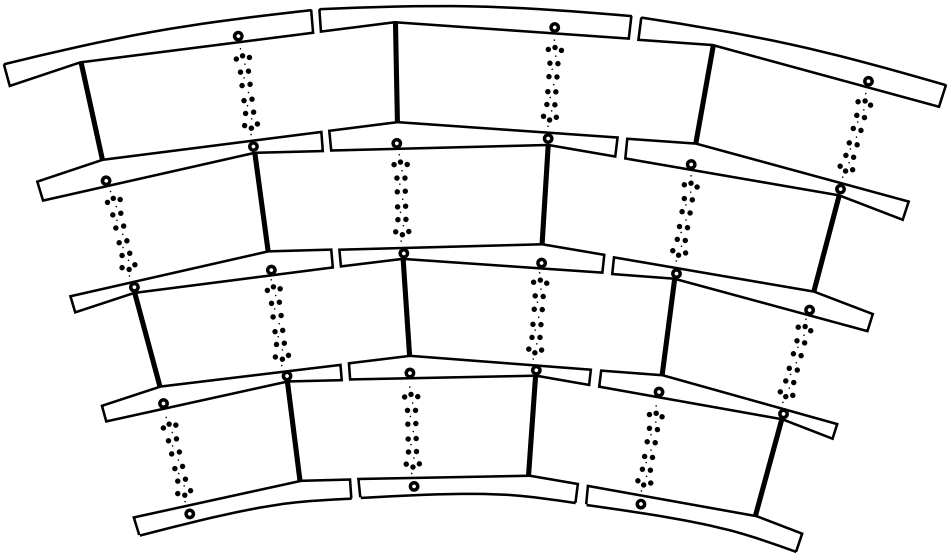

Figure 3.6: A end view of the 3 CDC modules.

Active volume length	179.4 cm
Active radial interval	51.8 - 71.9 cm
Number of layers	4
Radial interval between wires	6.0 mm
Number of sensor wires/cell	7
Number of sensor wires	896
Number of delay lines	256
Gas composition	Ar(93%)-CH_4(4%)-CO_2(3%)-H_2O
Gas pressure	1 atm
Drift field	620 V/cm
Average drift velocity	34 μm/ns
Gas gain in the sensor wires	$2,6 \times 10^4$
Sensor wire potential	+1.5 kV
Sensor wire diameter	30 μm Au-plated W
Guard wire diameter	125 μm Au-plated CuBe

Table 3.3: Some parameters of the CDC chamber.

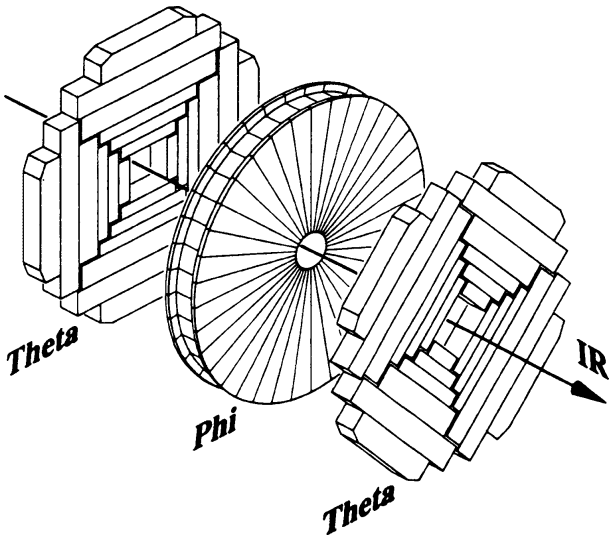

Figure 3.7: An exploded end view of the FDC.

	Θ *modules*	Φ *modules*
z interval	104.8-111.2 cm	113.0-127.0
	128.8-135.2 cm	
Radial interval	11-62 cm	11-61.3 cm
Number of cells per radius	6	
Maximum drift distance	5.3 cm	5.3 cm
Stagger of sense wires	0.2 mm	0.2 mm
Sensor wire separation	8 mm	8 mm
Angular interval/cell		10°
Number of sensor wires per cell	8	16
Number of delay lines per cell	1	0
Number of sense wires/end	384	576
Number of delay lines read out/end	96	
Gas mixture	Ar(93%)-CH_4(4%)-CO_2(3%)-H_2O	
Gas pressure	1 atm	1 atm
Drift field	1.0 kV/cm	1.0 kV/cm
Average drift velocity	37 μm/ns	40 μm/ns
Gas gain at sense wire	$2.3, 5.3 \times 10^4$	3.6×10^4
Sense wire potential	+1.5 kV	+1.5 kV
Sense wire diameter	30 μmAu-plated W	
Guard wire diameter	163 μm Au-plated Al(5056)	

Table 3.4: Forward drift chamber parameters.

hadrons, which in turn produce more hadrons. This cascade process begins to stop when the energies of the secondary hadrons are small enough to be exhausted by ionization or to be absorbed in a nuclear process. Hadronic showers tend to be wide and more penetrating than the electro-magnetic showers. The length scale appropriate for hadronic showers is the nuclear interaction length (λ_I) which is given very roughly by $\lambda_I \approx 35\ \mathrm{A}^{1/3}\ \mathrm{g\ cm}^{-2}$, where A is the atomic number o the material.

The DØ calorimeters [40] are of uranium-liquid argon sampling design. These consist of stacks of dense metallic plates which are used as energy absorber and the inter-plate gaps which is filled with some material to sample the ionization produced by electro-magnetic and hadronic showers. The DØ design uses liquid argon as the sensitive (sampling) material, and uranium (copper) as the absorber. Some of the advantages of this design are the unit gain of the liquid argon, the simplicity of calibration, the flexibility to segment the calorimeter in longitudinally and transversely, the radiation hardness and the relatively low unit cost for readout electronics.

The calorimeters (see Figure 3.8) are divided into three modules: the Central Calorimeter (CC), the North End Calorimeter (ECN), and the South End Calorimeter (ECS). Each module has an electro-magnetic section (EM) with 3mm uranium plates, a fine hadronic section with 6mm uranium plates and a coarse hadronic section with 4.7cm copper or stainless steel plates. To provide uniform coverage across the gaps between the cryostats, a scintillator counter known as the inter-cryostat detector (ICD) is used. This consists of an array of scintillator tiles and is located between the CC and EC cryostats. The EM section of the calorimeter is ≈ 21 radiation lengths deep, and is divided into four longitudinal layers for the study of shower depth profiles. The hadronic sections are 7 to 9 nuclear interaction lengths thick and are divided into four (CC) or five (EC) layers. The calorimeter transverse segmentation is 0.1×0.1 in $\Delta\eta \times \Delta\phi$ (see Figure 3.9) except for the third EM layer, where the maximum of electro-magnetic showers is expected, where the segmentation is 0.05×0.05. Figure 3.10 shows a typical unit cell of the calorimeter modules showing the liquid argon gaps, absorber plates, and signal boards.

Central calorimeter (CC)

The CC consists of three concentric cylindrical shells 226 cm in length with a radial coverage of $75 < r < 222$ cm and covers the pseudorapidity range $|\eta| \leq 1$. There are 32 EM modules in the inner ring, 16 fine hadronic (FH) modules in the surrounding ring and 16 coarse hadronic (CH) in the outer ring. In order to reduce the energy loss in cracks, the EM, FH, and CH module boundaries are arranged so that there are no cracks pointing at the interaction point. Table 3.5 summarizes the design specifications for the central calorimeter.

End Calorimeter (ECN, ECS)

There are two end calorimeters located at the north (ECN) and south (ECS) ends of the central tracking system (see Figure 3.8). Each calorimeter consists of one EM module (See Figure 3.11), one inner hadronic module (IH), and 16 middle

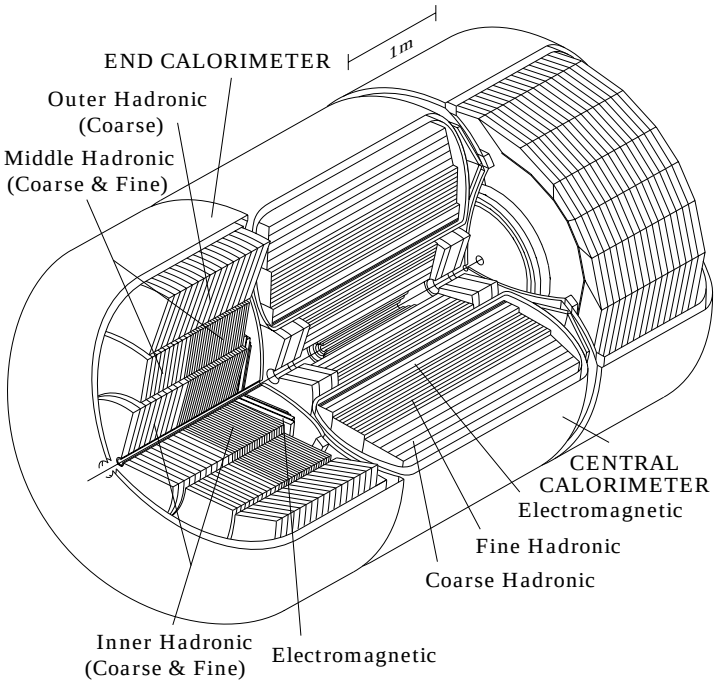

Figure 3.8: A cut-away view of the CC and EC calorimeters.

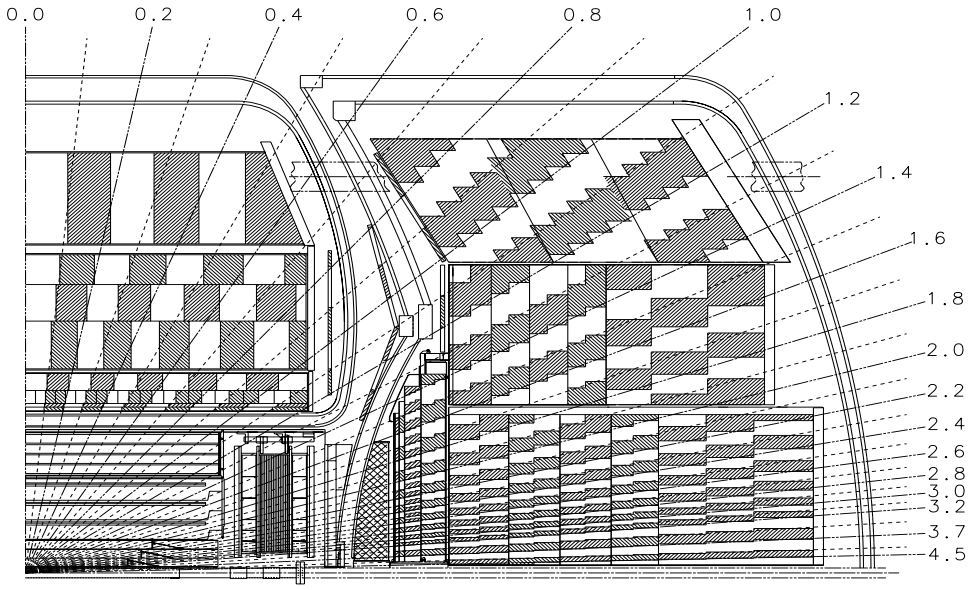

Figure 3.9: A schematic of one quadrant of the Calorimeters showing arrangement of cells and towers.

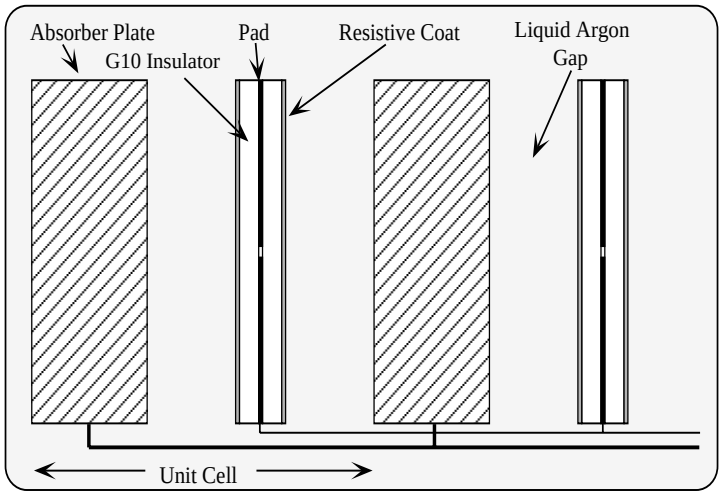

Figure 3.10: A calorimeter unit cell showing the arrangement of the absorber plate, argon gaps and readout boards.

	EM	FH	CH
Rapidity coverage	$\pm$ 1.2	$\pm$ 1.0	$\pm$ 0.6
Number of modules	32	16	16
Absorber material	Depleted Uranium	Depleted Uranium (1.7% niobium alloy)	Copper
Absorber material thickness (cm)	0.3	0.6	4.65
Argón gap (cm)	0.23	0.23	0.23
Number of cells/module	21	50	9
Longitudinal depth	20.5 X_0	3.24 λ_0	2.93 λ_0
Number of readout layers	4	3	1
Cells/readout layer	2, 2, 7, 10	21, 16, 13	9
Total radiation length	20.5	96.0	32.9
Radiation length/cell	0.975	1.92	3.29
Total absorption length	0.76	3.2	3.2
Absorption lengths/cell	0.036	0.0645	0.317
Sampling fraction (%)	11.79	6.79	1.45
Segmentation ($\eta \times \phi$)	0.1 $\times$ 0.1 (3rd EM: 0.05 $\times$ 0.05)	0.1 $\times$ 0.1	0.1 $\times$ 0.1
Total number of readout cells	10,368	3,456	768

Table 3.5: CC design parameters.

and outer hadronic (MH and OH) modules. The ECEM transverse segmentation is identical to the CCEM, except that the third layer segmentation is 0.1×0.1 for $|\eta_{\rm det}| > 2.5$. The azimuthal boundaries of the MH and OH modules are offset to prevent projecting cracks. Some of the specifications of the end calorimeters are listed in the Table 3.6.

Inter-cryostat Detectors (ICD) and Massless Gaps (MG)

There is a substantial amount of material in the form of cryostat walls which lies in the region $0.8 \leq |\eta| \leq 1.4$. Two scintillation counter arrays, known as inter-cryostat detectors (ICD) are placed in this region to correct for the energy deposited by the particles in the uninstrumented cryostat walls. Each ICD consists of 384 scintillator tiles of size 0.1×0.1, exactly matching the segmentation of the calorimeter cells. In addition, separate readout cells called massless gaps (MG) are installed inside the CC and EC cryostats in the $0.8 \leq |\eta| \leq 1.4$ region. These consist of three liquid argon gaps and two readout boards with no absorber plates. The MG detectors together with the ICD provide an approximation to the sampling of EM and hadronic showers and provide close to uniform energy resolution in the CC-EC transition gaps.

Calorimeter Readout and Performance

There are $\sim$ 47000 readout channels in the DØ calorimeter. The signals from the modules are brought to charge sensitive pre-amplifiers which are mounted in enclosures on the surface of each cryostat by specially fabricated cables. The output signals from the pre-amplifiers are then transported to the baseline subtractor (BLS), shaping and sampling circuits. Depending on the signal size, the BLS outputs can be amplified by a factor of between 1 and 8 so as to reduce the dynamic range requirements of subsequent digitization. The BLS outputs are sent from the detector platform to the moving counting house (MCH).

The performance of the calorimeter has been studied by using electron and pion beams with energies between 10 and 150 GeV at a test beam facility [40, 42] . The energy resolutions are:

$$\frac{\sigma(E)}{E} = \frac{16\%}{\sqrt{E(GeV)}} \oplus 0.3\% \tag{3.3}$$

and

$$\frac{\sigma(E)}{E} = \frac{41\%}{\sqrt{E(GeV)}} \oplus 3.2\% \tag{3.4}$$

for electrons and pions, respectively. The position resolution of the calorimeter is important for identification of the electron backgrounds due to overlap of photons and charged particle tracks. This varies approximately as $\sqrt{E}$ and also varies between 0.8 and 1.2 mm over the full range of impact positions.

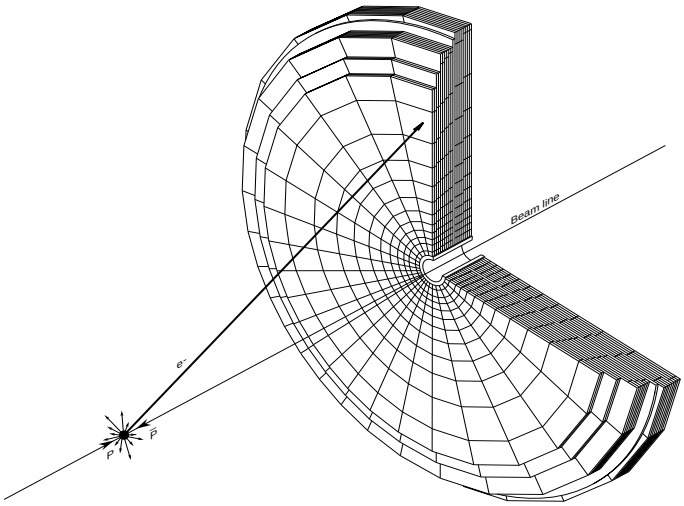

Figure 3.11: A view of the EC EM module.

	EM	IFH	ICH	MFH	MCH	OH
Rapidity coverage	1.3-4.1	1.6-4.5	2.0-4.5	1.0-1.7	1.3-2.0	0.7-1.4
Number of modules	1	1	1	16	16	16
Absorbing material[a]	U	U	SS[b]	U	SS	SS
Absorbent thickness (cm)	0.4	0.6	4.6	0.6	4.6	4.6
Argon gap (cm)	0.23	0.21	0.21	0.22	0.22	0.22
Number off cells/Module	18	64	12	60	12	24
Longitudinal depth	$20.5X_\circ$	$4.4\lambda_\circ$	$4.1\lambda_\circ$	$3.6\lambda_\circ$	$4.4\lambda_\circ$	$4.4\lambda_\circ$
Number of readout cells	4	4	1	4	1	3
Cells/readout layer	$2, 2, 6, 8$	16	12	15	12	8
Total radiation lengths	20.5	121.8	32.8	115.5	37.9	65.1
Total absorption lengths (Λ)	0.95	4.9	3.6	4.0	4.1	7.0
Sampling fraction (%)	11.9	5.7	1.5	6.7	1.6	1.6
Segmentation $\Delta\phi^c$	0.1	0.1	0.1	0.1	0.1	0.1
Segmentation $\Delta\eta^d$	0.1	0.1	0.1	0.1	0.1	0.1
Total readout channels	14976	8576	1856	2944	768	1784

Table 3.6: The design parameters of the ECN and ECS calorimeters.

[a] Depleted uranium. The absorbing material in modules FH (IFH and MFH) contains a 1.7% niobium alloy.

[b] Stainless steel

[c] The third layer of EM $\Delta\phi \times \Delta\eta = 0.05 \times 0.05$ for $|\eta| < 2.6$

[d] For $|\eta| > 3.2, \Delta\phi = 0.2$ $\Delta\eta \approx 0.2$

3.2.4 The Muon Spectrometers

Since muons are weakly interacting long lived particles they penetrate the detector material depositing little of their energy in the calorimeter as they pass through. The outermost part of the DØ detector consists of the wide angle (WAMUS) and small angle (SAMUS) muon spectrometers [43]. These consist of five toroidal magnets surrounded by proportional drift chambers (see Figure 3.13). The toroids provide magnetic fields ($\approx$ 2T) to bend the muon trajectory which is measured by the drift chambers. This system enables muon identification and measurement of trajectories down to approximately 3 degrees from the beam pipe. The total number of interaction length transversed by a muon varies with η (see Figure 3.12) but is typically $\geq 14X_o$.

Wide Angle Muon Spectrometers (WAMUS)

Each WAMUS consists of a toroidal magnet and three layers of proportional drift tube (PDT) planes (see Figure 3.13). The first layer (A) of PDT chambers is mounted in the inner surface of the magnetized toroids. The second and third layer (B and C) are mounted outside of the toroids and are separated by $\approx$ 1.4 m. The A layer consists of four planes of PDT's where as the B and C layers each have three planes. In the WAMUS spectrometers, the central toroid (CF) covers the pseudorapidity region $|\eta| \leq 1$ and two end toroids (EFs) cover $1 < |\eta| \leq 2.5$. Some other parameters of the WAMUS are summarized in the Table 3.7.

Small Angle Muon Spectrometers (SAMUS)

The small angle muon systems (SAMUS) consist of two toroids and sets of PDT's. The chambers cover the pseudorapidity region $2.5 \leq |\eta| \leq 3.5$ and are arranged into three stations A, B and C in the same manner as in the WAMUS spectrometers. Each layer consists of three doublets of proportional drift tubes oriented in x, y, and u (u being at 45^o with respect to x and y) directions. Further details about the SAMUS are listed in Table 3.7.

3.2.5 Trigger and Data Acquisition

During data taking in Run 1 (1992-1996), the bunch crossing rate of the Tevatron was 290 kHz. At this frequency there are hundreds of thousands of collisions occurring per second within the DØ detector. It is impractical to read out the entire detector for all the collisions even if all the events were of the interest. In order to select the interesting events (at a rate of a few events per second) from such a large amount of collisions, we need a trigger and data acquisition system. The DØ detector has a four level trigger system with three hardware levels (Level Ø, Level 1, Level 1.5) and one software level (Level 2) [40]. These are summarized in the following sections.

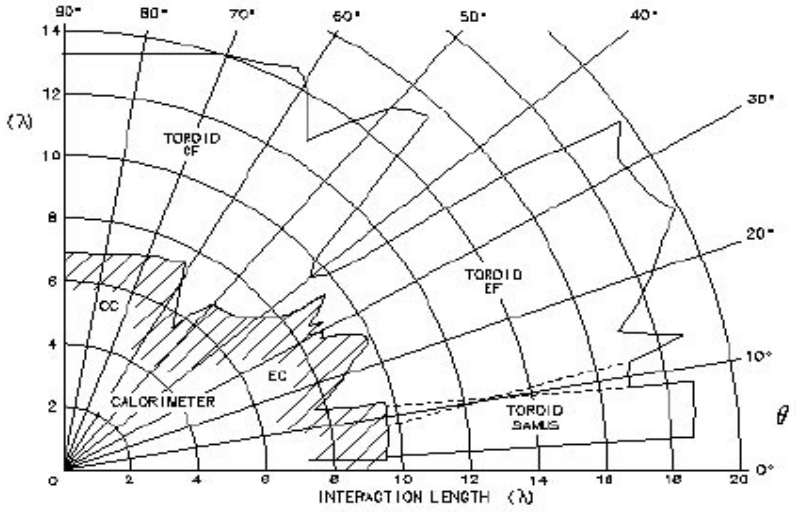

Figure 3.12: The nuclear interaction length of the DØ detector as a function of the polar angle (θ).

	WAMUS	SAMUS
Pseudorapidity coverage	$\|\eta\| \leq 1.7$	$1.7 \leq \|\eta\| \leq 3.6$
Magnetic field	2 T	2 T
Number of chambers	164	6
Interaction lengths	13.4	18.7
Bend view resolution	± 0.9 mm	± 0.35 mm
Non-bend (ξ) resolution	± 10 mm	± 0.35 mm
Gas composition	Ar 90%, CF_4 6%,	CF_4 90%,
	CO_2 4%	CH_4 10%
Avg. drift velocity	6.5 cm/μs	9.7 cm/μs
Anode wire voltage	+4.56 kV	+4.0 kV
Cathode pad voltage	+2.3 kV	—
Number of cells	11,386	5308

Table 3.7: Muon System Parameters.

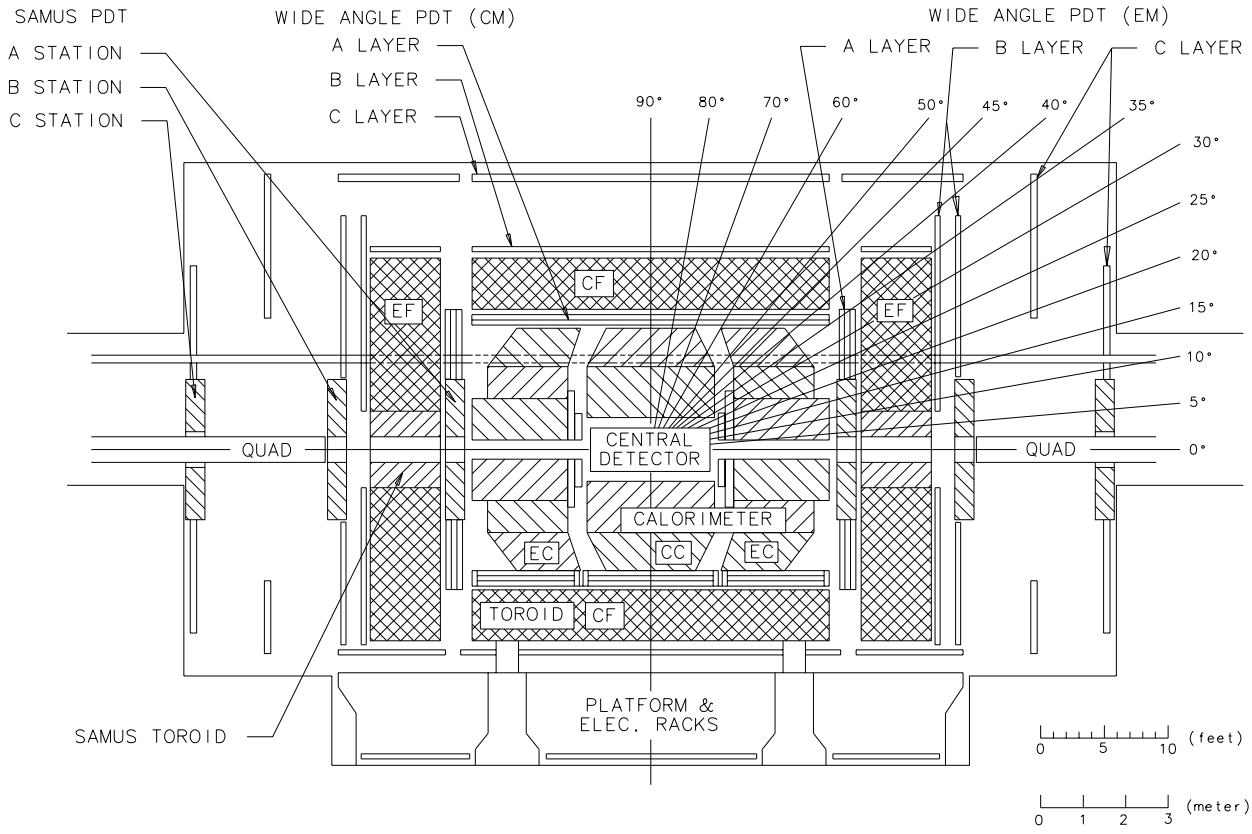

Figure 3.13: An elevation view of the DØ detector showing the muon system.

The Level Ø Trigger (LØ)

The Level Ø trigger indicates the occurrence of inelastic collisions and serves as the luminosity monitor for the experiment. It consists of two array of scintillator hodoscopes mounted between the FDC and EC calorimeters. The timing information from the LØ counters is used to determine the approximate interaction z position for subsequent trigger levels and the hit rates are used to monitor instantaneous luminosity. For example, a luminosity of $\mathcal{L} = 10^{30}$ cm^{-2}s^{-1} corresponds to a LØ rate of about 150 kHz.

The Level 1 (L1) and Level 1.5 (L1.5) Trigger

The Level 1 trigger elements collect the digital information from each of the detector sub-systems and flags an event for further examination. Many of the Level 1 triggers operate within the 3.5 μs time interval between beam crossings and contribute no dead-time. Others such as the muon trigger require several bunch crossing times to complete and are referred to as Level 1.5 triggers. The rate of successful Level 1 triggers is about 200 Hz.

The L1.5 is a DSP-based trigger and improves energy resolution by examining the energy in towers neighboring the L1 calorimeter EM towers. Additionally, energy sums are computed from adjacent hadronic towers, and the ratio $E_{\rm EM}/E$ is used for further background rejection. The rate is further reduced to 100 Hz using L1.5 trigger.

The Level 2 Trigger (L2)

The L2 trigger system is software-based and consists of a farm of 50 parallel VAX nodes connected to the detector electronics and triggered by a set of eight 32-bit high-speed (40 MB/s) data cables. The L2 nodes are coordinated through the host computer (see Figure 3.14). Event filtering is built around a series of filter tools each of which has a specific function related to a identification of a type of particle or event characteristic. These include tools for jets, muons, calorimeter EM clusters, track association with calorimeter clusters, $\sum E_T$ and missing $E_T(\not\!\!E_T)$. Other tools recognize specific noise or background conditions. The rate of successful Level 2 events is about 2 Hz.

The Main Ring Veto Triggers

The Main Ring passes through the course hadronic portion of CC and EC calorimeters. It is active during the production of the anti-protons and during new beam injection into the Tevatron. Beam loss from the Main Ring can cause spurious signals in the hadronic calorimeter and muon chambers. Typically this occurs once every 2.4 seconds when the protons are injected into the Main Ring and 300 ms later when the beam passes through transition [44]. A timing circuit linked to the Main Ring control system is used to set a hardware flag known as MRBS-LOSS. This is set every time the protons are injected and remains set for 400ms until the beam has passed through transition and muon system recovers. In addition, smaller beam losses occur with every passage of the beam. These are significant only if the

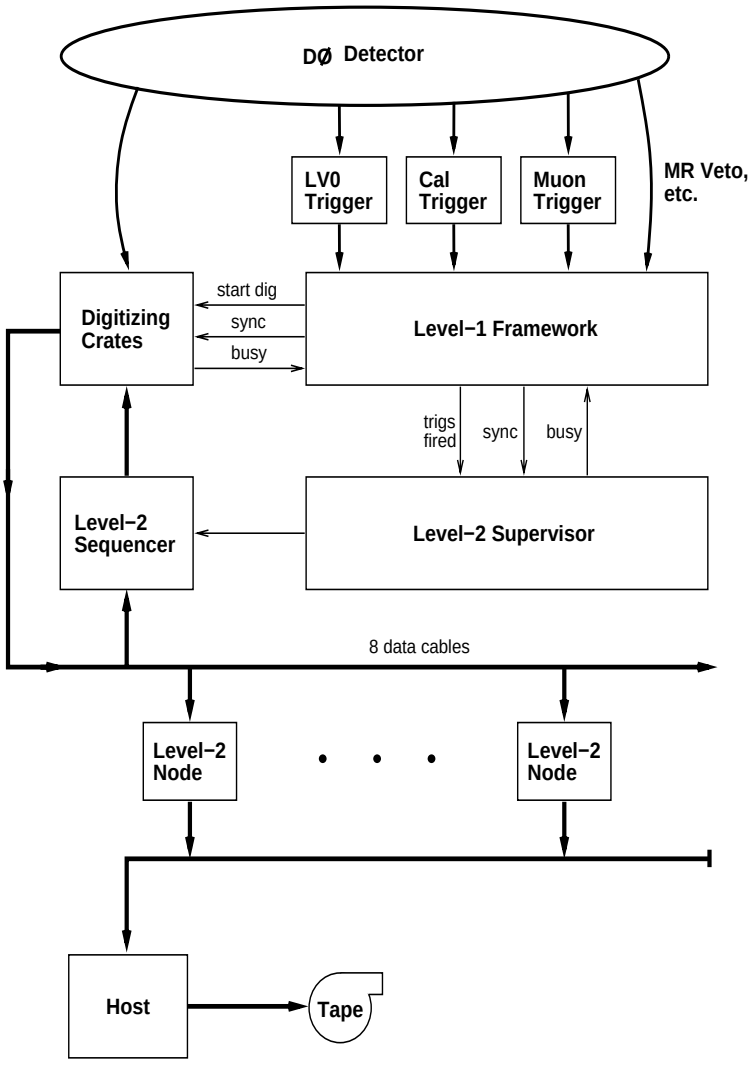

Figure 3.14: Block diagram of the Level 2 trigger and data acquisition system at DØ.

passage of the Main Ring beam coincides with the $p\bar{p}$ crossing in the Tevatron. This is flagged using another bit known as the MICRO-BLANK veto which is set if a Main Ring beam passes with $\pm$ 800 ns of a $p\bar{p}$ crossing.

More complete details about triggers (L1 and L2) used in the analysis are listed in Appendix A.

The Data Acquisition System

Figure 3.14 shows a schematic of the DØ data acquisition and its relationship to the Level 2 trigger hardware. The data from the detector sub-systems and

the LØ and L1 triggers are read out using eight high-speed data cables. Events passing the L2 trigger are passed on to the host computer for run-time monitoring and recording on tape. Events are buffered in the host until about 500 have been accumulated and then the file is closed and moved to 8mm data tape for permanent storage. The average size of an event is 500 kbytes.

Chapter 4

Event Reconstruction and Particle Identification

I recognize the lion by the paw.

- Jacques Bernoulli

The particles produced in the $p\bar{p}$ collisions generate signals in various parts of the detector. The raw data is stored on magnetic tape in the form of the analog and digital signals from the various detector sub-systems. The process of converting the raw information into a meaningful form suitable for physics analysis is known as reconstruction. At DØ this is done by program called DØRECO. This chapter describes the main features of DØRECO and the techniques it uses for particle identification.

4.1 DØRECO

The DØRECO package is a set of software algorithms which are used to perform particle and jet reconstruction. It contains about 150,000 lines of code and is run on a farm of silicon graphics 4D/35 computers at the Fermilab central computing facility. In addition to the reconstruction of the data DØRECO reduces the volume of the stored data by considerable fraction, thereby making data storage and handling easier. DØRECO creates three types of output data streams in ZEBRA [45] format: Standard (STA), Data Summary Tape (DST) and Micro-DST (μDST). The STA files are the largest in size and contain all of the raw data plus the complete results of the reconstruction. The DST files are a compressed version of the STA files containing only processed information and μDST files are series of analysis specific highly compressed DST files. DØRECO performs the three major listed in the following sections.

4.2 Tracking and Vertex Finding

The hits in the drift chambers are used to form track segments which are subsequently linked to form a track in the $r - \phi$ plane. For each track, directional information is specified by five parameters: the coordinates of a reference point (x_0, y_0, z_0), the polar angle θ and the azimuthal angle ϕ.

Once the tracking is done, the next step is to to determine the position of the interaction point[1]. The precise measurement of the z-position of the interaction vertex is very important to the determination of particle energies and the missing energy (energy imbalance) in an event. To do this, the CDC tracks are projected to the center of the detector and an impact parameter[2] is calculated for each track. Tracks with an impact parameter smaller than a critical value are retained for further analysis. Next each of these tracks is projected into the $r - z$ plane and the z axis intersection is computed and entered into a histogram. The z position of the vertex is then determined from the mean of a Gaussian fit to the distribution. Secondary vertex[3] solutions are also searched for around the initial peak. This method produces a resolution of about 2-3 cm in the vertex z position and multiple vertices can be separated if they are at least 8 cm apart. More information about tracking and vertexing can be found in reference [46]. Once the vertices have been identified, the calorimeter-based objects ($e, \gamma, \not\!\!E_T$, jets) are reconstructed.

4.3 Electron/Photon Reconstruction and Identification

Electrons and photons are identified by detection of the electro-magnetic energy clusters in the calorimeters with (electron) or without (photon) an associated track in the central tracking system.

4.3.1 Reconstruction

In DØRECO, the reconstruction of electron (photon) energy uses a nearest neighbor cluster algorithm [47]. Starting with the highest transverse energy (E_T) tower, the energy of adjacent towers are added provided that they are above an E_T threshold of 5 GeV, and that the cluster size is not too large. Each cluster is required to have at least 90% of its energy contained in the electro-magnetic calorimeter, and at least 40% of the total energy must be contained in a single tower. The centroid

[1]Sometimes there can be more than one interaction during the detector livetime

[2]The impact parameter is the shortest distance between track and z axis

[3]Here secondary vertex refers to a multiple interaction and it has nothing to do with the decays of the long-lived particles

of the cluster is then calculated using a log-energy weighting technique to take account for the transverse distribution of energy within the shower [44]. This gives a resolution of about $\approx$ 2mm. At this point the reconstruction program searches for a central detector track pointing from the interaction vertex to the calorimeter cluster within a road of size $\pm$ 0.1 in both $\Delta\eta$ and $\Delta\phi$. If one or more tracks are found, the object is classified as an electron candidate (PELC[4]). Otherwise, it is classified as a photon candidate (PPHO[5]).

4.3.2 Electron Identification

The sample of electron candidates collected after the reconstruction is contaminated with two types of background. The first is low energy charged hadrons which spatially overlap with energetic photons from π^0 or η decays and second is isolated photons convert to e^+e^- pairs in the beam pipe or the material of tracking chambers. Several tools have been developed to suppress these backgrounds while retaining most of the real electrons for further analysis. These are discussed below.

1. Electro-magnetic energy fraction (f_{EM})

The electro-magnetic energy fraction (f_{EM}) of a cluster is the fraction of its energy which is contained in electro-magnetic calorimetry. For electrons (photons), the EM calorimeter contains almost all of the energy, while charged hadrons will deposit only small fraction of their energy. Thus the EM energy fraction of a cluster, f_{EM}, serves as a powerful discriminant against charged hadrons. The Figure 4.1(a) shows the distributions of f_{EM} for real electrons and the backgrounds.

2. Isolation Fraction ($\mathcal{I}$)

Electro-magnetic clusters are narrow compared with the clusters produced by hadronic particles and they are usually contained in a cone of radius $R = 0.2$ ($R = \sqrt{\Delta\eta^2 + \Delta\phi^2}$) in $\eta - \phi$ space. DØ defines a isolation fraction ($\mathcal{I}$):

$$\mathcal{I} = \frac{E_{Total}(R = 0.4) - E_{EM}(R = 0.2)}{E_{EM}(R = 0.2)} \tag{4.1}$$

where $E_{Total}(R = 0.4)$ is the total energy contained in the cone of radius 0.4 and $E_{EM}(R = 0.2)$ is the electro-magnetic energy in a core cone of radius 0.2. This gives a good measure to select isolated electrons. Figure 4.1(f) shows the $\mathcal{I}$ for electrons and background sample.

3. Shower Shape - The Covariance Matrix (χ^2)

Electro-magnetic showers can also be characterized by the fraction of the cluster energy deposited in each layer of the calorimeter. These are correlated and are also dependent on the incident electron energy. If an electron deposits large

[4]PELC is the definition of a electron at DØ detector

[5]PPHO is the definition of a photon at DØ detector

amount of energy in the first layer then it will deposit relatively small fraction of energy in the subsequent layers and vice versa. To obtain the discrimination against hadrons and particle jets, we can exploit these correlations. Based on test beam studies and Monte Carlo simulations of electrons with energies between 10 and 150 GeV, a 41 variable covariance matrix (H-matrix) has been constructed. This represents the correlation between the energy depositions in individual layers [48]. Each variable characterizes a part of the profile of the electro-magnetic shower. A χ^2 is then computed from the observed shower shape and the covariance matrix representing the expected shower shape. The lower the χ^2, the more the candidate cluster resembles an electron shower. Figure 4.1(b) show the χ^2 distributions for sample of electron and background tracks.

4. Track Ionization (dE/dx)

Isolated photons that convert to e^+e^- pairs inside the beam pipe or the material of the tracking chambers may result in tracks which match to an EM cluster. Since there is no central magnetic field the two tracks do not separate and are often too close to resolve. However, in the tracking chambers the ionization energy per unit length (dE/dx) of a e^+e^- pair is about twice that of a single charged particle. Figure 4.1(d) shows the dE/dx distribution for real electrons and background. The electron spectrum has only one peak, but the distribution for the background has two clear peaks where the second peak comes from photon conversions.

5. Track match significance (σ_{trk})

A source of background for electrons is photons from the decay of π^0 or η mesons. The photons do not leave tracks in the central detector, but a track might appear if a charged particle is nearby. This background can be reduced by demanding a good spatial match between calorimeter cluster and the nearby tracks . The significance S, of the matching between these quantities is:

$$S = \sqrt{\left(\frac{\Delta\phi}{\sigma_{\Delta\phi}}\right)^2 + \left(\frac{\Delta z}{\sigma_{\Delta z}}\right)^2} \tag{4.2}$$

where $\Delta\phi$ and Δz are the azimuthal and z axis mismatch, respectively and $\sigma_{\Delta\phi}$ and $\sigma_{\Delta z}$ are the corresponding resolutions. In the case of EC track matching, the z is replaced by the radial distance r.

6. TRD efficiency (ϵ_t)

The response of the Transition Radiation Detector (TRD) is characterized by the efficiency variable ϵ_t:

$$\epsilon_t(E) = \frac{\int_E^\infty \frac{\partial N}{\partial E'}(E')\,dE'}{\int_0^\infty \frac{\partial N}{\partial E'}(E')\,dE'} \tag{4.3}$$

where E is the total energy recorded in the TRD minus that recorded in the layer with the largest signal and $\frac{\partial N}{\partial E'}$ is the energy spectrum from a sample of $W \to e\nu$

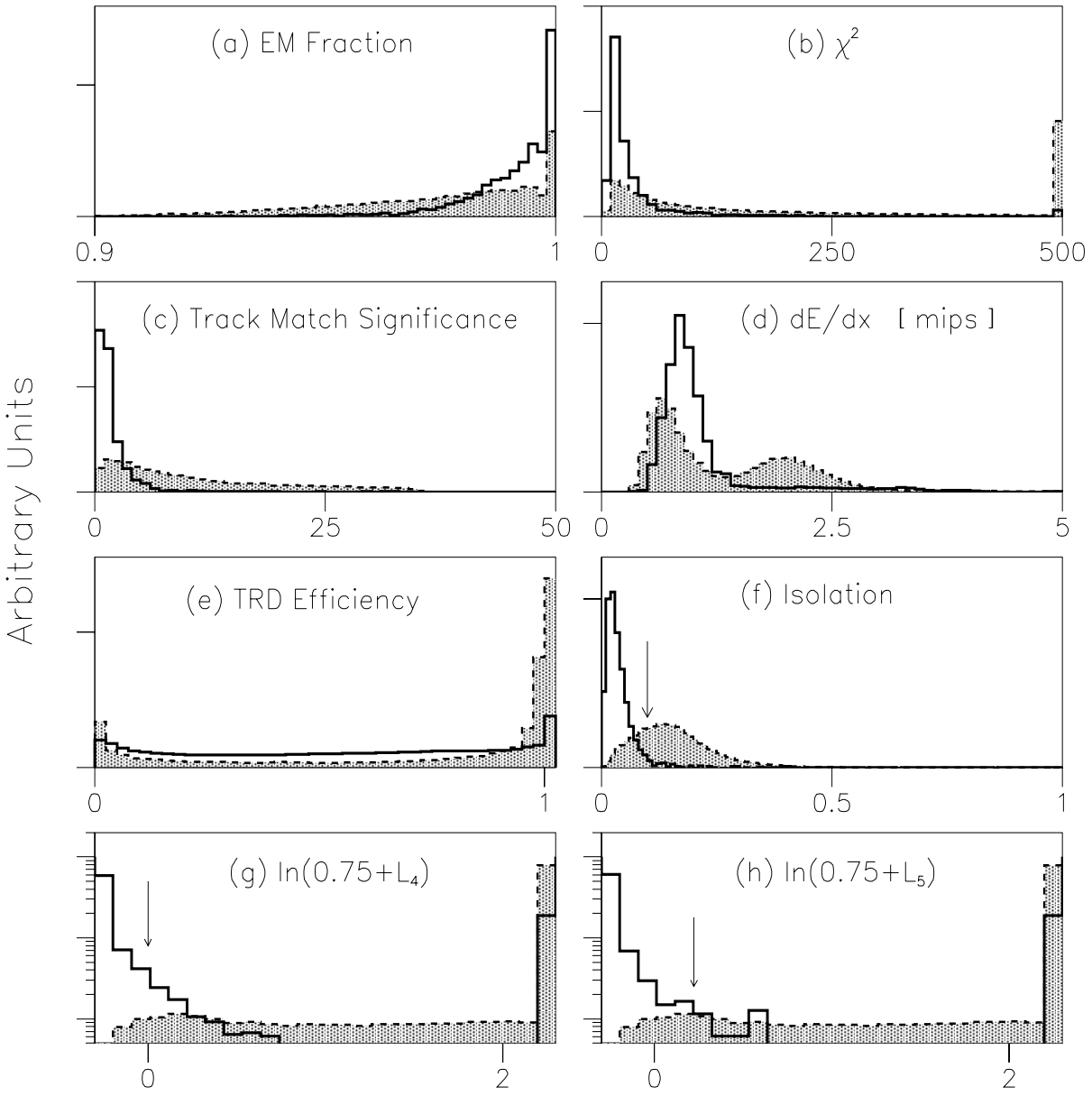

Figure 4.1: Various quantities used in electron identification (a) EM fraction ($f_E M$) (b) χ^2 (c) Track match significance (σ_{trk}) (d) Ionization (dE/dx) (e) TRD efficiency (ϵ_t) (f) Isolation ($\mathcal{I}$) (g) 4 variable likelihood (L_4) (h) 5 variable likelihood (L_5). The unshaded distributions are from electrons in $Z \to ee$ and $W \to e\nu$ events and shaded distributions are from electro-magnetic clusters in inclusive jet data.

events [49]. Since ϵ decreases as E increases, hadrons will tend to have values near unity while the distribution from electrons is roughly uniform over the allowed range of zero to one (See Figure 4.1(e)).

7. Likelihood ratio (L_4, L_5) [50]

In order to extract the maximum possible background rejection while keeping a high acceptance for real electrons the DØ electron identification algorithm uses a 4 or 5 variable likelihood function. The 4 variable likelihood, L_4 uses the combinations of $f_{EM}, \chi^2, \sigma_{trk}$, and dE/dx and the 5 variable likelihood, L_5 uses the 4 variables from L_4 and ϵ_t. The functions (L_4 or L_5) are constructed using the probability density distributions: $P_1(f_{EM}|h), P_2(\chi^2|h), P_3(\sigma_{trk}|h), P_4(dE/dx|h)$ and $P_5(\epsilon_t|h)$, where $h = e$ for electrons and $h = b$ for background. The results are shown in Figure 4.1(g,h) for L_4 and L_5 respectively. The analysis described in this thesis uses the 5 variable likelihood.

4.3.3 Electromagnetic Energy Resolution and the Absolute Energy Scale

The energy resolution of electrons and photons can be expressed by the relation:

$$\left(\frac{\sigma}{E}\right)^2 = C^2 + \frac{S^2}{E} + \frac{N^2}{E^2} \tag{4.4}$$

where E is the mean energy of the incident electron, C is a constant term due to calibration errors, S is the sampling fluctuation of the liquid argon calorimeter, N corresponds to a noise term due to the contribution of electronic noise the effects of the natural and radioactivity of the Uranium in the calorimeter. For electrons the resolution is:

$$\frac{\sigma}{E} = \frac{0.15}{\sqrt{E}} \oplus 0.03 \tag{4.5}$$

The energy scale of the electro-magnetic calorimeter has been calibrated by setting the measured invariant mass peak of $Z \to e^+e^-$ to the measured LEP value [51]. Lower mass resonances ($\pi^0 \to \gamma\gamma$, $J/\Psi \to ee$) have also been used to cross check the calibrated scale at lower energies.

4.4 Muon Reconstruction and Identification

Muons interact weakly with matter and have long enough lifetime to pass through all of the detector material without decaying. They are reconstructed and identified using the hits and timing information from the muon spectrometers. Since a muon deposits a little of its energy in the calorimeter as it passes through, the resulting minimum ionizing trace can also be used for muon identification. The

momentum of the muon is measured from the bend in the track produced by the magnetic field of the muon spectrometer.

4.4.1 Reconstruction

The muon reconstruction is similar to that of CDC track reconstruction except for the differences in algorithm which take account of the geometry of the muon system. DØRECO uses timing information to determine the position of the hits in all the planes (A, B and C) of the muon system. For the B and C chambers, hits in four out of six possible planes are required and for the A chamber this requirement is two out of four. The hits from the planes of A, B and C chambers are then used to form tracks. Because the B and C chambers are outside the magnetic toroid and the A chamber is inside, the tracking is done separately before and after the magnet. The segments are then matched, and a measurement of the momentum is made by measuring how much the track bends. Lastly, a global fit [52] is performed using the tracks in the muon chamber, the interaction vertex, the energy profile in the calorimeter, and the track from the CDC/FDC (if present). Additional corrections are made for the effects of multiple scattering in the calorimeter and the iron toroid and for the expected energy loss in the calorimeter.

4.4.2 Muon Identification

The main sources of muon background are cosmic rays, combinatoric errors in track reconstruction and random hits from the beam spray. The backgrounds from hadronic punch-through and π/K decays are negligible [53]. As in the electron/photon case, there are several other quality parameters which are used for the muon identification.

1. Impact Parameter (IP) Requirements

To provide rejection against in-time cosmic ray muons, each track is required to project back to the interaction vertex in both the bend and non-bend views and the PDT hits must be within ± 100ns of the beam crossing time. This is done using the time information from the cosmic ray scintillators counters and by using cuts on the values of bend view (BV) and non-bend (NB) view impact parameters.

The NB impact parameter tests the track and vertex consistency in the $x-y$ plane and the BV impact parameter in the $x-z$ plane. These are combined to define a pseudo 3-D impact parameter, $IP = \sqrt{IP_{BV}^2 + IP_{NB}^2}$, which is required to be less than 20 cm for a good muon candidate.

2. Muon Track Quality (IFW4)

DØRECO computes track quality flag referred to as IFW4. This contains the following information for each track:

- Is there a missing PDT Plane on the track?

- Is the non-bend view impact parameter $\geq$ 100 cm ?
- Is the bend view impact parameter $\geq$ 80 cm ?
- Does the non-bend view fit have a hit residual rms $\geq$ 7 cm ?
- Does the bend view fit have a hit residual rms $\leq$ 1 cm ?

IFW4 is incremented by one unit for each failure of above checks. Thus, IFW4 = 0 means no failure (a perfect track) and IFW4=1 means the track failed only one of the criteria. The IFW4 cut is a very powerful tool to reduce the cosmic rays and the fake track backgrounds constructed from random hits.

3. Calorimeter Verification (MTC)

The muons leave a distinctive energy deposition (MIP) as they pass through the calorimeter. Therefore it is important to examine the calorimeter cells along the track path of the muon. For this purpose, DØ has developed a software package known as MTC which stands for the Muon Tracking in the Calorimeter. This uses the calorimeter to identify localized depositions of energy (no showers) and provides information independent of the muon chambers. A more detailed description of the MTC package can be found in reference [54]. For this analysis most relevant parameters provided by the MTC package are HFRAC and EFRCH1:

HFRAC: This is the fraction of hadronic calorimeter layers used in track fitting. For a good MIP muon it should be 100%. HFRAC equals 0.7 means that no more than one layer of the hadronic calorimeter can be missing.

EFRCH1: This is the fraction of the total energy deposited in a 3 $\times$ 3 calorimeter cell region around the track in the last hadronic layer of the calorimeter. If HFRAC is less than 1 (100%), then the last layer must be hit. So one must have EFRCH1 $>$ 0 if HFRAC $<$ 1.

The MTC package uses information which was available only for the 1994-96 runs. For the earlier data (Run 1a) another quantity called calmip was used. This required a matching CDC(FDC) track and 1 GeV in the calorimeter cells hit by the muon or no CDC track match and 1.5 GeV in the hit cells.

4. Isolation, (ΔR cut)

Since this analysis will deal primarily with muons coming from W boson decays, we require each muon to be isolated from any other activity (electro-magnetic or hadronic) in an event. A muon is defined as "isolated" , if the separation between the muon and the nearest object (electron/photon or jets) is greater than certain value in the $\eta - \phi$ space. This is done by computing the ΔR[6] between muon and its nearest neighbors. Two cuts were used, one for muon-jet separation, which required $\Delta R(\mu, jet) > 0.5$ and one for muon-electron/photon separation which required $\Delta R(\mu, e/\gamma) > 0.25$.

[6] $\Delta R = \sqrt{\Delta\eta^2 + \Delta\phi^2}$

4.5 Jet Reconstruction and Identification

Quarks other than top and gluons which are produced in the $p\bar{p}$ collisions hadronize into colorless particles. Some of these have energies high enough to allow further decay or radiation resulting in the formation a cascade of particles. These appear in a cone around the original direction of motion of the parent particle and show up as cluster of tracks in the central tracking system and a cluster of energy in the calorimeter. These groupings are classified as jets of particles because of their close spatial correlations.

4.5.1 Reconstruction

There are several algorithms which could be used for jet reconstruction. The most common algorithm used in the $p\bar{p}$ environment is the "cone algorithm" [55]. This is based on summing the observed calorimeter transverse energy within a fixed radius cone in $\eta - \phi$ space. This analysis used a R[7] $= 0.5$ cone algorithm. The main steps in the reconstruction process are:

Pre-clustering: The transverse energy is calculated for all of the calorimeter towers which are then sorted in order of decreasing E_T. Beginning with the highest E_T tower, clusters are formed by adding the towers within a radius R of the highest energy tower. The process is repeated for the remaining calorimeter towers.

Cone Clustering: The centroid of each cluster is calculated by performing an E_T weighted sum of the tower (η, ϕ) positions. Then the whole process is iterated using the jet centers as cluster seeds until the position of the cluster converges.

Merging and Splitting: Once the cone clustering is completed, some cells may have been assigned to more than one jet. If two jets share cells, the fraction of the total energy which is shared between them is examined. If the fraction is greater than 50%, the two jets are merged together and the jet axis is recalculated from the centroid of the cells in the merged jet. Otherwise the jets are split and the shared cell is assigned to the closest jet. At this stage all jets with transverse energy $E_T \geq 8$ GeV are retained for further analysis.

4.5.2 Jet Identification

In order to remove any fake jets produced by calorimeter or Main Ring noise, DØ has developed a set of quality cuts based on the jet characteristics. These are cuts on the jet electro-magnetic fraction (EMF) which is used to distinguish between electrons/photons and jets, the Hot Cell Energy Fraction (HCF) which helps reduce calorimeter noise and Coarse Hadronic Energy Fraction (CHF) which

[7] $R = \sqrt{\Delta\eta^2 + \Delta\phi^2}$

helps to remove activity caused by the Main Ring. A detailed discussion of these can be found in reference [56]. The various kinematic quantities defining a jet are:

$$E_T = \sqrt{E_x^2 + E_y^2} \tag{4.6}$$

$$\phi^{jet} = tan^{-1}\left(\frac{E_y}{E_x}\right); \qquad \theta^{jet} = cos^{-1}\left(\frac{E_z}{\sqrt{E_x^2 + E_y^2 + E_z^2}}\right) \tag{4.7}$$

4.5.3 Jet Energy Corrections

The measured jet energy usually is not equal to the energy of the original parton which formed the jet. There are several effects which contribute this and which are corrected for using a DØ software algorithm called CAFIX [57]. This corrects the reconstructed jet energies for:
- The non-uniformities in the calorimeter and non-linear response for low energy particles (< 2 GeV).
- Noise due to electronics and the natural radioactivity of uranium absorber.
- The energy deposited in the jet cone from partons not produced in the hard scattering process. This is typically from the soft interactions of spectator partons within the proton and the anti-proton and is known as the underlying event.

The resulting correction is a function of both η and the transverse energy and takes the form:

$$E_{jet}^{corr} = \frac{E_{jet}^{meas} - O}{R(1 - S)} \tag{4.8}$$

where O is the offset energy due to both uranium noise and the underlying event, R is the calorimeter response to jets and S is the fraction of the jet energy for out of cone showering.

4.6 Missing Transverse Energy ($\not\!\!E_T$)

The presence of neutrinos in an event is inferred by the presence of significant imbalance in the energy measured in the detector. Since muons escape the calorimeter depositing only a small fraction of their energy, the apparent missing transverse energy ($\not\!\!E_T^{cal}$) must first be corrected for the muon energy to obtain a true measure of the missing energy in an event.

We define $\not\!\!E_T^{cal}$ as:

$$\not\!\!E_T^{cal} = \sqrt{(\not\!\!E_T^{cal})_x^2 + (\not\!\!E_T^{cal})_y^2} \tag{4.9}$$

where $\not\!\!E_T^{cal}$ is summed over all of the calorimeter. For events which have muons, the transverse momentum of muons is subtracted from $\not\!\!E_T^{cal}$ to compute the total missing energy $\not\!\!E_T$:

$$(\not\!\!E_T)_x = (\not\!\!E_T^{cal})_x - \sum_i p_x^{\mu_i} \tag{4.10}$$

$$(\not\!\!E_T)_y = (\not\!\!E_T^{cal})_y - \sum_i p_y^{\mu_i} \tag{4.11}$$

$$\not\!\!E_T = \sqrt{(\not\!\!E_T)_x^2 + (\not\!\!E_T)_y^2} \tag{4.12}$$

Chapter 5

Analysis Tools

...the clarity of the thoughts should also be accompanied by the clarity of the technique.

- Piet Mondriaan

5.1 Artificial Neural Networks

At many tasks, the human brain is superior to any computer. A one year old infant is much better and faster in recognizing patterns than any artificial intelligence system running on the fastest computer. How does brain do it? It has been well established that the basic unit of signal processing in the brain is a *neuron*. There are about 10^{11} inter-connected neurons in a human brain, each of which has essentially the same structure (See Figure 5.1). The signals arriving at a neuron are summed and if this sum is greater than a threshold, the neuron is "fired". After firing the neuron returns back to its initial state. The signals are electrical pulses cause by bio-chemical changes. The fired neuron in turn send a signal to the connected neurons which may result in the firing of other neurons in the network. The key process is the linear summations of inputs and a non-linear transformation of the sum.

Artificial neural networks (ANN) are mathematical models that are inspired by the connections and the functioning of neurons in biological systems. They have given rise to a branch of research called neural computing which has applications in many disciplines. The basic concept is based on two ideas, the topology of the nodes/connections and the transfer functions which relate the input and output of each node. A node receives input data through its input connections, performs a very simple operation (weighted sum and some kind of thresholding function), and then passes the result on its output connection(s) for use by other nodes. From a neurophysiological point of view these models are extremely simple but are still are

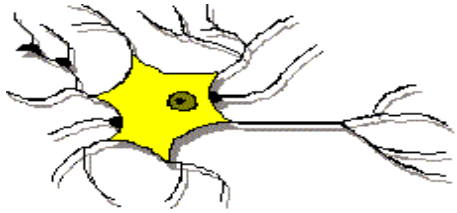

Figure 5.1: A drawing of a neuron.

valuable in gaining insight into the principles of biological "computation".

Artificial neural networks are often used as a way of optimizing a classification (or pattern recognition) procedure and have been applied to many pattern recognition problems in physics [7, 59, 60, 61] with a notable success. They usually have more input than output nodes and may thus viewed as performing a dimensionality reduction on input data. This makes the neural network a multivariate technique which exploits the correlations among different variables and then builds a representation by mapping the multidimensional input feature space into an output space of fewer dimensions.

5.2 The Neural Network as a Multivariate Classifier

A multivariate classifier is a technique which assigns objects to classes [62]. The objects can be different data types such as signal and background in our case. Each data type is assigned to a class which in the present context is 0 for background and 1 for signal. Discrimination is achieved by looking at the class to which the data belongs. The technique fully exploits the correlations among different variables and provides a discriminating boundary between the signal and background.

A pattern vector is characterized by a set of attributes or variables such as $E_T^e, P_T^\mu, \not\!\!E_T, \not\!\!E_T^{cal}, H_T$, etc. Each event is a point in the multidimensional space (known as the feature space) spanned by the variables. The dimensionality of the problem is reduced by mapping this input feature space onto one or more outputs and a Bayes discriminant is used to provide the optimal partitioning of a given mixture of signal and background events. The discriminant is defined by the ratio:

$$R = \frac{P(S|X)}{P(B|X)} = \frac{P(X|S)P(S)}{P(X|B)P(B)} \tag{5.1}$$

where

$P(S|X)$ = probability that an event characterized by X is a signal event.

$P(B|X)$ = probability that an event characterized by X is a background event.
$P(S)$ = *apriori* probability of an event being signal event.
$P(B)$ = *apriori* probability of an event being background event.
$P(X|S)$ = Likelihood function for the signal P(S)
$P(X|B)$ = Likelihood function for the background P(B)
The ratio of $P(S)/P(B)$ is the ratio of the signal to background cross section with the constraint that $P(S) + P(B) = 1$.

Several multivariate techniques available in the literature and have been used in high energy physics analyses [62].
- H-Matrix and Fisher's discriminant
- Probability Density Estimation
- Neural Networks

For this analysis we have adopted the neural network approach. ANN's have the capacity to learn, remember, and create relationships amongst the data. There are many different types of ANN but the feed forward types are most popular among high energy physicists. Feed forward implies that the information can only flow in one direction and output can be interpreted as an approximation to the Bayes discriminant of Equation 5.1 [65]. This determines directly the probability ($P(S|X)$) that an event characterized by X is from the signal class.

5.3 A Mathematical Model of the Neural Network

As we have seen earlier, neural networks provide powerful paradigms for event classification problems. The mathematical model of neural network used by Physicists and Engineers is a very simple one. The three basic functions of a biological neuron:
- sum up all the information arriving at inputs (node/neuron);
- if sum is greater than some threshold, fire the neuron
- after firing, return back to quiescent state and send a signal to each of the other neurons in the network

It is a straightforward matter computationally to make an artificial neuron with these characteristics. This is known as an elementary perceptron (see Figure 5.2). The perceptron is a simple feed forward system in which the decision making unit has several input connections and a single output connection. Mathematically a perceptron with one output can be written as:

$$O(x_1, x_2, ...x_n) = g(\frac{1}{T}\sum_i w_i x_i + \theta)) \tag{5.2}$$

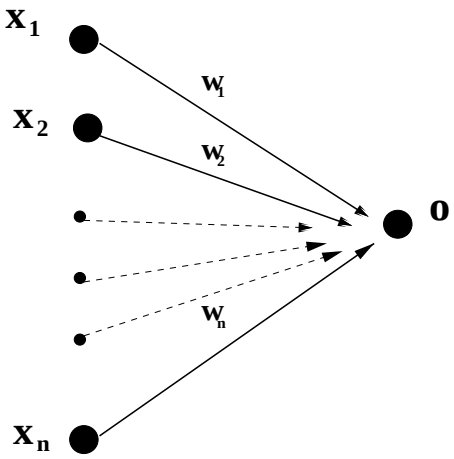

Figure 5.2: An elementary perceptron

where

x_i are the input pattern vectors;

O is the output;

w_i's and θ are the independent parameters called weights which connect the input nodes to the output node and the threshold of the output node respectively;

$\beta = 1/T$, is the called the inverse temperature;

g is a non linear transfer function and typically takes of the following form:

$$g(x) = \frac{1}{1 + e^{-2x}} \tag{5.3}$$

This is also known as a sigmoid function (see Figure 5.3).

A pattern vector x_i is multiplied by the connection weights w_i, so that each piece of information appears at the perceptron as $x_i w_i$. Next the perceptron sums all the incoming information to give $\sum w_i x_i$ and applies the transfer function (g) to give the output $g(\sum w_i x_i)$ (See Equation 5.2).

There are several limitations to the simple perceptron [66]. A feed-forward network with intermediate or "hidden layers" can be used to overcome these and can implement any continuous function [68]. Figure 5.4 shows a feed forward neural network with one hidden layer. In case of a one hidden layer the output of the neural network is:

$$O(x_1, x_2, ...x_n) = \mathbf{g}(\frac{1}{T}\sum_k w_k \mathbf{g}(\frac{1}{T}\sum_i w_{ki} x_i + \theta_k) + \theta) \tag{5.4}$$

where

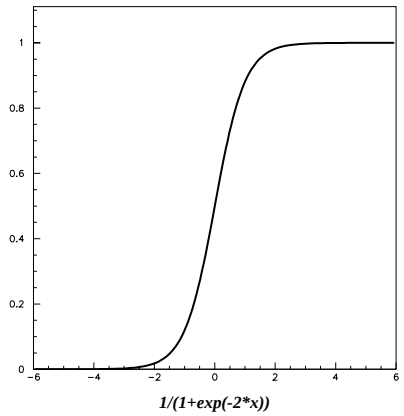

Figure 5.3: A sigmoid function

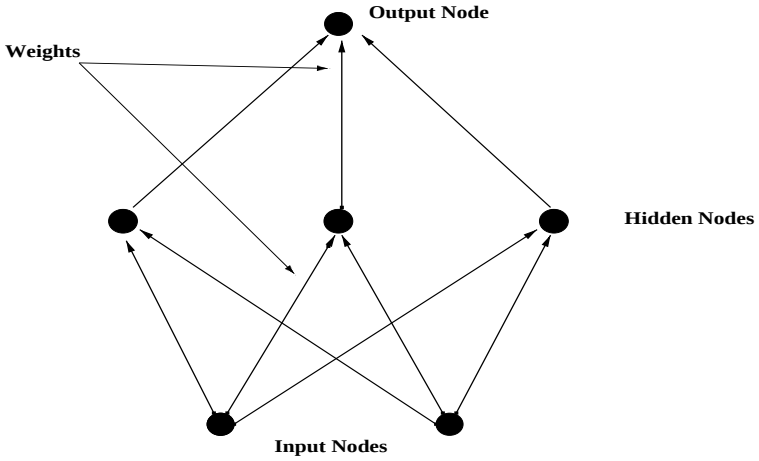

Figure 5.4: A feed forward neural network with one hidden layer

w_{ki}'s are the weights connecting the input nodes (i) to hidden nodes (k) and the w_k's connects the hidden nodes to the output node.

θ_k and θ are the thresholds of the hidden and output node, respectively

5.3.1 Learning/Training of the Perceptron

The behavior of a perceptron is determined by independent parameters known as weights and thresholds. The total number of independent parameters in a neural

network with a single hidden layer is given by:

$$N^{\text{Indep}} = (N^{\text{IN}} + N^{\text{ON}}) \times N^{\text{HN}} + N^{\text{HT}} + N^{\text{OT}} \tag{5.5}$$

where

N^{IN} are number of input nodes
N^{ON} are number of output nodes
N^{HN} are number of nodes in a hidden single layer
N^{HT} are number of thresholds in a hidden single layer
N^{OT} are number of output thresholds

Learning is the process of adjusting these parameters and information is stored as the values of the parameters values. During learning, the novice perceptron is shown examples of what it must learn to interpret. These constitute the training set which consists of two parts: the training stimulus (training data) which is a collection of inputs to the perceptron, and the training target which is a desired output for each kind of stimulus.

Mathematically, the goal of training is to minimize a measure of the error on the fit. The mean square error function E averaged over the training sample is defined by Equation 5.6 and its value is used in updating weights and thresholds.

$$E = \frac{1}{2N_p} \sum_{1}^{N_{p=1}} \sum_{i=1}^{N} (O_i^{(p)} - t_i^{(p)})^2 \tag{5.6}$$

where

O_i is the output of the neural net in Equation 5.4
t_i is the training target (in our case, 0 for background and 1 for signal)
N_p are the number of patterns (events) in the training sample
N are the number of network outputs

There are several algorithms available for error minimization. Gradient descent is the least sophisticated and most widely used for High Energy Physics problems. This is also known as the back propagation learning algorithm (BP) [67]. Here the weights are updated using:

$$\omega_{t+1} = \omega_t + \Delta\omega_t \tag{5.7}$$

where

$$\Delta\omega_t = -\eta \frac{\partial E_t}{\partial \omega} = -\eta \nabla E_t \tag{5.8}$$

and ω is the vector of weights and thresholds used in the network; t (t+1) refers to the previous (current) training cycle and η is the learning rate which is identical in all the directions of ω space. To speed up the convergence, a momentum term (α, typically < 1) is added and to help stabilize the learning process.

$$\Delta\omega_{t+1} = -\eta \frac{\partial E_t}{\partial \omega} + \alpha \Delta\omega_t \tag{5.9}$$

5.4 The Neural Network Package

This study was carried out using the JETNET 3.0 package developed at CERN and the University of Lund [68]. It is available via anonymous *ftp* from `thep.lu.se` or from `freehep.scri.fsu.edu`. The program is designed for DEC Alpha, SUN, Apollo, VAX, IBM and Hewlett−Packard machines with a Fortran77 compiler. It has been implemented in the DØ framework and reads information from row−wise ntuple files. The architecture is a feed forward structure with default values which are provided for some of the network parameters. The other parameters are chosen by maximizing the relative significance for signal as explained below. The weights are updated using the back propagation algorithm.

5.5 Neural Network Architecture and Learning Parameters

There are several different architectures and parameters available for a neural network. Many different studies have been done to investigate the effect of architecture and training parameters on the performance of a neural net [69]. Here we describe the process of choosing an architecture and the parameters for our classification problem.

5.5.1 Hidden Layers and Hidden Nodes

The present problem involves the discrimination between hyper volumes of signal and background. We have used one hidden layer because it is sufficient for most classification problems [66]. To ensure convergence and stability, the total number of training patterns (events) must be significantly larger ($\sim$ 20-40 times) than the number of independent parameters ($N^{\rm Indep}$) of the neural network (see Equation 5.2). Taking this in consideration, we tried networks with 5 to 7 hidden nodes.

To investigate the impact on the learning parameters, we trained a neural net with 3000 signal ($t\bar{t}$, m_t = 170 GeV) events and 3000 background (1000 QCD fakes, 1000 WW and 1000 $Z \rightarrow \tau\tau$) events. The network was then tested with an independent set of 5000 signal and background events. The relative significance (S/B) was calculated for the signal and background events surviving the neural network with a discriminant cut of ≥ 0.7. This is shown as a function of each of the network parameters in Figure 5.5. The results are discussed in detail below.

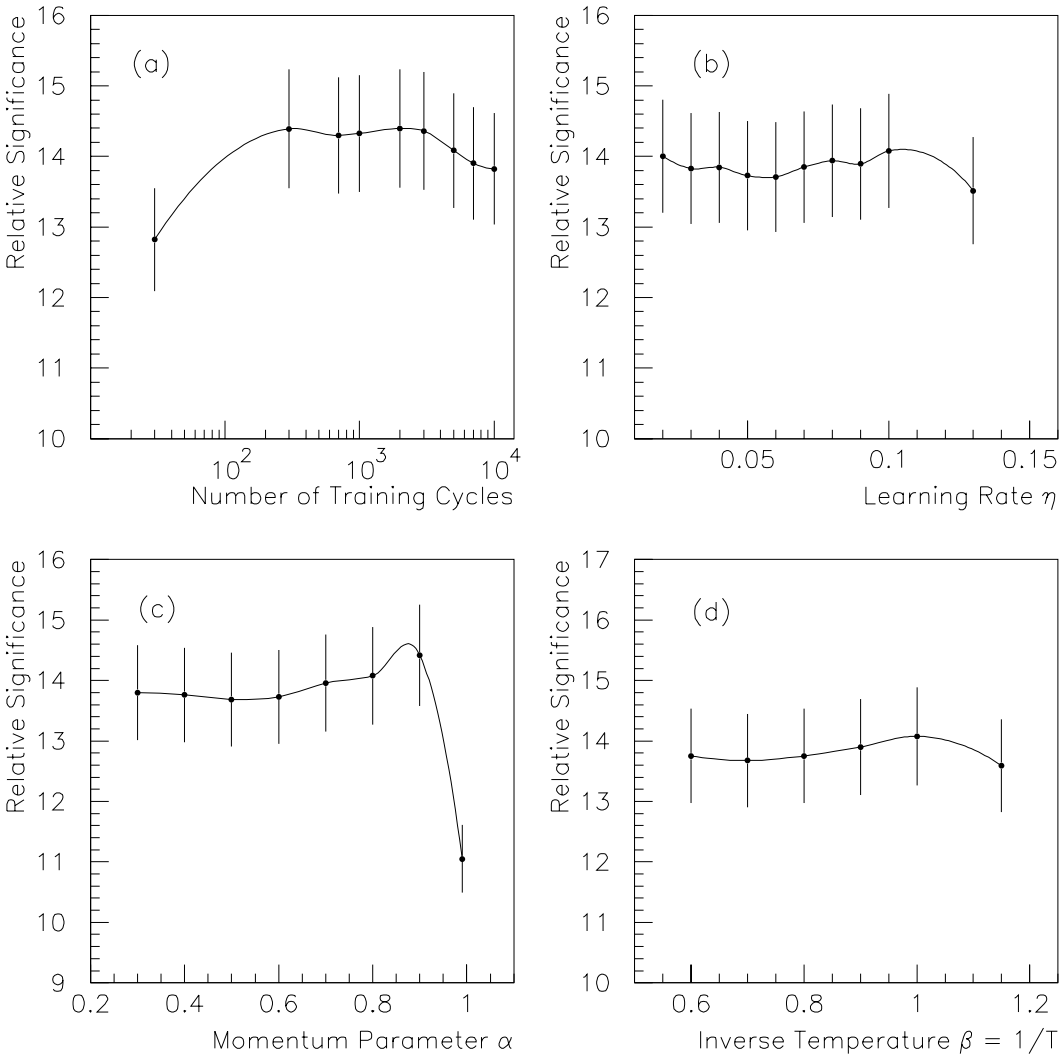

Figure 5.5: Relative significance (signal/background) for various network parameters (a) Number of Training cycles, (b) Learning Rate η, (c) Momentum Parameter α and (d) Inverse temperature $\beta = 1/\mathrm{T}$

5.5.2 Number of Training Cycles

We varied number of training cycles from 30 to 11000 to investigate the effect of training on network performance. The results shown in Figure 5.5 (a) indicate that the network performance is stable if 500-5000 training cycles are used.

5.5.3 Learning Rate (η)

The Learning rate (η) is a factor in updating the weights. We have varied its value between 0.01 and 0.15 (see Figure 5.5 (b)) and find that the results are relatively insensitive within this range. For our analysis we chose a learning rate of 0.1.

5.5.4 Momentum Parameter (α)

A momentum term, which typically varies between 0 and 1, can be used to stabilize learning and speed up convergence. We varied α between 0.2 and 0.99. Based on these studies (Figure 5.5 (c)) we chose a value of 0.8 for α.

5.5.5 Inverse Temperature (β)

The inverse temperature determines the steepness of the transfer function $g(x)$. Figure 5.5 (d) shows a plot of relative significance as a function of inverse temperature ($\beta = 1/\mathrm{T}$). As with η, we find little sensitivity to change and we selected a value of 1 for our analysis.

From these studies we conclude that the network performance depends only weakly on the network parameters. In the following chapter we go on to consider the sensitivity to the event samples used in training.

Chapter 6

Data Collection, Detection Efficiencies and Monte Carlo Simulations

Science with patience: Torture is certain.

- Arthur Rimbaud

The data used in this analysis were collected in three separate data taking runs with the DØ detector between the summer of 1992 and the spring of 1996. These are collectively referred to as the data from Run 1. During this time the Tevatron operated at the center-of-mass energy of 1.8 TeV and delivered beam luminosities of upto 3 $\times 10^{31}$ cm^{-2}s^{-1}.

In this chapter we discuss the factors relating to the data taking, the behavior of the apparatus (detection efficiencies) and the simulation of the detector response.

6.1 Data Collection

6.1.1 Integrated Luminosity and Data Sample

At DØ the instantaneous luminosity, $\mathcal{L}$ is determined and monitored using Level Ø trigger system. By measuring the rate, $\mathcal{R}$ of inelastic $p\bar{p}$ scattering the instantaneous luminosity is given by.

$$\mathcal{L} = \frac{\mathcal{R}}{\sigma_{L\emptyset}} \tag{6.1}$$

where $\sigma_{L\emptyset}$ is the cross section subtended by the LØ trigger. For Run 1, $\sigma_{L\emptyset}$ was measured to be 46.7 $\pm$ 2.5 mb [71]. The total integrated luminosity ($\int \mathcal{L}dt$) is then

simply obtained by integrating the instantaneous luminosity $\mathcal{L}$.

For this analysis, we have used the combined integrated luminosities of 1992-93, 1994-95 and 1996 data taking runs which corresponds to:

$$\int \mathcal{L}dt = 108.3 \pm 5.7 pb^{-1} \tag{6.2}$$

which was taken using the triggers described below.

6.1.2 Triggers

The experimental signatures of the $t\bar{t} \rightarrow e\mu$ dilepton channel event consists of a high transverse energy electron and muon, two or more jets and a significant amount of missing transverse energy. The level 1 and 2 triggers used for data collection are a direct reflection of this and are summarized in Table 6.1. A more detailed description is given in Appendix A. In addition to these requirements, events collected during MRBS-LOSS and MICRO-BLANK gates were rejected in the subsequent off-line analysis.

Run	Triggers
Run 1a	**mu-ele OR ele-jet-high OR mu-jet-high**
Run 1b	**mu-elc OR ele-jet-high OR mu-jet-high OR mu-jet-cent**
Run 1c	**mu-ele-high OR ele-jet-high OR mu-jet-cencal OR mu-jet-cent**

Table 6.1: Triggers for Run 1

6.1.3 Preliminary Data Reduction

The initial offline selection utilized the complete set of Run 1 μdsts. After selection demanding the above triggers, the data were filtered by requiring at least one PELC/PPHO candidate with $E_T^{\rm em} \geq 10$ GeV, $\mid \eta_{\rm em} \mid \leq 3.3$ and at least one PMUO[1] candidate with $P_T^{\mu} \geq 7$ GeV/c, $\mid \eta_{\mu} \mid \leq 2.5$. In addition, the PELC/PPHO candidates were required to have $\chi^2 \leq 300$ and $\mathcal{I} \leq 0.3$. The resulting files were then processed through the top_dilep package [72] where CAFIX 5.0 was used to apply the final data calibrations [57]. The corrected data were then written to disk

[1]PMUO is the definition of muon in DØ

$\epsilon_{CC}^{\rm eid}$	$\epsilon_{EF}^{\rm eid}$
0.768 ± 0.018	0.599 ± 0.025

Table 6.2: Electron identification efficiencies for Run 1

in the form of column wise PAW ntuples files. During this stage any events from runs with known detector problems were removed using the standard Run 1 bad run list [73]. Subsequent analysis was done using compiled Fortran code, PAW and Mircosoft EXCEL.

6.2 Particle Selection and Detection Efficiencies

6.2.1 Electron Selection and Identification Efficiency

The electrons for this analysis were selected by using the following cuts (see Chapter 4.3 for definitions of the variables):

$E_T^e \geq 15$ GeV with $|\eta^e| \leq 2.5$

$\mathcal{I} \leq 0.1$

$L_5 \leq 0.5$

The corresponding electron identification efficiencies were determined from an independent data set using the procedure outlined below.

Since the electrons from $Z \rightarrow ee$ decays have similar kinematics to those in $t\bar{t}$ decays, these are chosen as representative for efficiency calculation. The procedure was based on a sample of data with two reconstructed electro-magnetic clusters with $E_T \geq 20$ GeV. One of the electron candidates, denoted as the 'tag', was required to satisfy tight identification cuts ($\chi^2 \leq 100$, $\mathcal{I} \leq 0.15$). If the second electro-magnetic cluster, denoted as the 'probe', satisfied $\mathcal{I} \leq 0.1$, then the invariant mass of the pair, $m(\text{tag}, \text{probe})$ was recorded. This was done separately for probes in the central (CC, $|\eta^e| \leq 1.1$) and end cap (EC, $|\eta^e| > 1.1$ and $|\eta^e| \leq 2.5$) regions of the calorimeters. The number of entries in the Z mass window 80 <m(tag, probe)< 100 GeV/c^2, were counted and corrected for the residual background.

The track finding efficiency, ϵ_{trk} which was determined from the above selected $Z \rightarrow ee$ data is defined by:

$$\epsilon_{trk} = \frac{\text{number of 'probes' with a matching track}}{\text{total number of 'probes'}} \tag{6.3}$$

The results vary with the number of reconstructed vertices per event. Typical values are 82.7 ± 1.1 % for the CC and 85.2 ± 1.0 in the EC.

The second component of the identification efficiency is the electron cluster

R^f_{CC}	R^f_{EC}
0.046 ± 0.001	0.08 ± 0.001

Table 6.3: Electron fake rate

identification efficiency (effect of $L_5 \leq 0.5$ cut). This is given by:

$$\epsilon_{clus} = \frac{\text{number of 'probes' with a matching track passing } L_5 \leq 0.5}{\text{total number of 'probes' with a matching track}} \tag{6.4}$$

This gives results of 88.0 ± 1.6 % in the CC and 63.8 ± 2.3 % in the EC regions. For $t\bar{t}$ Monte Carlo simulations there is an implicit tracking inefficiency built in. To avoid double counting when using the values of ϵ_{trk}, the results must be corrected (normalized) using the Monte Carlo efficiencies (ϵ^{MC}_{trk}). These are 94.8 ± 0.6 % for CC and 90.7 ± 1.6% in th EC [74].

The total electron identification efficiency is then given by:

$$\epsilon^{eid} = \epsilon_{clus} \times \frac{\epsilon_{trk}}{\epsilon^{MC}_{trk}} \tag{6.5}$$

which gives the results listed in Table 6.2.

6.2.2 Electron Misidentification or 'Fake Electron' Rate

To determine the fake electron rate, a sample of QCD multi jet events was used. A loose event selection was performed, requiring one electron to pass loose electron identification cuts ($\mathcal{I} \leq 0.3$ and $\chi^2 \leq 300$). The fake rate is then given by the fraction of these events which pass the tight electron selection criteria. The results were computed separately for the CC and the EC giving the values listed in Table 6.3.

6.2.3 Muon Selection and Detection Efficiency

The muon selection criteria are different for runs 1a, 1b and 1c because of the physical changes made to the WAMUS chambers and the trigger logic. Three sets of selection cuts are used, corresponding to the WAMUS configurations for run 1a (1992-93), the first half of run 1b (1994) and the second half of run 1b + 1c (1994-95, 1996). Run 1a is treated separately because of the changes made in the level 2 trigger logic to enable the use of the offline MTC package (see section 4.4). During the first part of the 1994 data taking, it was found that the efficiencies of some of the WAMUS chambers in the central (CF, quad $\leq 4 \approx\mid \eta^\mu \mid \leq 1.0$) spectrometer close to main ring beam pipe and the forward (EF, quad > 4 and quad $\leq 12 \approx\mid \eta^\mu \mid > 1.0$

	1a -	1b prezap	1b+1c postzap	
	CF	CF	CF	EF
$P_T^\mu \geq$	15	15	15	
IFW4 $\leq$	1	1	1	0
calmip	yes	no	no	
MTC	no	yes	yes	
$\Delta R(\mu, jet) \geq$	0.5	0.5	0.5	
$\Delta R(\mu, e/\gamma) \geq$	0.25	0.25	0.25	

Table 6.4: Muon selection criteria

Run	$\epsilon_{CF}^{\mu\text{id}}$	$\epsilon_{EF}^{\mu\text{id}}$
Run 1a	0.86 ± 0.073	-
Run 1b and Run 1c	0.89 ± 0.062	0.50 ± 0.059

Table 6.5: Muon identification efficiencies for Run 1a, 1b and 1c

and $\mid \eta^\mu \mid \leq 1.7$) spectrometers showed serious deterioration. During the break in 1994 data taking the affected chambers were removed and cleaned to restore their efficiencies. Because of the efficiency problem the data taken in the pre-cleaning period is restricted to the CF region and is referred to as the 'prezap' data. The post cleaning data uses both the CF and EF spectrometers and is referred to as the 'postzap' data . The cuts used for these three configurations are summarized in Table 6.4.

The total muon finding efficiency, $\epsilon^{\mu\text{id}}$ was determined from a combination of inclusive muon data and Monte Carlo simulations and cross checked using $Z \to \mu\mu$ data. The value of $\epsilon^{\mu\text{id}}$ is given by the product:

$$\epsilon^{\mu\text{id}} = \epsilon_{trk} \times \epsilon_\phi \times \epsilon_{PMO} \tag{6.6}$$

where

ϵ_{trk} is the track finding efficiency in the WAMUS chambers.

ϵ_ϕ is a ϕ-dependent correction which is used to correct the monte carlo CF tracking efficiency in the region of the main ring beam pipe.

ϵ_{PMO} is the efficiency for finding a muon using loose identification cuts. (ϵ_{trk}

$\epsilon^{\text{trig}}_{CCCF}$	$\epsilon^{\text{trig}}_{CCEF}$	$\epsilon^{\text{trig}}_{ECCF}$	$\epsilon^{\text{trig}}_{ECEF}$
0.95 ± 0.05	0.93 ± 0.05	0.90 ± 0.04	0.93 ± 0.05

Table 6.6: Trigger efficiencies for Run 1

and ϵ_ϕ are treated as corrections to this.
The values of ϵ_{PMO} and ϵ_ϕ were determined from inclusive samples of high P_T muons [76] and ϵ_{trk} was determined using the combination of cosmic ray data and monte carlo calculations [75, 76]. Table 6.5 summarizes the total muon identification efficiencies, which have been weighted according to luminosity fraction for the prezap and postzap parts of Run 1b. For a full discussion the reader is referred to [75, 76].

6.2.4 Trigger Efficiencies

The data were divided into four different classes according to the detector region into which the e and μ fell. These were chosen to enable an efficient simulation of the detector and trigger response which is strongly correlated to the location of the e and μ. The four classes are $CCCF, CCEF, ECCF$ and $ECEF$ where $CCCF$ means that the electron is in CC and μ in CF; $CCEF$ means that the electron is in CC and μ in EF; $ECCF$ means that the electron is in EC and μ in CF; $ECEF$ means that the electron is in EC and μ in EF.

Because the number of $t\bar{t} \to e\mu$ events in the data is expected to be very small, the only practical way to estimate the trigger efficiency is by using simulations. For this, DØ uses a package called TRIG-SIM, which comprises of two separate packages: L1SIM and L2SIM. These simulate the Level 1 and Level 2 trigger logic and use the configuration files which were used during the actual data taking [70]. Because many such files were used over the 4 year of data taking period, we have chosen to the file which was used for the large number of runs as the reference set and used this to calculate the trigger efficiency. The results are shown in Table 6.6 where the error represents the combinations of the statistical uncertainty and the systematic errors due to variations between the configuration files.

6.2.5 Combined Trigger and Particle Identification Efficiencies

The trigger and particle identification efficiencies are combined to give four trigger $\times$ id efficiencies corresponding to the four e and μ classes. These are given

Run	ϵ_{CCCF}	ϵ_{CCEF}	ϵ_{ECCF}	ϵ_{ECEF}
Run 1a	0.63 ± 0.08	-	0.47 ± 0.06	-
Run 1b and 1c	0.65 ± 0.06	0.36 ± 0.05	0.48 ± 0.05	0.28 ± 0.04

Table 6.7: Trigger $\times$ identification efficiencies as a function of detector region and running period.

by:

$$\epsilon_{CCCF} = \epsilon^{\rm trig}_{CCCF} \times \epsilon^{e{\rm id}}_{CC} \times \epsilon^{\mu{\rm id}}_{CF} \tag{6.7}$$
$$\epsilon_{CCEF} = \epsilon^{\rm trig}_{CCEF} \times \epsilon^{e{\rm id}}_{CC} \times \epsilon^{\mu{\rm id}}_{EF} \tag{6.8}$$
$$\epsilon_{ECCF} = \epsilon^{\rm trig}_{ECCF} \times \epsilon^{e{\rm id}}_{EC} \times \epsilon^{\mu{\rm id}}_{CF} \tag{6.9}$$
$$\epsilon_{ECEF} = \epsilon^{\rm trig}_{ECEF} \times \epsilon^{e{\rm id}}_{EC} \times \epsilon^{\mu{\rm id}}_{EF} \tag{6.10}$$

and the resulting values are listed in Table 6.7.

6.3 Monte Carlo Simulations

In any High Energy Physics analysis, the most important thing is the ability to distinguish between signal and the backgrounds. The only way to study the details of the acceptances is by model each processes using Monte Carlo simulation. Although the instrumental backgrounds to the $t\bar{t} \to e\mu$ channel can be estimated from data, both the signal and the physics backgrounds have to be determined using Monte Carlo simulations. The reason is two fold. Firstly, suitable independent data sets are not available and secondly the acceptances are related to the details of the production and decay process which cannot be studied by other method.

Monte Carlo calculations consist of two steps: modeling the physics process and simulating the detector response. These are discussed in more detail below.

6.3.1 Event Generation

The most commonly used event generators for $p\bar{p}$ collision simulations are ISAJET [77], PYTHIA [78] and HERWIG [79]. Each of these perform the following processes;

- parton-parton hard scattering
- QCD evolution

- Hadronization

In an elementary hard scattering process, two (or more) partons interact to give rise to final state partons. This is typically calculated using leading order or tree level Feynman diagrams. Based on the distributions expected from the matrix element calculations, the momenta, spin and color connections of the final state partons are assigned.

Following the hard scattering, the partons are evolved through repeated parton branching using the Gribov-Lipatov-Altarelli-Parisi splitting functions [80]. The separation between emitted gluon and the parent is decreased after each branching and the evolution is continued until the partons are evolved. This procedure is used to simulate both the initial and final state radiation.

Fragmentation or Hadronization is the process by which partons evolve to produce hadrons. Since this cannot be calculated using perturbative QCD, an alternate technique must be used. The two most commonly used fragmentation models are; independent (Feynman-Field) fragmentation [81] and string fragmentation [82]. Most of the older generators use a former scheme which has been shown experimentally to be incorrect. Modern generators such as PYTHIA and HERWIG use either the Lund or similar string models [82]. Once generated, any unstable hadrons are allowed to decay into the final state particles according to their measured branching ratios.

6.3.2 Detector Simulation

The last step in simulating a physics process is the simulation of the detector response. The DØ detector uses a customized version of the CERN GEANT [83] program called DØGEANT. This encodes the DØ detector geometry and the materials through which the particles pass. It simulates in great detail the ionization in central tracking, the electro-magnetic and hadronic showers in the calorimeter and the hits in the muon chambers.

The CPU time needed to do the full simulation of the detector is enormous and is prohibitive when trying to obtain the very large event statistics necessary for this analysis. To get around this, a package known as the "shower library" is used to simulate the calorimeter response [84]. This is a library of GEANT shower information binned in 5 quantities which represents the kinematic of the input particle.

Following the DØGEANT simulation there are some additional corrections which need to be made. The first of these is to the efficiency and resolution of the WAMUS chambers which are only approximated in DØGEANT. This includes corrections for effects such as misalignments and the localized inefficiencies in the muon drift tubes due to gas leaks or voltage problems. This is done using a package called MU-SMEAR [85] which smears the hit timing information to match the resolution of collider data.

Another correction is for the effects of multiple $p\bar{p}$ interactions and calorimeter noise. This is done using a package called NOISY which allows the overlay multiple minimum bias events on the top of the hard scatter events being studied. This requires full DØGEANT simulation and is very CPU intensive. Thus only moderate samples of events are processed through NOISY. A correction to the acceptance is then made by making a comparison between single-interaction Monte Carlo events and those processed through NOISY.

The DØGEANT output is in the same form as actual data and consists of the digitized signals from various parts of the detector. These can then be processed through DØRECO to simulate the reconstruction smearing of the events.

6.4 $t\bar{t} \to e\mu$ Modeling

The simulation of the $t\bar{t} \to e\mu$X channel for this analysis was done using HERWIG version 5.7 with CTEQ3M parton distribution functions [32, 79]. Approximately 100,000 $t\bar{t} \to ll$ (where $l \to e, \mu$ or τ) events were generated for eight different values of the top quark mass (150, 155, 160, 165, 170, 175, 180, and 185 GeV/c^2). As a cross check, data sets were also generated using the ISAJET and the results compared. The events were processed through both DØGEANT and DØRECO and the signal acceptance estimated using only the events which yield a $e\mu$ final state. The values of the $t\bar{t}$ production cross section values were taken from Laenen *et. al* [26].

6.5 Background Modeling

The backgrounds to the eμ channel were modeled using the ISAJET and PYTHIA generators. For $Z \to \tau\tau \to ll$, ISAJET was used and the cross section was normalized to the DØ measured value [86]. The $WW \to ll$ and $\gamma^* \to \tau\tau \to ll$ backgrounds were both modeled using PYTHIA. The WW cross section was normalized to the predicted NLO QCD value [36] and the cross section of the γ^* process was normalized to the measured cross section [87]. Note that the feed down effects of secondary $\tau \to \mu/e$ decays have been included in both the background and signal modeling.

Chapter 7

Event Selection and Data Analysis

Get ready! Good fortune comes in bunches.

- Fortune Cookie

This chapter describes the training and implementation of the neural network architecture in the event selection procedure.

7.1 Neural Network Architecture

There are two stages in neural network analyses. The first is the training of the networks and second is testing. Neural networks are trained on samples of signal and background events and tested using independent data sets. The procedures of training and testing are described in detail below.

7.1.1 Network Training

In deciding how to use the neural network techniques for the $e\mu$ analysis, the first step was to decide how many networks to use. After exploring various possibilities it was established that the optimal discrimination between the signal and the background could be achieved using three separate networks. Each of these discriminate between the signal and one of the dominant backgrounds (see section 2.7.2).

- Network 1 (NN1), – $t\bar{t}$ vs instrumental background ($b\bar{b}/c\bar{c}$, W + jets) events
- Network 2 (NN2), – $t\bar{t}$ vs $WW \to e\mu$ events
- Network 3 (NN3), – $t\bar{t}$ vs $Z \to \tau\tau \to e\mu$ events

Large samples of data (instrumental background) and Monte Carlo ($t\bar{t}$, WW and Z) events were prepared using minimal selection criteria [1] so as not to bias the results. From these a small sub-sample of 1000-2000 events were selected at random to provide the training sample.

The number of nodes and the input parameters for each network were selected to give the best discrimination between the signal and background. Several nodal configurations were tested but the best results were obtained using three identical networks, each of which has six input nodes, seven hidden nodes and one output node. The input parameters used for each of the three network is listed below:

- Variables used in NN1 and NN2
  - E_T^e, Transverse energy of the leading electron
  - E_T^{jet2}, Transverse energy of next to leading jet
  - $\not\!\!E_T^{cal}$, Missing transverse energy
  - H_T^{Jets}, Scaler sum of jet transverse energies
    $H_T^{Jets} = \sum_{alljets} E_T^{jet}$ with$|\eta^{jet}| \leq 2.5$ and $E_T^{jet} \geq 15$GeV
  - $M_{e\mu}$, Electron muon invariant mass
  - $\Delta\phi_{e\mu}$, Azimuthal separation of the leading electron and muon
- Variables used in NN3
  - same as NN1 except E_T^{jet2} replaces E_T^{jet1} (transverse energy of the leading jet)

Figure 7.1, 7.3 and 7.5 shows comparisons of these variables for $t\bar{t} \to e\mu$ and the instrumental backgrounds, WW and $Z \to \tau\tau$ backgrounds respectively.

Each of the three networks was trained for 2000 training cycles. Training started with a set of random weights and thresholds which were adjusted using back propagation during training. The final results are shown in Figures 7.2, 7.4 and 7.6 which show the nodal connectivity for NN1, NN2, and NN3 respectively. The thickness of the lines represents the connecting strength.

7.1.2 Testing

After each network has been trained, a test procedure is implemented in which the events not used in training were passed through the network. An output is provided for each event which can be considered as the probability of that event

[1] $E_T^e \geq 10$ GeV, $P_T^\mu \geq 10$ GeV and $N_{\rm jets} \geq 1$ with $E_T^{\rm jet} \geq 10$ GeV

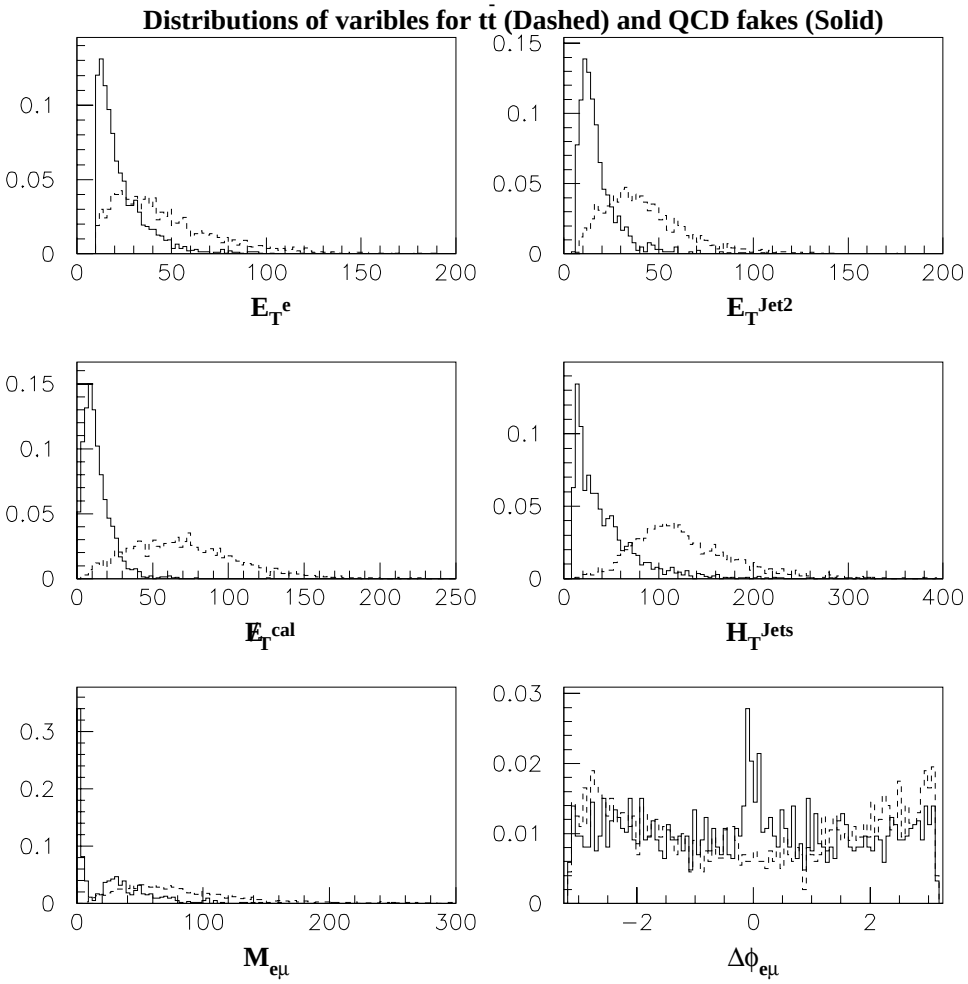

Figure 7.1: Distributions of the variables used in NN1

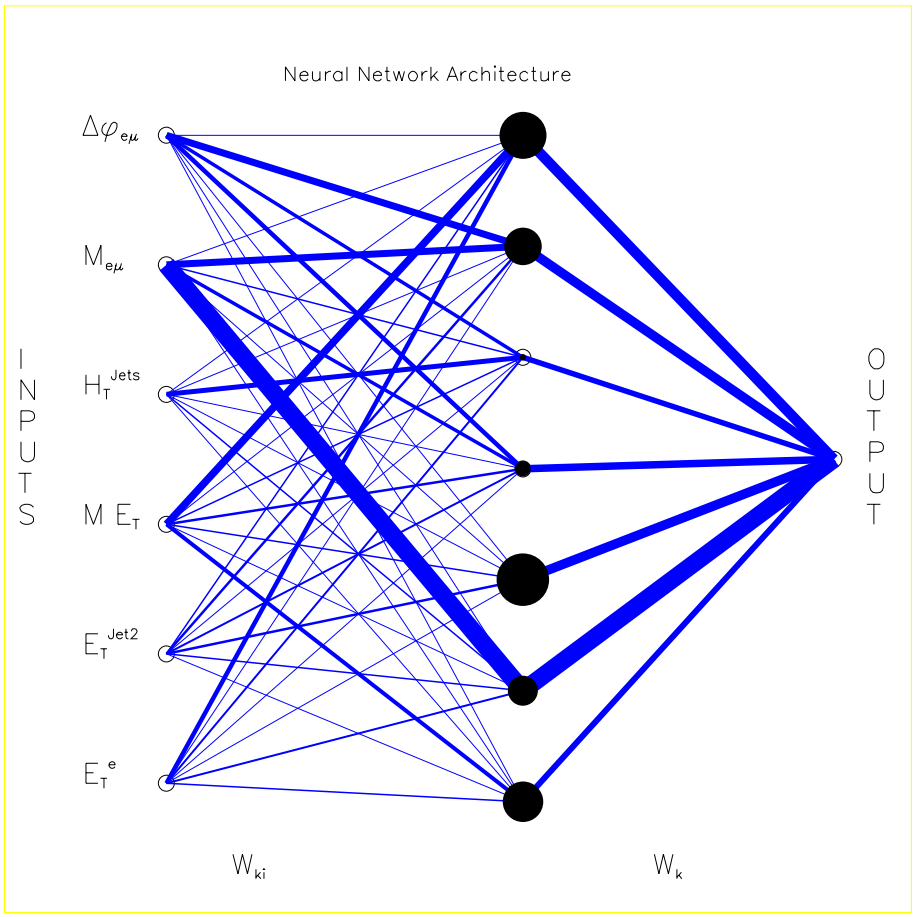

Figure 7.2: The architecture of NN1 after training on instrumental background and $t\bar{t}$ events. The thickness of lines and size of the nodes represent the connecting strengths between different nodes and thresholds respectively.

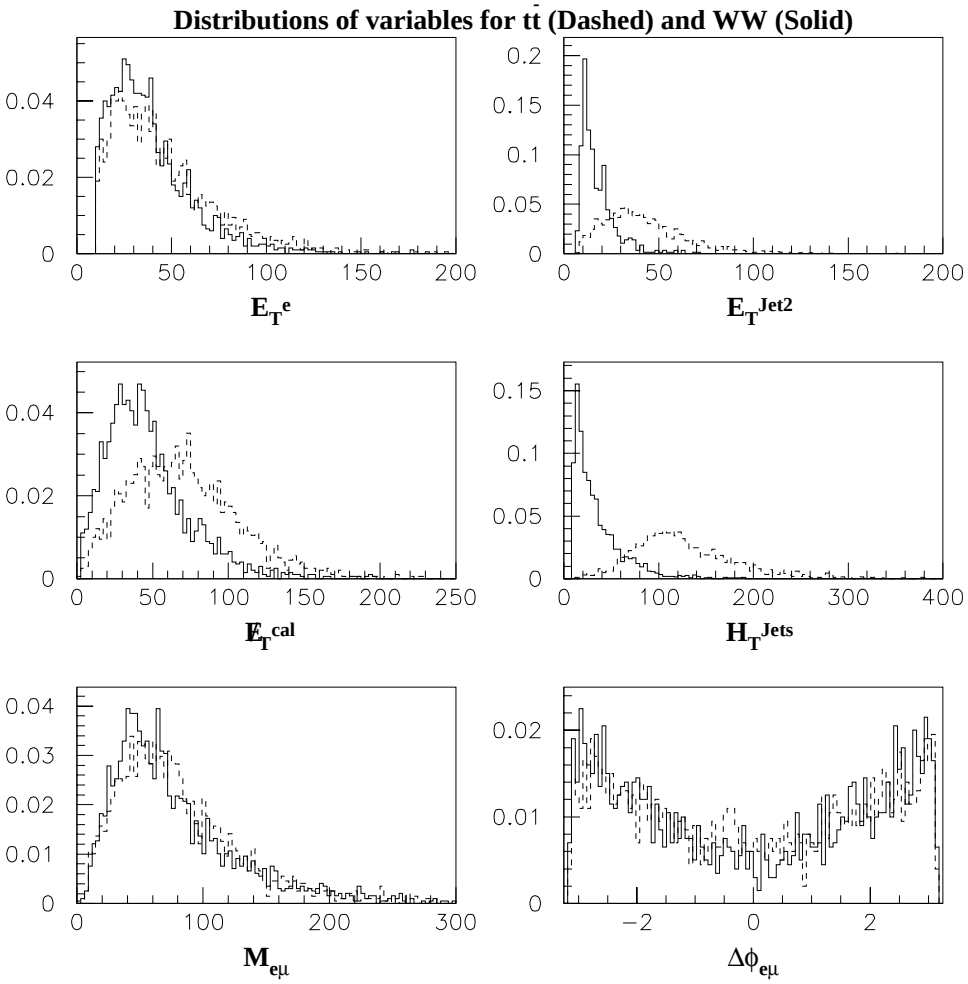

Figure 7.3: Distributions of the variables used in NN2

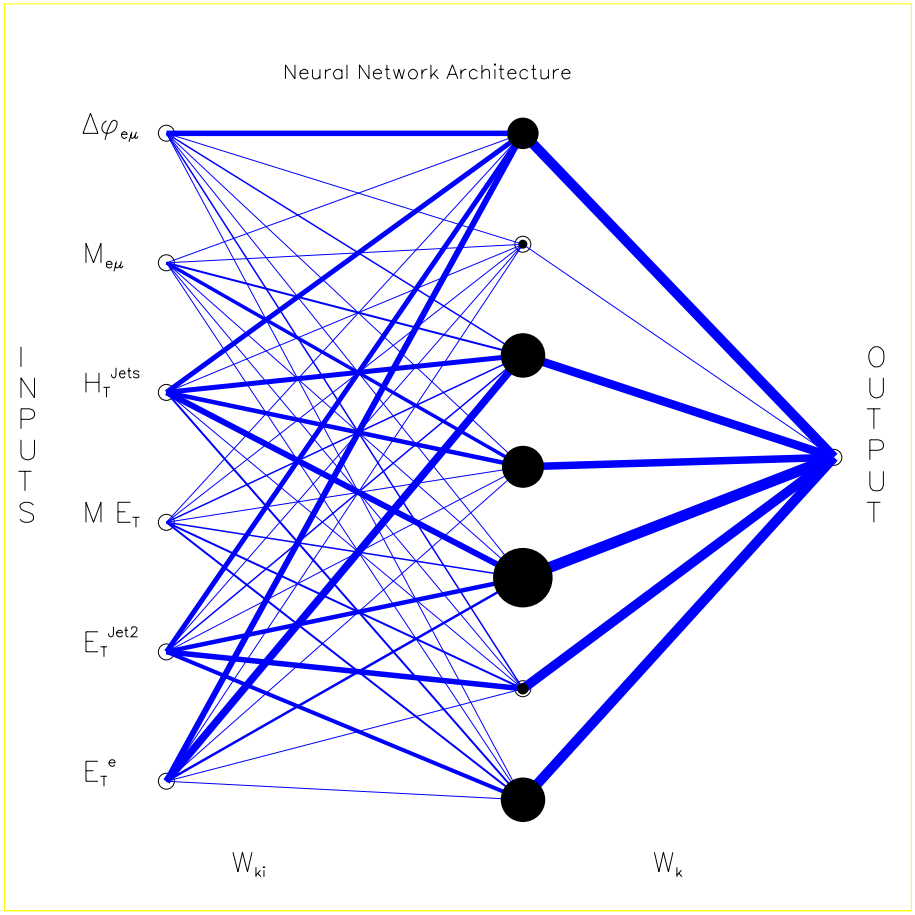

Figure 7.4: The architecture of NN2 after training on WW and $t\bar{t}$ events. The thickness of lines and size of the nodes represent the connecting strengths between different nodes and thresholds respectively

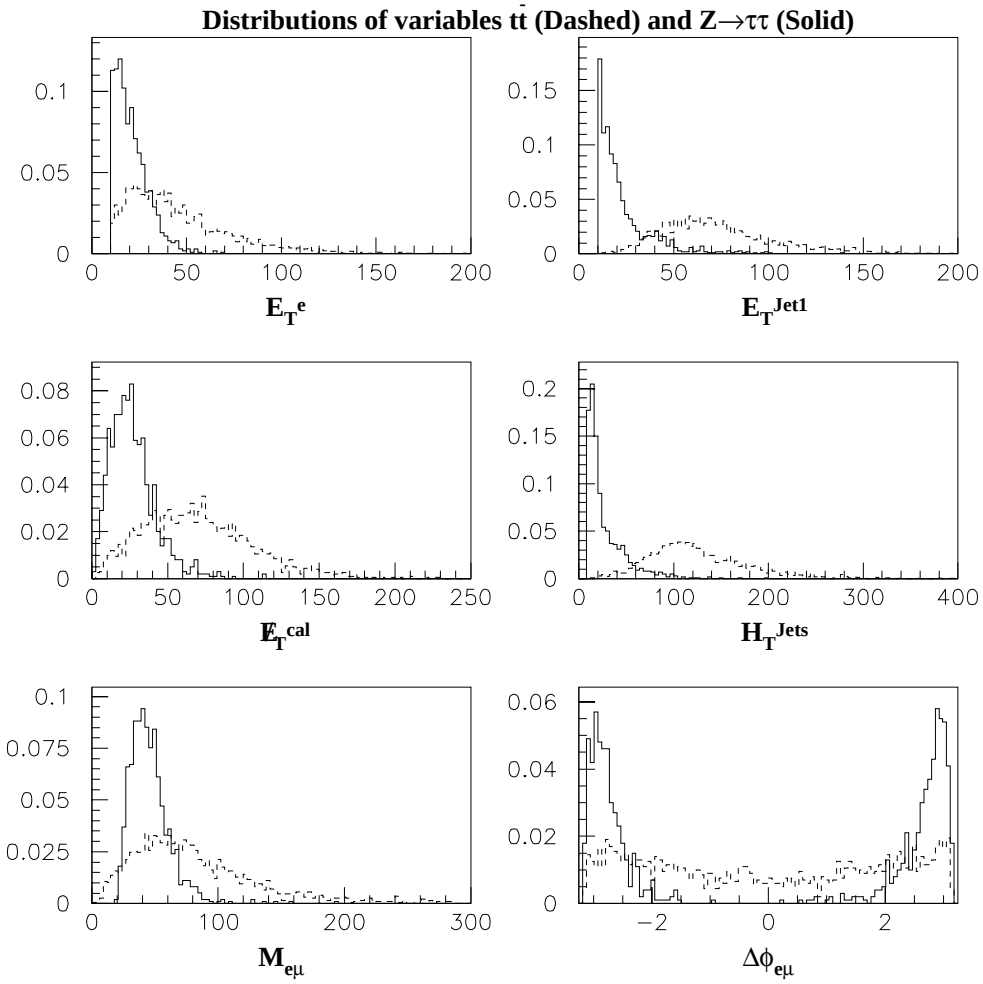

Figure 7.5: Distributions of the variables used in NN3

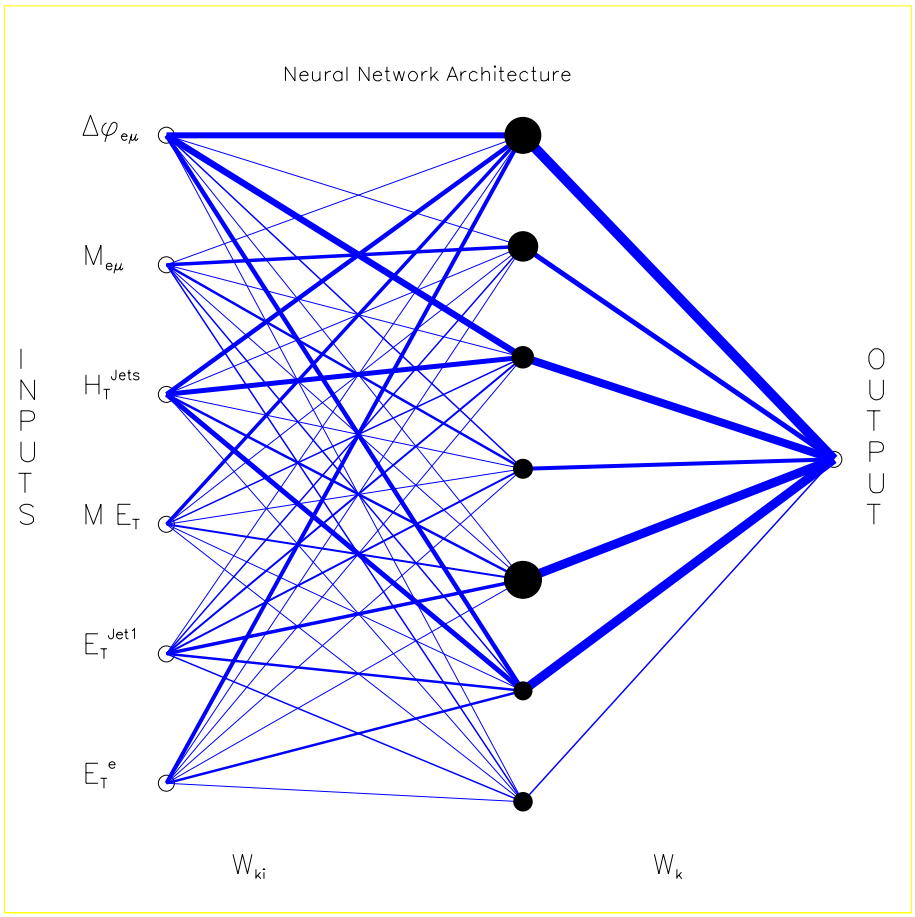

Figure 7.6: The architecture of NN3 after training on Z$\rightarrow \tau\tau$ and $t\bar{t}$ events. The thickness of lines and size of the nodes represent the connecting strengths between different nodes and thresholds respectively

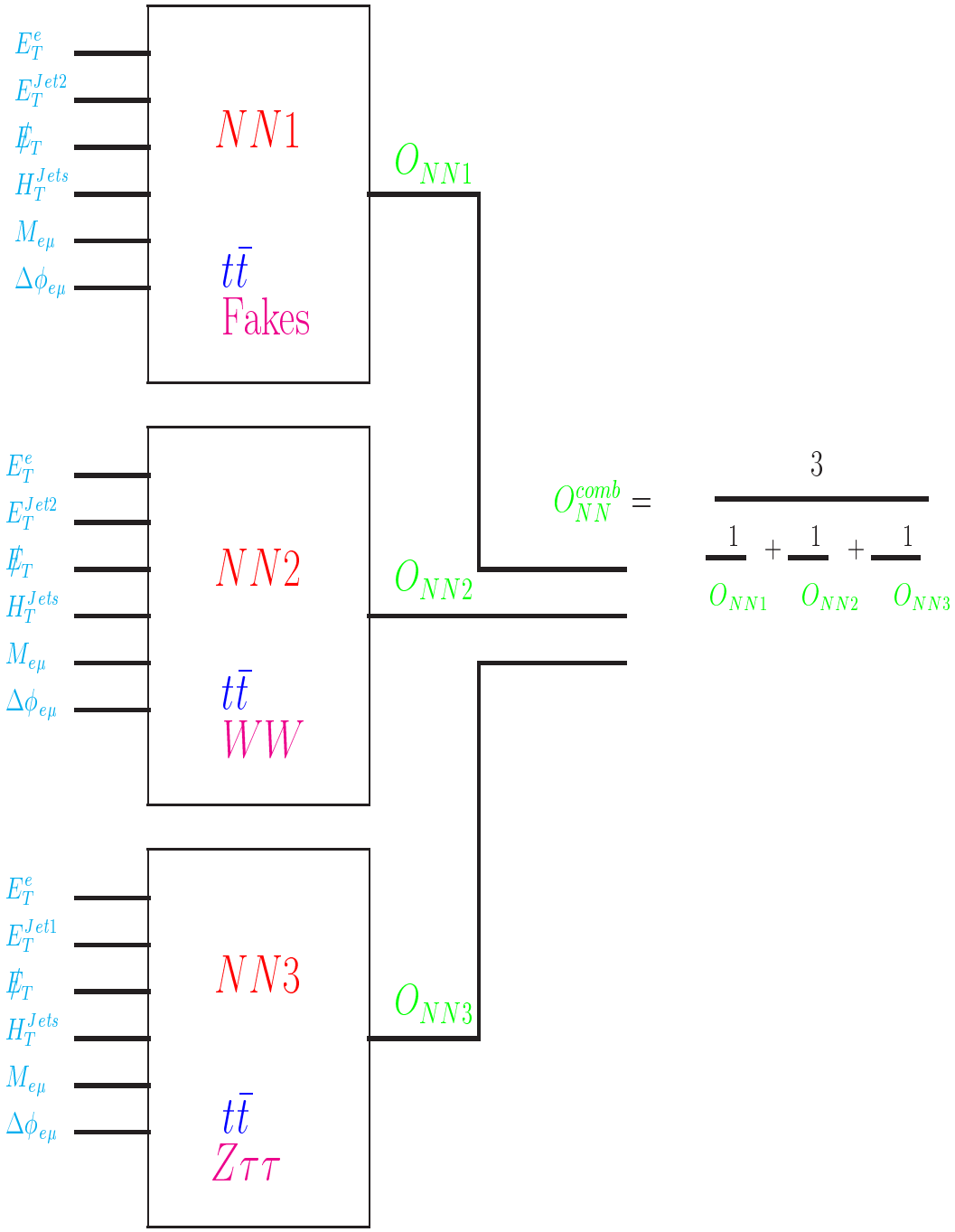

Figure 7.7: Schematic of the combined architecture

being either signal or background. If the training has been done correctly, the probability for an event being signal is high if the output is close to 1. Conversely if the output is close to 0 then it is more likely to be a background event (see Figure 7.9).

In our case there are three independent networks whose outputs are O_{NN1}, O_{NN2} and O_{NN3} respectively. By forming a simple algebraic sum (see Figure 7.7) these can be combined to give an overall discriminant, $O_{NN}^{\rm comb}$ which gives the probability that a given event is either a signal or background. This can be written as:

$$O_{NN}^{\rm comb} = \frac{3}{\frac{1}{O_{NN1}} + \frac{1}{O_{NN2}} + \frac{1}{O_{NN3}}} \tag{7.1}$$

It can be shown (see Appendix D) that such a combination is equivalent to that of a output of a single neural network, which was trained on each of the three different backgrounds and the signal. The rationale for choosing the single discriminant is one of the simplicity in that it provides a single variable which can be used for event selection.

Figure 7.8 shows a comparison of the signal and background selection efficiencies for grid searches done using independent network cuts and a single cut on the combined discriminant. Each open point represents a set of cuts on $O_{NN1}, O_{NN2}, O_{NN3}$ and the solid points, a cut on $O_{NN}^{\rm comb}$. This clearly shows that the $O_{NN}^{\rm comb}$ cut retains all of the discriminant power of the separate network cuts and provides an excellent choice for maximizing the signal to background ratio. In principal one could also weight each network output according to the cross sections of processes involved. However we have found that the results are insensitive to this and so we have kept this simple approach.

Figures 7.9 and 7.10 show comparison of the discriminant distributions for signal and background test samples. In Figure 7.9 the backgrounds have been combined and in Figure 7.10 they are shown separately.

Another important factor is the sensitivity of the network training to the value of top quark mass used in the training and test samples. For training we chose $m_t = 170$ GeV which is close to the DØ measured value. To test the sensitivity we used the network trained on 170 GeV events on several top quark samples generated with different mass. The results, shown in Figures 7.11 and 7.12, indicate that the discrimination is relatively insensitive to the value of m_t within this large range.

7.2 Event Selection and Data Analysis

The analysis cuts used for Run 1 analysis are summarized below:

- Trigger requirements (see Chapter 6.1.2)

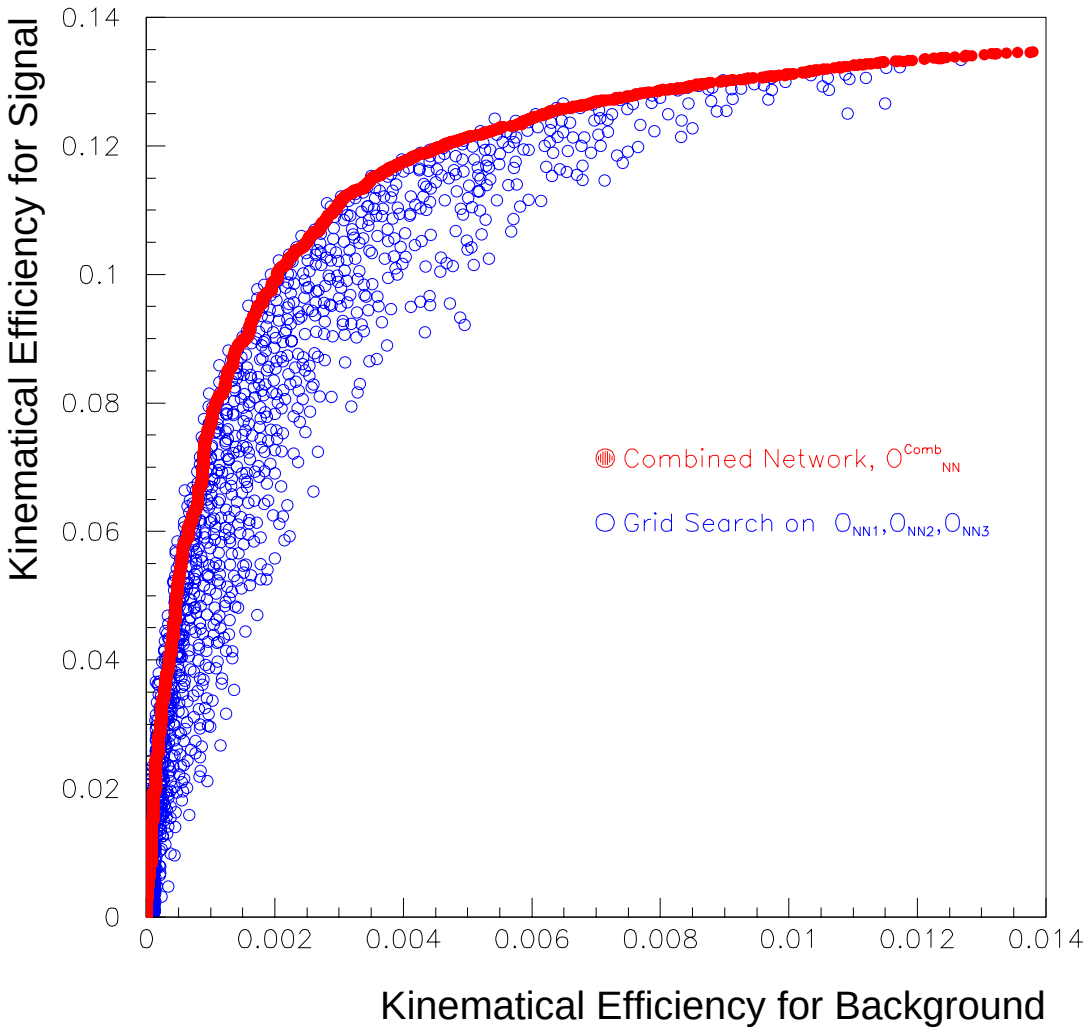

Figure 7.8: A plot of signal efficiency and background efficiency for a grid search on the $O_{NN1}, O_{NN2}, O_{NN3}$ and their combination O_{NN}^{comb}. Each circle is a set of cuts on $O_{NN1}, O_{NN2}, O_{NN3}$

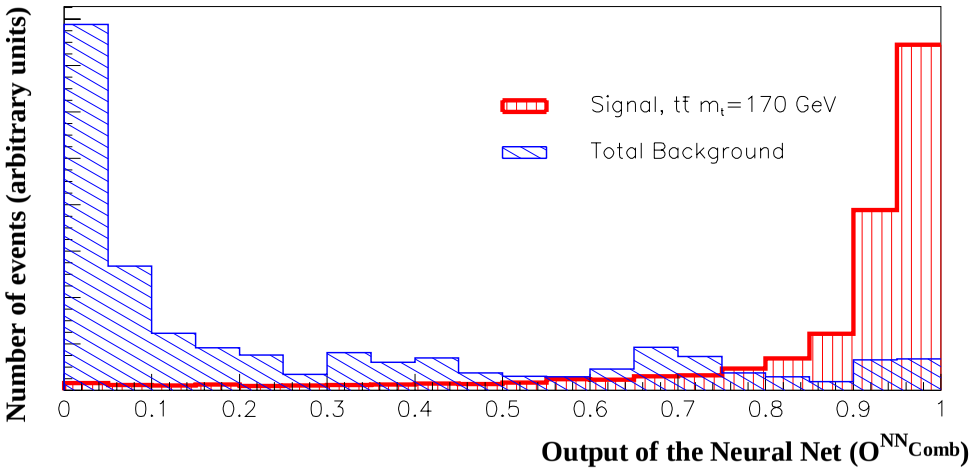

Figure 7.9: The distribution of total background and signal as a function of $O_{NN}^{\rm comb}$.

- $N_{\rm electron} \geq 1$ passing identification cuts (see Chapter 6.2.1) with $\mathrm{E}_T^e \geq 15$ GeV and $\mid \eta^{\rm e} \mid \leq 2.5$
- $N_{\rm muon} \geq 1$ passing identification cuts (see Chapter 6.2.3) with $\mathrm{P}_T^\mu \geq 15$ GeV and quad ≤ 12
- $\Delta R_{\mu,\rm jets} \geq 0.5$ and $\Delta R_{\mu,ele} \geq 0.25$
- $\not\!\!E_T^{cal} \geq 15$ GeV
- $N_{\rm jets} \geq 2$ with $E_T^{\rm jet} \geq 15$ GeV and $\mid \eta^{\rm jet} \mid \leq 2.5$
- $O_{NN}^{\rm comb} \geq 0.88$

Most of the kinematical cuts used in this analysis are close to the trigger thresholds. The $O_{NN}^{\rm comb}$ cut is chosen to correspond to the maximum of the distribution of relative significance ($\frac{S}{\sigma_B}$) versus network output (see Figure 7.13), where σ_B is the measured uncertainty on the expected number of background events.

Table 7.1 shows the number of events which survive each level of cuts in the data. Although not explicitly stated, all of the events have passed the $e\mu$ trigger requirements. Also shown are the corresponding background yields and the predicted $t\bar{t}$ event yields for $m_t = 170$ GeV.

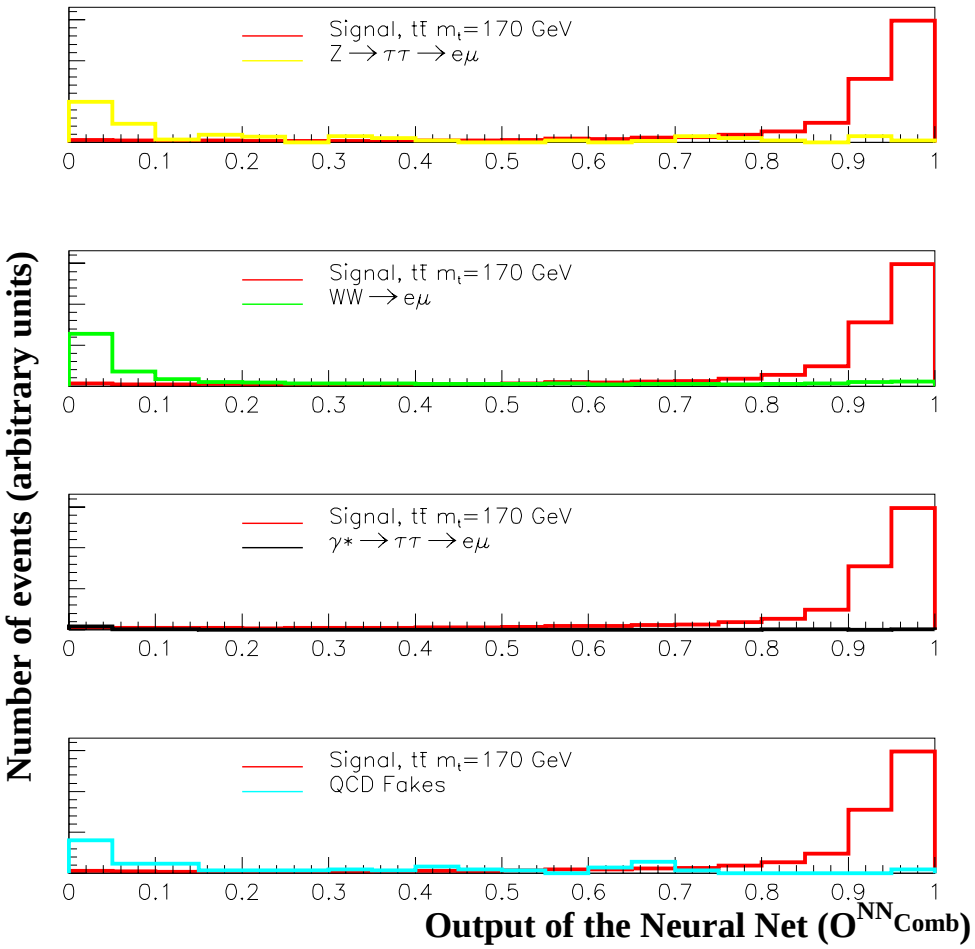

Figure 7.10: The distribution of different backgrounds and signal as a function of O_{NN}^{comb}, Z $\to \tau\tau \to e\mu$, $WW \to e\mu$, $\gamma^* \to \tau\tau \to e\mu$ and QCD fakes

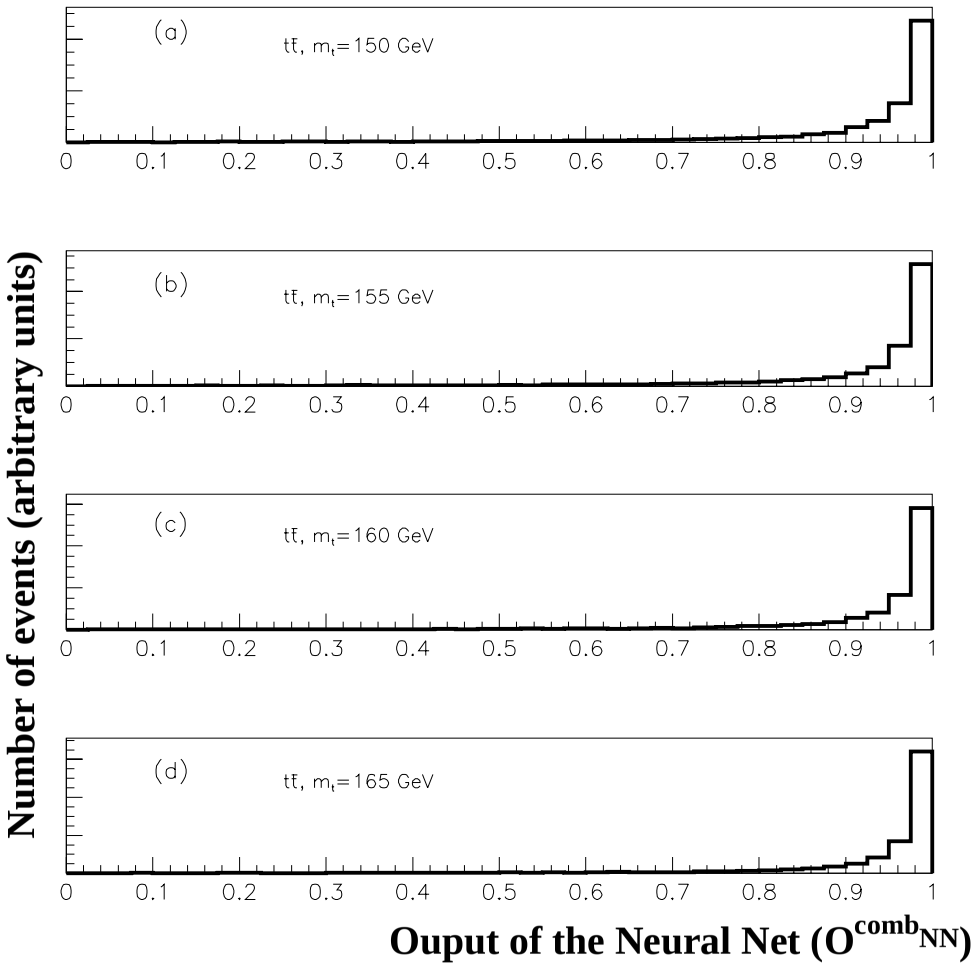

Figure 7.11: The distribution of signal as a function of $O_{NN}^{\rm comb}$ for (a) $m_t = 150$ GeV (b) $m_t = 155$ GeV (c) $m_t = 160$ GeV (d) $m_t = 165$ GeV

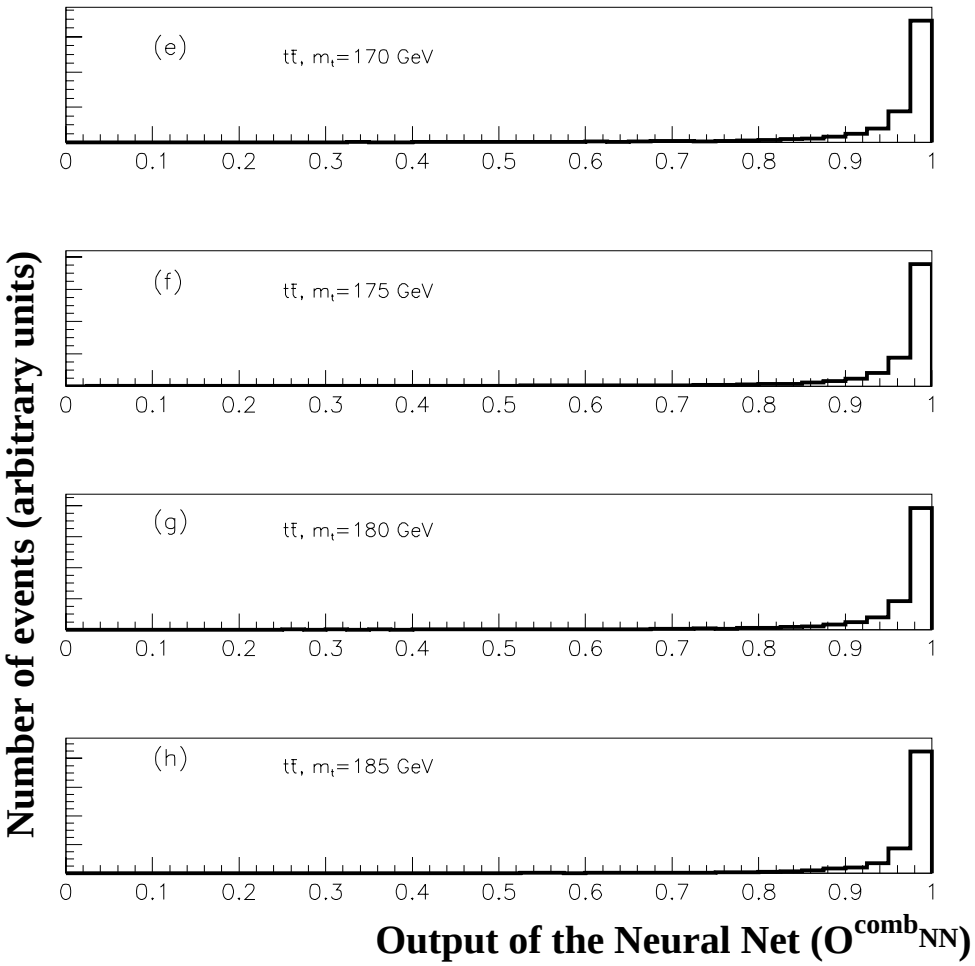

Figure 7.12: The distribution of signal as a function of $O_{NN}^{\rm comb}$ for (e) $m_t = 170$ GeV (f) $m_t = 175$ GeV (g) $m_t = 180$ GeV (h) $m_t = 185$ GeV

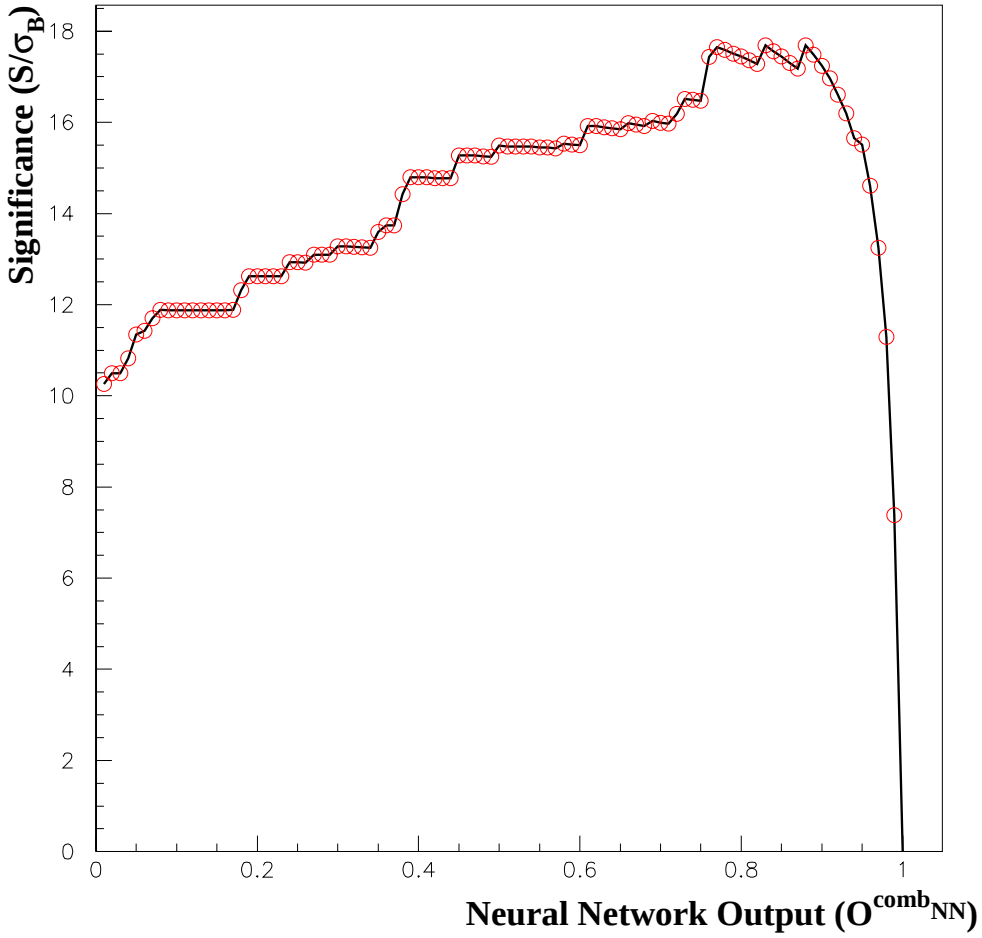

Figure 7.13: The relative significance ($\frac{S}{\sigma_B}$) versus neural network output ($O^{\rm comb}_{NN}$), where σ_B is the uncertainty on the estimated background.

Cut	$t\bar{t}$ $\varepsilon \times \mathcal{BR}$ (%)	Signal $m_t = 170$ GeV/c^2	Background		Signal + Background	Data
			Fakes	Physics		
$E_T^e \geq 15$ GeV, $P_T^\mu \geq 15$ GeV	0.68 ± 0.15	4.3 ± 0.9	54 ± 2	40 ± 9	98 ± 12	130
$\Delta R_{\mu,\text{jets}} \geq 0.5$, $\Delta R_{\mu,ele} \geq 0.25$	0.53 ± 0.11	3.4 ± 0.7	12 ± 1	39 ± 8	54 ± 9	58
$\not\!\!E_T^{cal} \geq 15$ GeV	0.52 ± 0.11	3.3 ± 0.7	5.8 ± 0.5	32 ± 7	42 ± 8	44
$N_{\text{jets}} \geq 2$, $E_T^{\text{jets}} \geq 15$ GeV	0.45 ± 0.10	2.8 ± 0.7	0.68 ± 0.17	0.85 ± 0.21	4.4 ± 0.9	6
$O_{NN}^{\text{comb}} \geq 0.88$	0.35 ± 0.06	2.2 ± 0.5	0.04 ± 0.12	0.18 ± 0.07	2.5 ± 0.7	4

Table 7.1: The expected and observed number of events as a function of cuts

There is a good agreement between the data and background plus $t\bar{t}$ event calculations for each of the cuts shown, despite the fact that the backgrounds vary by nearly two orders in magnitude from the first set to the last. The composition of the background also changes considerably. With the initial e and μ selection, the background is dominated by QCD multijet events containing a fake electron and non-isolated muon from a semi-leptonic b or c quark decay. This is the most difficult background to calculate reliably as the events come from a very restricted phase space of a large cross section process. The $\Delta R_{\mu,\text{jets}}$ cut is very effective in removing these events

The other component of the second level of cuts is $\Delta R_{\mu,ele}$ cut which is used to remove radiative $W \to \mu\nu$ + jets events in which the muon radiates a photon as it passes through the calorimeter. As this is a bremsstrahlung process in which the photon remains close to its parent muon, the photon can often be misidentified as an electron by matching to the CD track of the muon. The handful of the events which appear in the data are easily removed by the $\Delta R_{\mu,ele}$ cut.

The residual fake ($b\bar{b}/c\bar{c}$ and $W \to \mu\nu$ + jets) background is further reduced by the $\not\!\!E_T^{cal} \geq 15$ GeV cut. In the case of the $b\bar{b}/c\bar{c}$ events the $\not\!\!E_T^{cal}$ is the result of the jet mis-measurement and/or electron misidentification and is typically small. In the case of $W \to \mu\nu$ + jets events, this is effectively a cut on the transverse momentum of the W boson because both the μ and ν are not seen in the calorimeter. Requiring $P_T^W \geq 15$ GeV removes any low P_T events. The effect of this on the $t\bar{t}$ events is negligible.

After the $\not\!\!E_T^{cal}$ cut, the background is dominated by $Z \to \tau\tau \to e\mu$X and

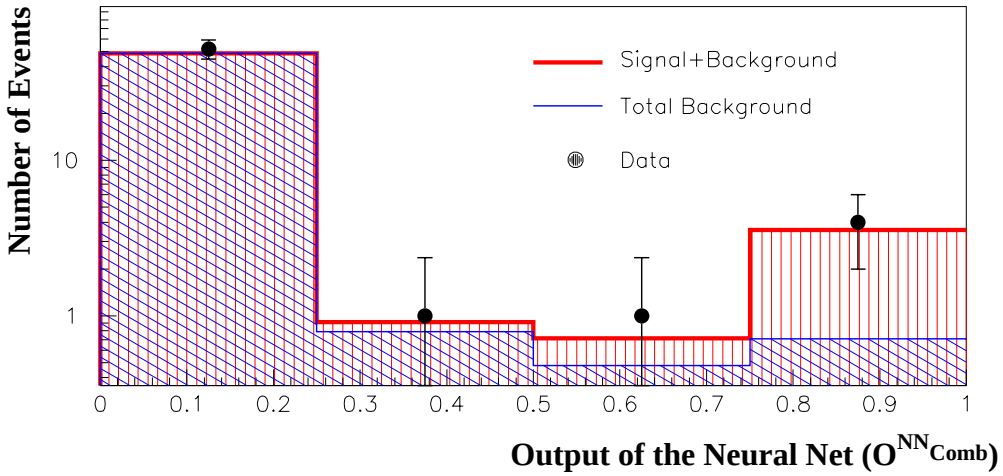

Figure 7.14: Distributions of the signal, background and data as a function of neural network output.

$WW \to e\mu$X events. The jets in these events are produced by initial state radiation (bremsstrahlung) and the rate is suppressed by a factor of $O(\alpha_s)$ for each jet. This results in both fewer jets and softer transverse energy spectrum than in $t\bar{t}$ events. In the $t\bar{t}$ case we have at least two jets from the $b(\bar{b})$ decays which are quite energetic. By requiring at least two central ($|\eta^{\rm jet}| \leq 2.5$) jets with $E_T^{\rm jet} \geq 15$ GeV we obtain a significant suppression of these backgrounds.

Lastly, the $O_{NN}^{\rm comb} \geq 0.88$ cut performs the final signal to background optimization. Figure 7.14 shows a comparison of the data and the expected signal and background rates as a function of $O_{NN}^{\rm comb}$. The final event sample contains 4 events with an estimated background of 0.22 ± 0.14 event.

Here we have given an overview of the features of the data and background calculations. The acceptance and event yield calculations are discussed in more details in the following sections.

7.3 Acceptance and Event Yield Calculations

The total acceptance for a given process, $\mathcal{E}$ ($\varepsilon\times$ BR) is given by:

$$\mathcal{E} = \varepsilon \times BR = BR \times \frac{N_{\rm cut}^{\rm tot}}{N_{\rm input}} \tag{7.2}$$

where $N_{\rm cut}^{\rm tot}$ is the number of events surviving after the cuts have been applied. This is given by:

$$\begin{aligned} N_{\rm cut}^{\rm tot} &= N_{CCCF} \times \varepsilon_{CCCF} + N_{CCEF} \times \varepsilon_{CCEF} \\ &+ N_{ECCF} \times \varepsilon_{ECCF} + N_{ECEF} \times \varepsilon_{ECEF} \end{aligned} \tag{7.3}$$

where $N_{CCCF}, N_{CCEF}, N_{ECCF}, N_{ECEF}$ are the number of events remaining in $CCCF$, $CCEF$, $ECCF$ and $ECEF$ classes respectively (see chapter 6.2.4). The terms $\varepsilon_{CCCF}, \varepsilon_{CCEF}, \varepsilon_{ECCF}, \varepsilon_{ECEF}$ are the corresponding selection efficiencies and $N_{\rm input}$ is the starting number of events. BR is the branching fraction of $t\bar{t} \rightarrow$ dileptons (e,μ only). This is discussed in detail in Appendix B. After correcting for the τ decay modes it takes the value of 0.0685.

The expected number of events for a given process is then given by:

$$N^{\rm expected} = \sigma_{\rm input} \times \mathcal{E} \times \int \mathcal{L} dt \tag{7.4}$$

where $\sigma_{\rm input}$ is the input cross section (measured or theoretical) and $\int \mathcal{L}$ dt is the total integrated luminosity.

To calculate the background event yields presented in Table 7.1 two sets of calculations were performed. The first set, to determine the fake background ($b\bar{b}/c\bar{c}$ and $W \rightarrow \mu\nu$ + jets), used a set of appropriately normalized collider data. The second, the physics backgrounds ($Z \rightarrow \tau\tau \rightarrow e\mu, \gamma^* \rightarrow \tau\tau \rightarrow e\mu$ and $WW \rightarrow e\mu$), used Monte Carlo event samples with cross sections taken from either experimental measurements (Z/γ^*) or NLO QCD calculations (WW) (see chapter 2.7.2). The $t\bar{t} \rightarrow e\mu$X yields were also calculated using Monte Carlo event samples for which the cross section was normalized to the resumed NLO QCD result of Laenen *et. al* [26]

The data used in this analysis were taken with a wide range of instantaneous luminosities. At the higher luminosities it is common to have two or three interactions within the detector lifetime which has the effect of introducing a luminosity dependence into some of the acceptance corrections. This is automatically built into the fake calculations which were done using collider data, but for Monte Carlo calculations an additional correction must be determined. The Monte Carlo data sets were generated using only a single hard scattering per event. The method used to correct for the effects of multiple interactions is described below.

Three different sets of $t\bar{t} \rightarrow e\mu$X monte carlo events corresponding to one, two and three interactions were generated using the NOISY package. These have :

- one hard scattering (one interaction)
- one hard scattering plus one minimum bias event (two interactions)
- one hard scattering plus two minimum bias events (three interactions)

Number of interactions	Acceptance
1	0.35 ± 0.02
2	0.31 ± 0.02
3	0.27 ± 0.02

Table 7.2: Acceptance after all the cuts for different number number of interactions. error are statistical only.

The events were processed through the full DØGEANT and DØRECO and used to calculate results for the selection efficiency as a function of the number of interactions. The results are listed in Table 7.2 and shown in Figure 7.15(a), from which it is clear that the acceptance decreases as the number of interactions increase.

To determine a correction factor, the acceptance variation was parameterized using a straight line fit as a function of the number of interactions, N:

$$A(N) = 0.39 - 0.04 \times N \tag{7.5}$$

Figure 7.15(b) shows the distribution of the number of interactions throughout Run 1. For the average value of 1.83, the correction factor (C) is given by:

$$C = \frac{A(N=1) - A(N=1.83)}{A(N=1)} \tag{7.6}$$

and the total acceptance after correction is:

$$\mathcal{E}^{corr} = \mathcal{E} - \mathcal{E} \times C \tag{7.7}$$

This gives an acceptance correction of 9% for the $t\bar{t}$ process. Because of the kinematical and topological similarities between the $t\bar{t}$ and background process after the cuts, we apply the same correction factor to the Z/γ^* and WW backgrounds.

7.4 Cross Section Calculations

The cross section for the $t\bar{t} \to e\mu$X process, $\sigma_{t\bar{t}}(m_t)$ can now be calculated using:

$$\sigma_{t\bar{t}}(m_t) = \frac{N_{obs} - < B >}{\mathcal{E} \times \int \mathcal{L}dt} \tag{7.8}$$

where N_{obs} is the number of events observed in the data, $< B >$ is the expected background, $\mathcal{E}$ is the corrected acceptance for the $t\bar{t}$ process and $\int \mathcal{L}dt$ is total

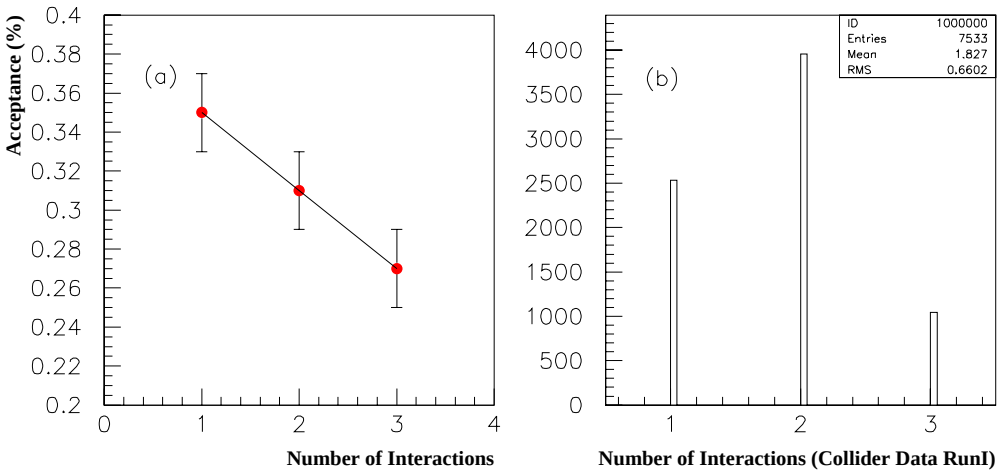

Figure 7.15: (a) Acceptance and number of interactions; (b) Number of interaction in collider data

integrated luminosity of the data sample. Note that $\mathcal{E}$ and hence $\sigma_{t\bar{t}}(m_t)$ are both functions of the top quark mass because of the coupling between the event kinematics and the detector/analysis acceptance.

To determine the total (statistical and systematic) error on the cross section, the statistical and systematic errors must be combined taking into account of all the error correlations. There are four inputs to the cross section calculation (see Equation 7.8) which give rise to six correlation terms. However, the error on N_{obs} is purely statistical which reduces the number of terms to three. The errors on acceptance ($\mathcal{E}$) and integrated luminosity $\mathcal{L}$ are assumed to be uncorrelated, leaving only the correlation terms between the background B and either $\mathcal{E}$ or $\mathcal{L}$. Taking this into account the error on the cross section can be expressed as:

$$\begin{aligned}\sigma^2_{\sigma_{t\bar{t}}} &= \left(\frac{\partial\sigma_{t\bar{t}}}{\partial N_{obs}}\right)^2 \sigma^2_{N_{obs}} + \left(\frac{\partial\sigma_{t\bar{t}}}{\partial B}\right)^2 \sigma^2_B + \left(\frac{\partial\sigma_{t\bar{t}}}{\partial\mathcal{E}}\right)^2 \sigma^2_{\mathcal{E}} \\ &+ \left(\frac{\partial\sigma_{t\bar{t}}}{\partial\mathcal{L}}\right)^2 \sigma^2_{\mathcal{L}} + \left(\frac{\partial\sigma_{t\bar{t}}}{\partial B}\right)\left(\frac{\partial\sigma_{t\bar{t}}}{\partial\mathcal{E}}\right)\sigma^2_{B\mathcal{E}} \\ &+ \left(\frac{\partial\sigma_{t\bar{t}}}{\partial B}\right)\left(\frac{\partial\sigma_{t\bar{t}}}{\partial\mathcal{L}}\right)\sigma^2_{B\mathcal{L}}, \end{aligned} \tag{7.9}$$

Source	Error (%)
Electron id	2.5 %
Muon id	8 %
Trigger	5 %
Jet energy scale	5.7 %
Monte Carlo generator	5 %
Top Quark Mass	9%
Luminosity	5.3 %

Table 7.3: Sources of systematic errors

$$= \sigma_{t\bar{t}}{}^2 \left[\frac{\sigma^2_{N_{obs}} + \sigma^2_B}{(N_{obs} - B)^2} + \frac{\sigma^2_{\mathcal{E}}}{\mathcal{E}^2} + \frac{\sigma^2_{\mathcal{L}}}{\mathcal{L}^2} + \frac{\sigma_B}{N_{obs} - B} \left(C_{B\mathcal{E}} \frac{\sigma_{\mathcal{E}}}{\mathcal{E}} + C_{B\mathcal{L}} \frac{\sigma_{\mathcal{L}}}{\mathcal{L}} \right) \right] \tag{7.10}$$

where $C_{B\mathcal{E}}$ and $C_{B\mathcal{L}}$ are the correlation coefficients which are given by:

$$C_{B\mathcal{E}} = \frac{\sum_{i=\text{syst.}} \sigma_{Bi}\sigma_{\mathcal{E}i}}{\sigma_B \sigma_{\mathcal{E}}}, \qquad C_{B\mathcal{L}} = \frac{\sigma_{\mathcal{L}}}{\sigma_B} \tag{7.11}$$

and have values of 0.226 and 0.068 respectively.

7.4.1 Systematic Uncertainties

Table 7.4.1 summarizes the systematic errors which affect the cross section measurement. The errors corresponding to the particle identification, trigger acceptance and luminosity calculations have already been discussed in Chapter 6. For these the systematic error is assumed to be $\pm$ the full calculation.

The remaining terms come from the uncertainty in the calibration of the jet energy scale (see Chapter 4.5.3), the choice of the Monte Carlo generator for the $t\bar{t}$ simulation and the value used for the top quark mass by the generator. The energy scale calibration has a known $\pm 1\sigma$ uncertainty on it [88]. The corresponding systematic error was determined by measuring the change in $t\bar{t}$ acceptance which results from a $\pm 1\sigma$ shift in the energy calibration. The error was taken as the difference in acceptance between central value and shifted values.

The generator uncertainty was estimated from a comparison of the $t\bar{t}$ acceptances calculated using events from HERWIG and ISAJET. While we believe

HERWIG to give the best description of the $t\bar{t}$ process, ISAJET which uses completely different evolution and fragmentation model still gives reasonable description of the $t\bar{t}$ data. Here, the systematic uncertainty was estimated from the changes in acceptance between two generators.

The value of m_t is measured by DØ is 172 $\pm$ 7 GeV [89]. We have used the central value to compute the signal acceptance which was used to calculate the cross section. The effect of $\pm$ 7 GeV uncertainty has been determined by calculating the acceptance between and 165(179) GeV (see Table 7.4). We make a conservative estimate of the systematic error by taking the difference between the central and shifted values. This is probably over generous since the error on the mass also includes a significant contribution from energy scale uncertainty.

7.5 Results

The four events which survive in the data correspond to an integrated luminosity of 108.3 $\pm$ 5.7 pb^{-1} For this we estimate a total background of 0.22 $\pm$ 0.14 events from the combination of the fake and physics processes. Table 7.4 summarizes the results of $\mathcal{E}$ for values of m_t between 150 and 185 GeV. By assuming the current DØ average value of 172 GeV for m_t and using the errors and correlations above, we obtain a cross section result of:

$$\sigma_{t\bar{t}} = 9.75 \pm 5.18(stat.) \pm 1.95(sys.)\ pb \tag{7.12}$$

where the statistical and systematic errors are quoted separately. Combining the errors give:

$$\sigma_{t\bar{t}} = 9.75 \pm 5.53\ pb \tag{7.13}$$

Summary Run 1, $\int \mathcal{L}dt = 108.3 \pm 5.7$ pb^{-1}		
Signal		
Top Mass (m_{top} GeV/c^2)	N^{expected}	$\varepsilon_{\rm tot}\times$BR (%)
150	3.38 $\pm$ 0.82	0.267 $\pm$ 0.048
155	3.03 $\pm$ 0.80	0.287 $\pm$ 0.051
160	2.74 $\pm$ 0.64	0.310 $\pm$ 0.055
165	2.49 $\pm$ 0.57	0.334 $\pm$ 0.059
170	2.22 $\pm$ 0.50	0.351 $\pm$ 0.063
172.1	2.11 $\pm$ 0.47	0.358 $\pm$ 0.064
175	1.96 $\pm$ 0.44	0.366 $\pm$ 0.065
180	1.74 $\pm$ 0.39	0.382 $\pm$ 0.068
185	1.54 $\pm$ 0.34	0.395 $\pm$ 0.070

Background	
Background process	N^{expected}
Z$\rightarrow \tau\tau \rightarrow e\mu$	0.09 $\pm$ 0.06
$WW \rightarrow e\mu$	0.08 $\pm$ 0.02
$\gamma^* \rightarrow \tau\tau \rightarrow e\mu$	0.01 $\pm$ 0.01
Fakes	0.04 $\pm$ 0.12
Total Background	0.22 $\pm$ 0.14
Events observed in Data	
Data	4

Table 7.4: Expected number of events, Efficiency times BR (%) and Total background for Run1 neural network analysis

Chapter 8

Comparison of the Neural Network and Conventional Analyses

Where all men think alike, no one thinks very much.

- Walter Lippmann

In this chapter we compare this analysis with the corresponding published DØ analysis of the $t\bar{t} \rightarrow e\mu$X channel which was performed by using conventional analysis techniques.

8.1 The Published DØ $t\bar{t} \rightarrow e\mu$X Analysis

The trigger requirement and initial data filtering used for the published analysis were identical to those used in the neural network analysis described here. Also, for the reasons discussed in Chapter 7.2, the first four of the analysis cuts are kept the same. However the cuts used on the missing energy and jet activity were somewhat more stringent in the published analysis. The cuts used were:

- $\not\!\!E_T^{cal} \geq 20$ GeV and $\not\!\!E_T \geq 10$ GeV
- $N_{\rm jets} \geq 2$ with $E_T^{\rm jet} \geq 20$ and $\mid \eta^{\rm jet} \mid \leq 2.5$
- $H_T^e \geq 120$ GeV

where H_T^e is the scaler sum of jets and leading electron transverse energies. This is defined as:

$$H_T^e = E_T^{ele} + \sum_{\rm jets} E_T^{\rm jet} \tag{8.1}$$

Cut	$t\bar{t}$ $\varepsilon \times \mathcal{BR}$ (%)	Signal $m_t = 170$ GeV/c^2	Background		Signal + Background	Data
			Fakes	Physics		
$E_T^e \geq 15$ GeV, $P_T^\mu \geq 15$ GeV, + $\Delta R_{\mu,\text{jets}} \geq 0.5$, $\Delta R_{\mu,ele} \geq 0.25$	0.53 ± 0.11	3.4 ± 0.7	12 ± 1	39 ± 8	54 ± 9	58
$\not\!\!E_T^{cal} \geq 20$ GeV, $\not\!\!E_T \geq 10$ GeV	0.49 ± 0.10	3.1 ± 0.7	2.6 ± 0.3	14 ± 3	20 ± 4	20
$N_{\text{jets}} \geq 2$, $E_T^{\text{jets}} \geq 20$	0.39 ± 0.08	2.5 ± 0.5	0.20 ± 0.13	0.31 ± 0.09	2.9 ± 0.7	4
$H_T^e \geq 120$ GeV	0.32 ± 0.06	2.0 ± 0.4	0.08 ± 0.13	0.17 ± 0.07	2.2 ± 0.6	3

Table 8.1: The expected and observed number of events as a function of conventional cuts.

where $E_T^{ele} \geq 15$ GeV, $E_T^{\text{jet}} \geq 15$ GeV and $|\eta^{\text{ele,jet}}| \leq 2.5$.

The analysis proceeded in a similar manner to that of neural network analysis before the $\not\!\!E_T^{cal}$ cut. At this stage, an additional cut on $\not\!\!E_T$ was imposed and the $\not\!\!E_T^{cal}$ cut value was raised to ≥ 20 GeV. This was done to reduce the fake background. The remaining cuts were chosen following an optimization of the $signal/\sqrt{background}$ ratio and led to cuts of $N_{\text{jets}} \geq 2$ with $E_T^{\text{jet}} \geq 20$, $|\eta^{\text{jet}}| \leq 2.5$ and $H_T^e \geq 120$ GeV.

Table 8.1 shows the number of events expected and observed as a function of each level of conventional analysis cuts. Table 8.2 summarizes acceptance ($\mathcal{E}$) for the $t\bar{t} \rightarrow e\mu$X and background processes. This is the direct analog of the neural network results shown in Table 7.4. Three candidate events were observed in data with a total background of 0.24 ± 0.15. For a top mass of 172 GeV, this gives a cross section of:

$$\sigma_{t\bar{t}} = 7.84 \pm 4.94(stat.) \pm 1.57(sys.) \text{ pb} \tag{8.2}$$

Note that this differs from the value of reference [90] because of the improvements made in the treatment of multiple-interaction corrections (see Chapter 7.3) and some additional corrections to the treatment of the trigger simulation. However the updated and published results agree well within the quoted errors.

Summary Run 1, $\int \mathcal{L}dt = 108.3 \pm 5.7$ pb^{-1}		
Signal		
Top Mass ($m_{\rm top}$ GeV/c^2)	N$^{\rm expected}$	$\epsilon_{\rm tot}\times$BR (%)
150	2.92 $\pm$ 0.55	0.230 $\pm$ 0.041
155	2.67 $\pm$ 0.50	0.253 $\pm$ 0.045
160	2.43 $\pm$ 0.45	0.275 $\pm$ 0.049
165	2.24 $\pm$ 0.42	0.301 $\pm$ 0.054
170	2.00 $\pm$ 0.37	0.317 $\pm$ 0.057
172.1	1.91 $\pm$ 0.36	0.325 $\pm$ 0.058
175	1.79 $\pm$ 0.33	0.334 $\pm$ 0.060
180	1.61 $\pm$ 0.30	0.354 $\pm$ 0.063
185	1.43 $\pm$ 0.27	0.368 $\pm$ 0.066

Background	
Background process	N$^{\rm expected}$
Z$\rightarrow \tau\tau \rightarrow e\mu$	0.09 $\pm$ 0.08
$WW \rightarrow e\mu$	0.07 $\pm$ 0.02
$\gamma^* \rightarrow \tau\tau \rightarrow e\mu$	0.01 $\pm$ 0.01
Fakes	0.08 $\pm$ 0.13
Total Background	0.24 $\pm$ 0.15
Events observed in Data	
Data	3

Table 8.2: Event yields for the signal, background and data for the Run 1 conventional analysis

8.2 Comparison of the Selection Efficiencies and the Cross Section Results

Because conventional analysis methods do not exploit the correlations between the variables on which the cuts are being applied, they tend to induce a loss of signal efficiency. Figure 8.1 shows a comparison of signal and background efficiencies from the conventional and neural network analyses. The open circles represent the results of a grid search using sets of cuts on $E_T^e, E_T^{\rm jet1}, E_T^{\rm jet2}, \not\!\!E_T^{cal}$ and H_T^e. The solid points are the result of a single cut on $O_{NN}^{\rm comb}$. This clearly shows that for a given amount of background, the neural network method gives a better signal efficiency than a set of conventional cuts.

The increase in efficiency can also be understood by comparing cuts on H_T^e and $\not\!\!E_T^{cal}$ for the two analyses. Figures 8.2 show scatter plots of $\not\!\!E_T^{cal}$ and H_T^e before 8.2(a) and after 8.2(b) the application of $O_{NN}^{\rm comb}$ cut. The solid lines represent the cuts used in the published analysis. It can be clearly seen that the contour cut of the neural network analysis gives the better signal efficiency than conventional cuts, especially in the region $80 \geq H_T^e \leq 120$ GeV and $\not\!\!E_T^{cal} \geq 20$ GeV.

A detailed comparison of $t\bar{t} \rightarrow e\mu$X acceptance between the two analyses is shown in Figure 8.3. For the purpose of clarity, the errors shown are only statistical and we note that the systematic errors are highly correlated. For 170 GeV, the neural network analysis has a signal efficiency which is 10% more than the conventional analysis. In addition, the comparison of Tables 7.4 and 8.2 shows that the total background is also slightly lower in the new analysis. However, because of the large statistical error on instrumental background calculations, this is hard to quantify.

The three candidate events selected from the data by conventional analysis were also found in the neural network analysis. In addition to these, one additional event was selected. This was rejected in the conventional analysis because it failed the H_T^e cut. It satisfies all the selection criteria and kinematically lies in the part H_T^e and $\not\!\!E_T^{cal}$ plane which is recovered by the neural network analysis (see Figure 8.2). The properties of all four candidate events are listed in Appendix C. This also contains pictorial displays for each event.

A further test of signal compatibility is provided by the reconstructed top quark mass for each event. Because each event contains two neutrinos the calculation is non-trivial and conventional kinematical fitting techniques do not work. For this study we have used the neutrino phase space weighting technique which was developed by DØ for to solve this problem [91]. The resulting probability distributions for the four candidates are shown in Figure 8.4. These lead to the reconstructed masses of 154, 158, 170 and 140 GeV for event 417, 12814, 26920 and 5566 respectively which are all highly compatible with the $t\bar{t} \rightarrow e\mu$X hypothesis. We further note that the fitted top quark mass from the first three events alone

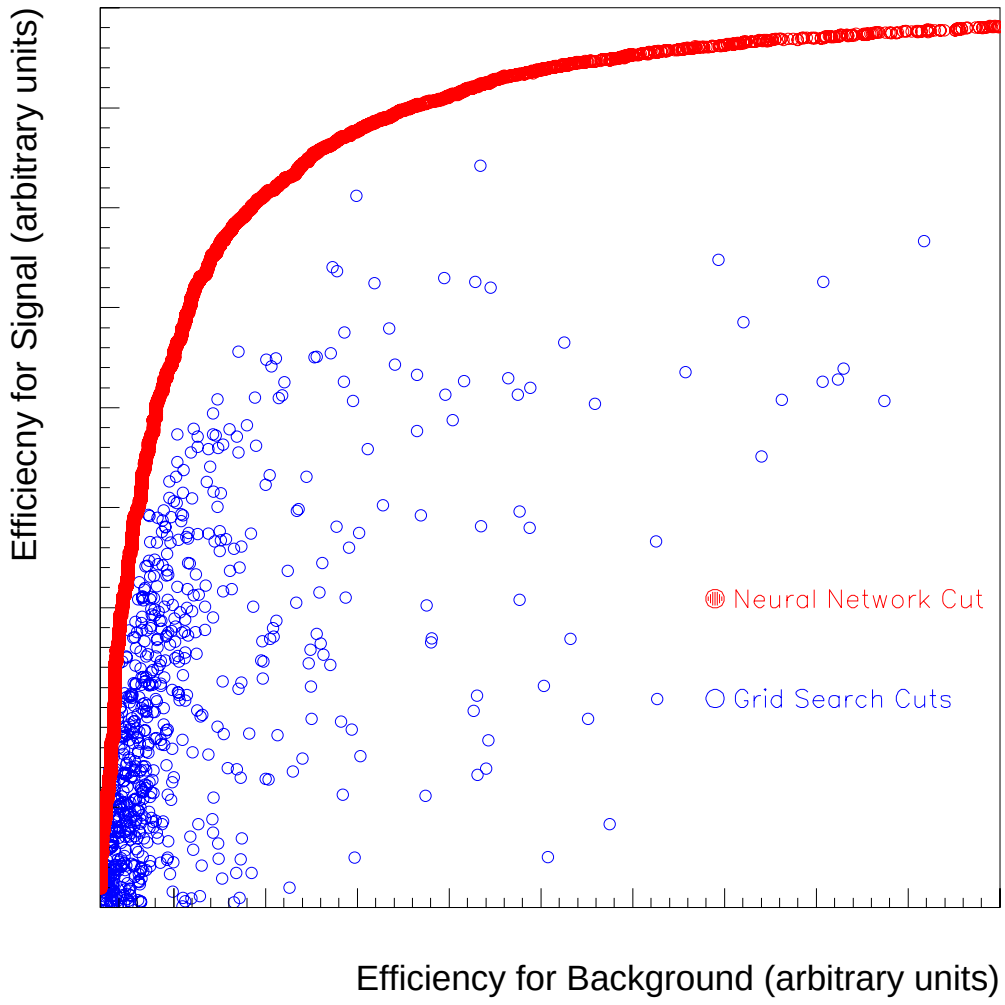

Figure 8.1: Comparison of signal and background efficiencies for the conventional and neural network cuts.

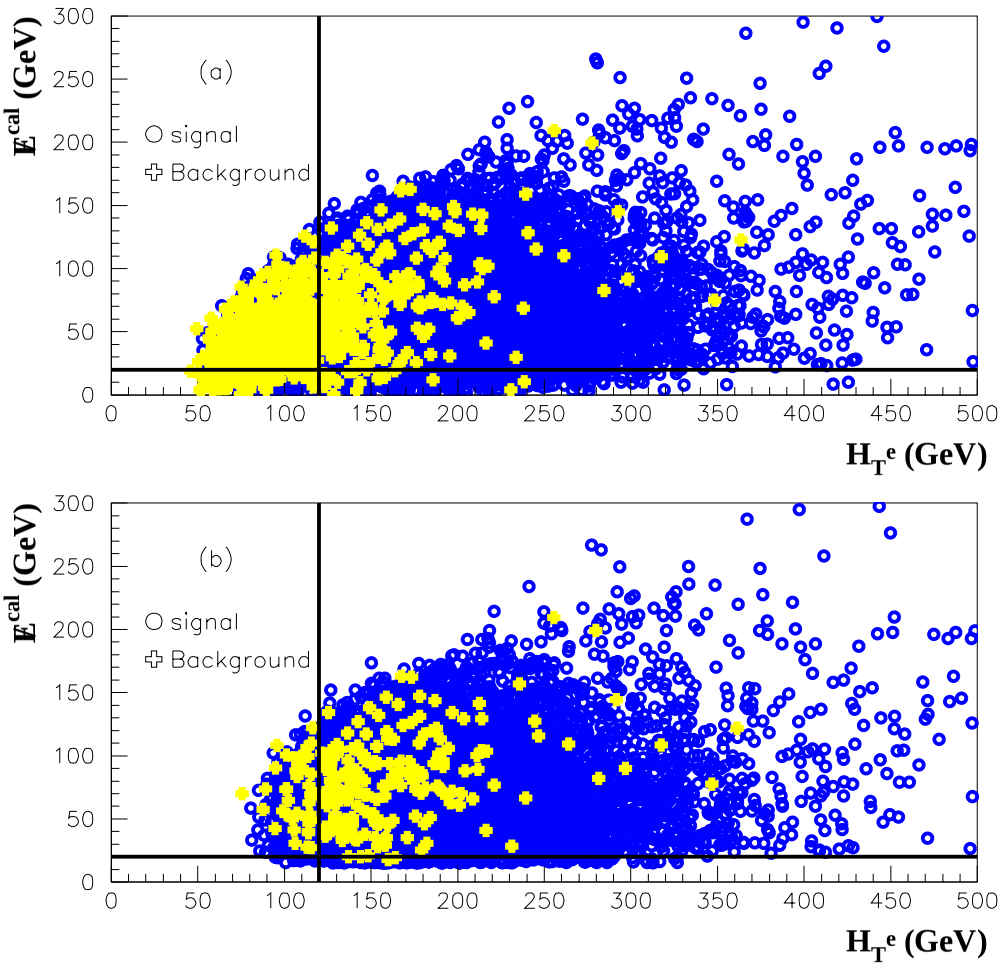

Figure 8.2: $\not\!\!E_T^{cal}$ and H_T^e scatter plots for signal and background (a) before any cuts (b) after neural network cut. The solid lines indicate the cut values used in the conventional analysis.

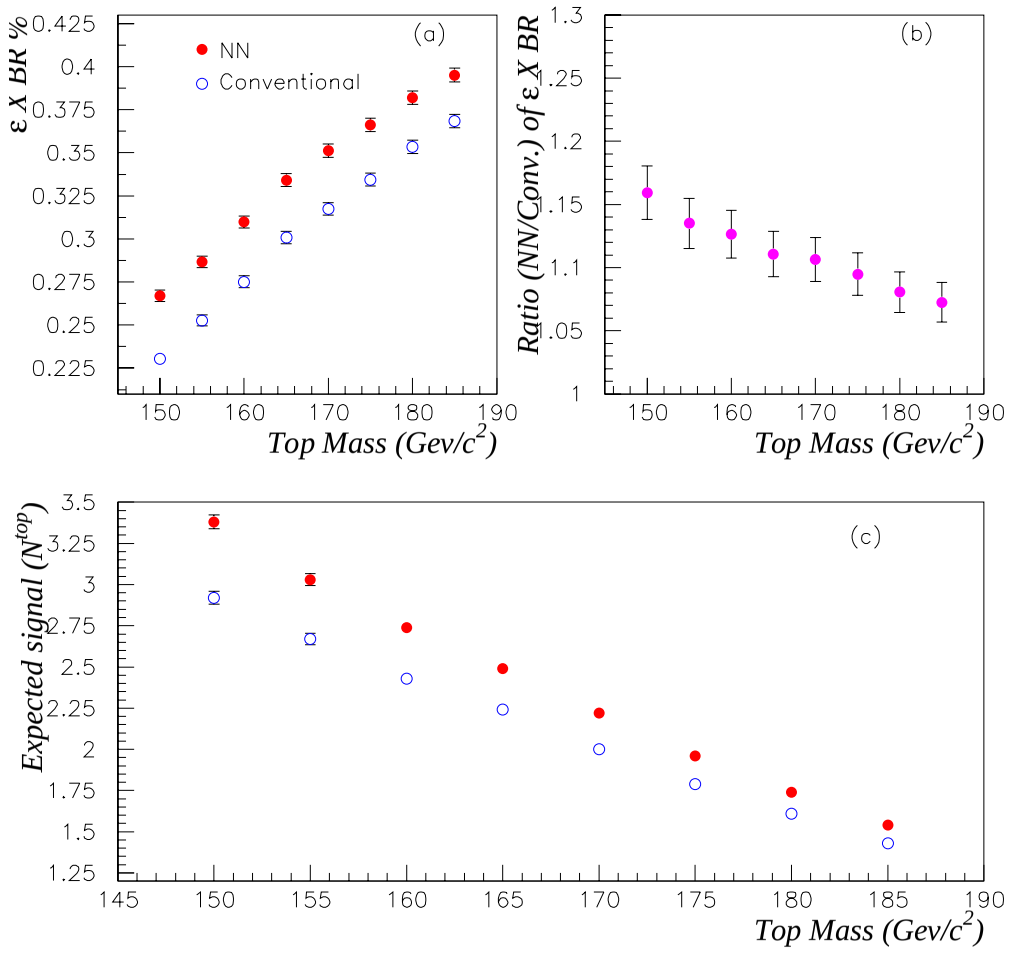

Figure 8.3: Comparison of the neural network and conventional $t\bar{t} \rightarrow e\mu$X analysis for Run 1 (a) Acceptance ($\mathcal{E}$). (b) Ratio of NN to conventional analysis efficiency (c) Expected number of events. The errors shown are statistical only.

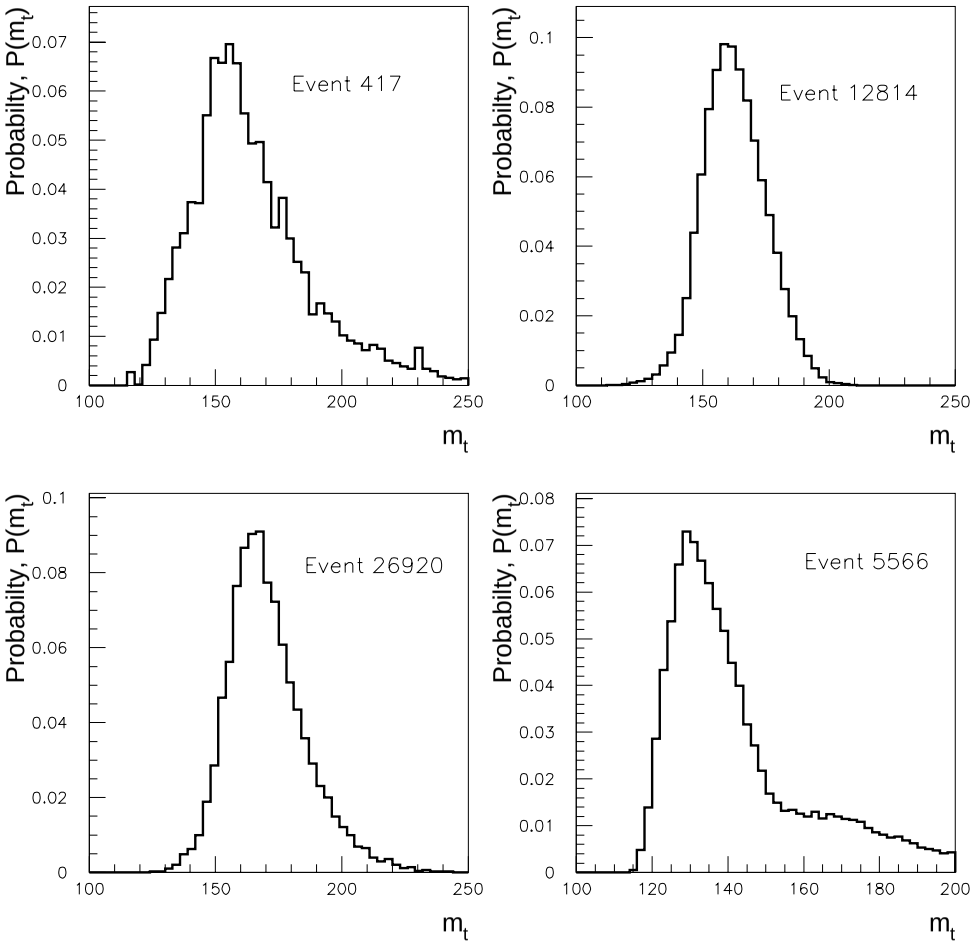

Figure 8.4: Probability distributions verses m_t for the four $e\mu$ candidates.

was 170.1 ± 14.5 GeV [91] indicating that the effects of smearing and fragmentation tend to decrease the apparent reconstructed mass value.

In Figure 8.5 we show the comparison of the two cross section measurements, together with the predictions of NLO QCD [26, 27, 28]. The old and and new measurements are in good agreement within the large errors and both are quite consistent with the QCD calculations.

The only other comparable measurement of $\sigma_{t\bar{t}}$ from the $t\bar{t} \rightarrow e\mu$X process is from the CDF experiment. Based on 109 pb^{-1} of data, they observed 7 events with a computed background of 0.74 ± 0.21 events. For their measured value of the top quark mass of 176 GeV, this corresponds to a cross section of $12.7^{+6.4}_{-4.9}$ pb [92]. This is some what higher than both of the DØ measurements, but is still compatible within the experimental errors.

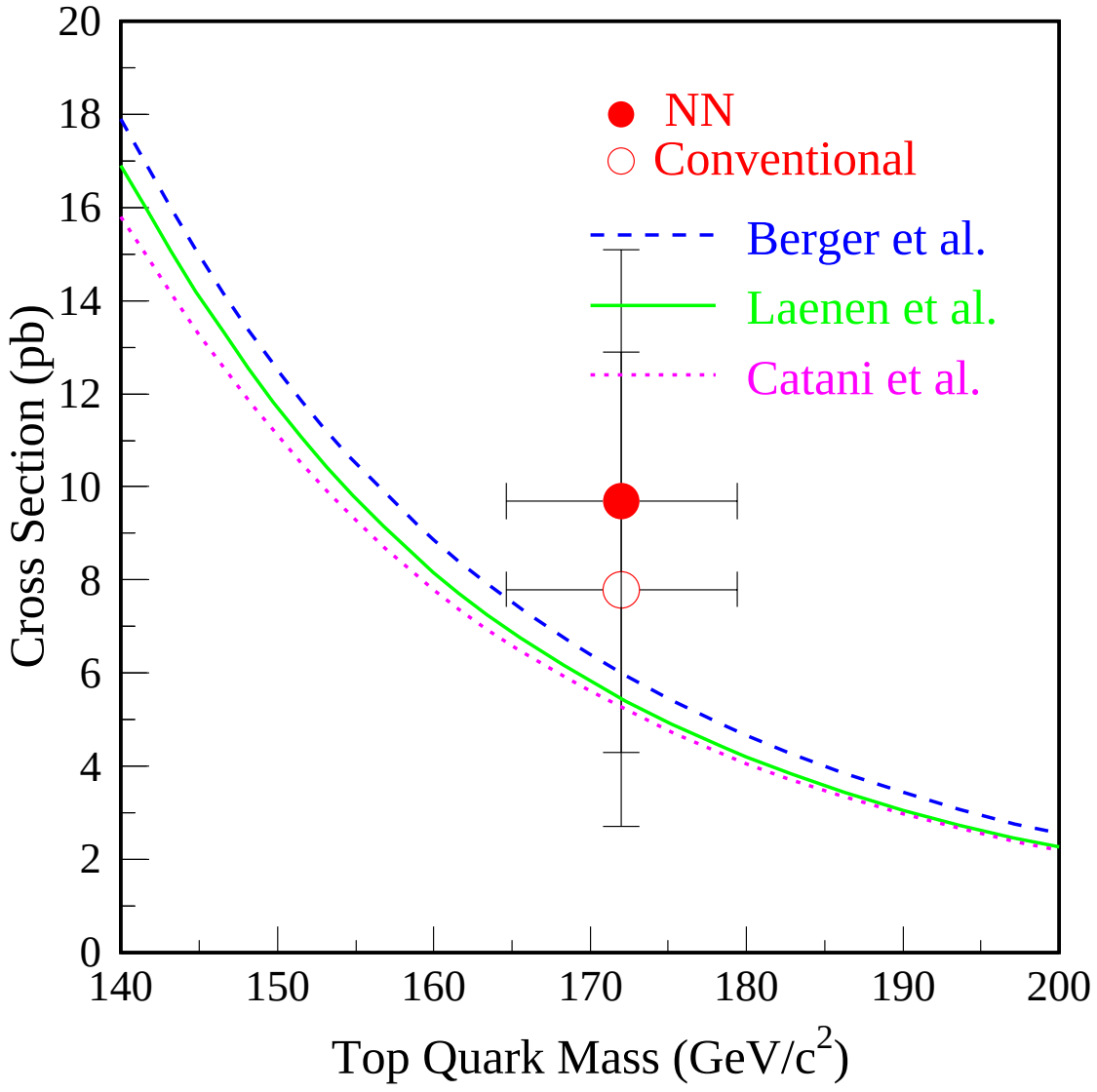

Figure 8.5: The $t\bar{t}$ production cross section as measured using the $t\bar{t} \rightarrow e\mu$X channel. Also shown are NLO QCD calculations from Berger, Laenen and Catani *et. al.* The solid point is the result from this analysis and the open point is an updated version of the result using the published conventional analysis.

Chapter 9

Conclusions

You may wonder what this has to do with the fancy things like protons and neutrons.

- John Baez, Mathematical Methods class at UCR in 1997.

We have performed a new measurement of the $t\bar{t}$ production cross section using $e\mu$ channel for $p\bar{p}$ collisions at $\sqrt{s} = 1.8$ TeV using neural network techniques. The result, based on the full Run 1 data set (1992-96), demonstrates the power of the artificial neural networks to discriminate between signal and background processes which are both rare and of very similar topology. We have further demonstrated that this analysis of the $t\bar{t} \to e\mu$X channel provides a significant gain in acceptance when compared to the corresponding published analysis which used more conventional analysis techniques.

For the 108 pb^{-1} of Run 1 data we have a calculated signal yield of 2.2 ± 0.5 with a background of 0.22 ± 0.14 events. Four events were observed in the data, giving a cross section measurement of:

$$\sigma_{t\bar{t}} = 9.75 \pm 5.53 \text{ pb} \tag{9.1}$$

This is in good agreement with the result from the published DØ analysis and is consistent with the predications of NLO QCD calculations.

The techniques developed for this analysis will be very useful during the next Tevatron collider run (Run II) which is scheduled to begin in the spring of 2001. For this run, the expected total integrated luminosity will be 2 fb^{-1}, 20 times more than Run 1 and at the higher energy of $\sqrt{s} = 2.0$ TeV. This will result in the production of about twenty five times more $t\bar{t}$ events as in the previous run. Furthermore, the DØ detector has been upgraded to improve it's efficiency for observing $t\bar{t}$ events. With large samples of $t\bar{t}$ events in the dilepton channels, the top cross section measurements will no longer be limited by statistics and the systematic

study of the background will become more important. The tools provided by ANN analysis are well suited to this task. These analyses may prove to be the most important for the precise studies of the cross section and the top quark mass in the next run.

Appendix A

Triggers used for Data Collection

A.1 Main Ring Triggers Definitions

- mrbs-loss (MRBS): The trigger is disabled for the 0.4 s after a proton bunch is injected into the Main Ring. This vetoes events during injection and transition and allows a small recovery time for the muon and calorimeter systems. The typical deadtime for mrbs-loss veto is ~ 17 %.

- micro-blank (MB): The trigger is disabled for events where Main Ring bunches are present during the livetime of the muon system which is $\approx \pm 800$ ns centered on the $p\bar{p}$ crossing. The calorimeter livetime is somewhat longer ($\sim 2\mu$s), so this is not completely efficient for vetoing events with Main Ring energy in the calorimeter. The typical deadtime for micro-blank is ~ 7 %.

- max-live (ML): The trigger is disabled during periods of overlap between MRBS and MB. This corresponds to the first few passes of newly injected beam passing through the detector.

- good-cal (GC): The trigger is disabled during periods of overlap between MRBS and MB and during MB periods of highest intensity beam leakage. This leakage was measured by a set of scintillator arrays surrounding the Main Ring beam-pipe upstream of the DØ detector.

- good-beam (GB): The trigger is disabled during periods of either MRBS or MB. good-beam is the cleanest possible running condition.

A.2 The L1 and L2 Triggers Definitions

Name	Run	Level 1	Level 2	Used by
ele-jet	1a	1 EM tower, $E_T > 10$ GeV , $\|\eta\| < 2.6$ 2 jet towers, $E_T > 5$ GeV MRBS	1 e, $E_T > 15$ GeV , $\|\eta\| < 2.5$ 2 jets ($\Delta R = 0.3$), $E_T > 10$ GeV , $\|\eta\| < 2.5$ $\not\!\!E_T^{\rm cal} > 10$ GeV	ee,$e\mu$,$e\nu$ $e + jets$ $e + jets/\mu$
ele-jet-high	1b,1c	1 EM tower, $E_T > 12$ GeV , $\|\eta\| < 2.6$ 2 jet towers, $E_T > 5$ GeV , $\|\eta\| < 2.0$ ML	1 e, $E_T > 15$ GeV , $\|\eta\| < 2.5$ 2 jets ($\Delta R = 0.3$), $E_T > 10$ GeV , $\|\eta\| < 2.5$ $\not\!\!E_T^{\rm cal} > 14$ GeV	ee,$e\mu$,$e\nu$ $e + jets$ $e + jets/\mu$
ele-jet-higha	1c	1 EM tower, $E_T > 12$ GeV , $\|\eta\| < 2.6$ 2 jet towers, $E_T > 5$ GeV , $\|\eta\| < 2.0$ 1 EX tower, $E_T > 15$ GeV ML	1 e, $E_T > 17$ GeV , $\|\eta\| < 2.5$ 2 jets ($\Delta R = 0.3$), $E_T > 10$ GeV , $\|\eta\| < 2.5$ $\not\!\!E_T^{\rm cal} > 14$ GeV	ee,$e\mu$,$e\nu$ $e + jets/\mu$
mu-ele	1a	1 EM tower, $E_T > 7$ GeV 1 μ, $\|\eta\| < 2.4$ MRBS	1 e, $E_T > 7$ GeV 1 μ, $P_T > 5$ GeV , $\|\eta\| < 2.4$	$e\mu$
	1b	1 EM tower, $E_T > 7$ GeV 1 μ, $\|\eta\| < 2.4$ GC	1 e, $E_T > 7$ GeV , $\|\eta\| < 2.5$ 1 μ, $P_T > 8$ GeV/c , $\|\eta\| < 2.4$	$e\mu$
mu-ele-high	1c	1 EM tower, $E_T > 10$ GeV , $\|\eta\| < 2.5$ 1 μ, $\|\eta\| < 2.4$ GC	1 e, $E_T > 10$ GeV , $\|\eta\| < 2.5$ 1 μ, $P_T > 8$ GeV/c , $\|\eta\| < 1.7$	$e\mu$
mu-jet-high	1a	1 μ, $\|\eta\| < 2.4$ 1 jet tower, $E_T > 5$ GeV GB	1 μ, $P_T > 8$ GeV/c , $\|\eta\| < 1.7$ 1 jet ($\Delta R = 0.7$), $E_T > 15$ GeV	$e\mu$,$\mu\mu$ $\mu + jets$ $\mu + jets/\mu$
	1b	1 μ, $P_T > 7$ GeV/c , $\|\eta\| < 1.7$ 1 jet tower, $E_T > 5$ GeV , $\|\eta\| < 2.0$ GC	1 μ, $P_T > 10$ GeV/c , $\|\eta\| < 1.7$, scint 1 jet ($\Delta R = 0.7$), $E_T > 15$ GeV , $\|\eta\| < 2.5$	$e\mu$,$\mu\mu$ $\mu + jets$ $\mu + jets/\mu$
mu-jet-cal	1b	1 μ, $P_T > 7$ GeV/c , $\|\eta\| < 1.7$ 1 jet tower, $E_T > 5$ GeV , $\|\eta\| < 2.0$ GC	1 μ, $P_T > 10$ GeV/c , $\|\eta\| < 1.7$ cal confirm, scint 1 jet ($\Delta R = 0.7$), $E_T > 15$ GeV , $\|\eta\| < 2.5$	$\mu\mu$,$\mu + jets$ $\mu + jets/\mu$
mu-jet-cent	1b	1 μ, $\|\eta\| < 1.0$ 1 jet tower, $E_T > 5$ GeV , $\|\eta\| < 2.0$ GC	1 μ, $P_T > 10$ GeV/c , $\|\eta\| < 1.0$, scint 1 jet ($\Delta R = 0.7$), $E_T > 15$ GeV , $\|\eta\| < 2.5$	$e\mu$,$\mu\mu$ $\mu + jets$ $\mu + jets/\mu$
	1c	1 μ, $\|\eta\| < 1.0$ 1 jet tower, $E_T > 5$ GeV , $\|\eta\| < 2.0$ 2 jet towers, $E_T > 3$ GeV GC	1 μ, $P_T > 12$ GeV/c , $\|\eta\| < 1.0$, scint 1 jet ($\Delta R = 0.7$), $E_T > 15$ GeV , $\|\eta\| < 2.5$	$e\mu$,$\mu\mu$
mu-jet-cencal	1b	1 μ, $\|\eta\| < 1.0$ 1 jet tower, $E_T > 5$ GeV , $\|\eta\| < 2.0$ GC	1 μ, $P_T > 10$ GeV/c , $\|\eta\| < 1.0$ cal confirm, scint 1 jet ($\Delta R = 0.7$), $E_T > 15$ GeV , $\|\eta\| < 2.5$	$\mu\mu$, $\mu + jets$ $\mu + jets/\mu$
	1c	1 μ, $\|\eta\| < 1.0$ 1 jet tower, $E_T > 5$ GeV , $\|\eta\| < 2.0$ 2 jet towers, $E_T > 3$ GeV GC	1 μ, $P_T > 12$ GeV/c , $\|\eta\| < 1.0$ cal confirm, scint 1 jet ($\Delta R = 0.7$), $E_T > 15$ GeV , $\|\eta\| < 2.5$	$e\mu$, $\mu\mu$

Appendix B

The Branching Ratios for $t\bar{t} \to l_1 l_2$X Decays

In modeling $t\bar{t}$ events for this analysis, we required both of the W bosons in the events to decay to leptons (e,μ or $\tau \to e$ or μ). Further to calcualte the total cross section, we have to correct for the fact that dilepton channel has a total bracnhing ratio of 6.85 %. This follows form the following calculations.

The total BR for $t\bar{t} \to$ dileptons (e,μ or $\tau \to e$ or μ) is

$$(4/81) \times (1 + (0.178) \times (0.178) + 2 \times (0.178)) = 0.0685 \qquad \text{(B.1)}$$

where 0.178 is the BR for $\tau \to e$ or μ.[93]. See Table B.1 for branching ratio details.

Main Process $t\bar{t} \to WW$	BR	Sub-process (Like $\tau \to e$ or μ)	BR (sub-process)	Total BR
$\to ee$	1/81	na	na	4/81
$\to \mu\mu$	1/81	na	na	
$\to e\mu$	2/81	na	na	
$\to \tau\tau$	1/81	ee	0.0317	$4/81 \times 0.0317$
		$\mu\mu$	0.0317	
		$e\mu$	0.0634	
$\to e\tau$	2/81	ee	0.178	$4/81 \times 0.178$
		$e\mu$	0.178	
$\to \mu\tau$	2/81	$\mu\mu$	0.178	$4/81 \times 0.178$
		μe	0.178	

Table B.1: Branching ratios for $t\bar{t} \to ee$ or $e\mu$ or $\mu\mu$ including all the decays like $\tau \to e$ or μ

Appendix C

The properties of the Four Candidate Events

Run 1a Candidate Run=58796, Event=7338(417)

N_{vertex}=1	$z_{vertex1}$=-1.75	mrbs-loss=0	micro-blank=0
mu-ele=1	ele-jet-high=0	mu-jet-high=0	mu-jet-cent=0
$N_{electron}$=1	E_T^e=97.94	η^e=0.40	η_{det}^e=5.0
ϕ^e=4.84	χ^2=50.58	isolation=0.02	$\sigma_{\rm trkmatch}$=0.15
dE/dx=0.95	elkl-all=0.0095	elkl-notrd=0.0259	
N_{muon}=1	P_T^μ=193.04	η^μ=0.33	quad=2.00
ϕ^μ=1.82	$N_{\rm trkm}$=1.00	calmip=3.37	ifw41=0.00
bdl1=0.68	mtchfrac=0.00	mtcefrh1=0.00	ghfarc=0.00
IP^{3D}=0.00	IP^{bend}=0.00	$IP^{nonbend}$=5.65	T_0^{float}=39.07
muctag=0	scint-active=0.00	χ^2_{gfit}=14.76	
No of hits A layer=2	No of hits B layer=3	No of hits C layer=3	
$\not\!\!E_T$=125.13	$\not\!\!E_T^{cal}$ =104.60	$N^{\rm jets,E_T\geq 15}$=2	
$E_T^{\rm jet1}$=26.42	$\eta^{\rm jet1}$=-0.71	$\eta_{det}^{\rm jet1}$=-0.72	$\phi^{\rm jet1}$=3.51
$E_T^{\rm jet1}$=24.38	$\eta^{\rm jet2}$=1.09	$\eta_{det}^{\rm jet2}$=1.07	$\phi^{\rm jet2}$=4.10
H_T=148.74	$M_{e\mu}$=274.63	$\Delta R_{e\mu}$=3.02	$O_{NN}^{\rm comb}$=0.922

Run 1b Candidate Run=84676, Event=12814

N_{vertex}=1	$z_{vertex1}$=-6.17	mrbs-loss=0	micro-blank=0
mu-ele=1	ele-jet-high=1	mu-jet-high=1	mu-jet-cent=0
$N_{electron}$=1	E_T^e=75.45	η^e=-0.40	η_{det}^e=-5.0
ϕ^e=3.16	χ^2=33.22	isolation=0.02	$\sigma_{trkmatch}$=1.05
dE/dx=0.69	elkl-all=0.095	elkl-notrd=0.048	
N_{muon}=1	P_T^μ=27.35	η^μ=-0.45	quad=3.00
ϕ^μ=2.75	N_{trkm}=1.00	calmip=3.23	ifw41=0.00
bdl1=0.71	mtchfrac=1.00	mtcefrh1=0.30	ghfarc=1
IP^{3D}=2.26	IP^{bend}=-2.39	$IP^{nonbend}$=-3.00	T_0^{float}=27.67
muctag=0	scint-active=1.00	χ^2_{gfit}=1.45	
No of hits A layer=4	No of hits B layer=2	No of hits C layer=3	
$\not\!\!E_T$=40.06	$\not\!\!E_T^{cal}$ =62.26	$N^{\mathrm{jets,E_T\geq 15}}$=3	
E_T^{jet1}=91.95	η^{jet1}=-0.17	$\eta_{det}^{\mathrm{jet1}}$=-0.23	ϕ^{jet1}=5.14
E_T^{jet2}=35.15	η^{jet2}=-0.31	$\eta_{det}^{\mathrm{jet2}}$=-0.38	ϕ^{jet2}=1.17
E_T^{jet3}=28.67	η^{jet3}=0.39	$\eta_{det}^{\mathrm{jet3}}$=0.33	ϕ^{jet3}=1.63
H_T=231.22	$M_{e\mu}$=18.72	$\Delta R_{e\mu}$=0.42	O_{NN}^{comb}=0.94

Run 1b Candidate Run=90422, Event=26920

N_{vertex}=1	$z_{vertex1}$=18.23	mrbs-loss=0	micro-blank=0
mu-ele=1	ele-jet-high=1	mu-jet-high=0	mu-jet-cent=1
$N_{electron}$=1	E_T^e=49.41	η^e=1.76	η_{det}^e=19.00
ϕ^e=2.72	χ^2=17.49	isolation=0.06	$\sigma_{trkmatch}$=8.57
dE/dx=3.64	elkl-all=0.29	elkl-notrd=0.29	
N_{muon}=1	P_T^μ=16.77	η^μ=-0.19	quad=2.00
ϕ^μ=1.38	N_{trkm}=2.00	calmip=3.71	ifw41=1.00
bdl1=0.65	mtchfrac=1.00	mtcefrh1=0.27	ghfarc=1.00
IP^{3D}=0.00	IP^{bend}=0.00	$IP^{nonbend}$=5.65	T_0^{float}=29.80
muctag=0	scint-active=1.00	χ^2_{gfit}=235.99	
No of hits A layer=3	No of hits B layer=3	No of hits C layer=3	
$\not\!\!E_T$=22.94	$\not\!\!E_T^{cal}$ =11.74	$N^{\mathrm{jets,E_T\geq 15}}$=2	
E_T^{jet1}=48.14	η^{jet1}=0.21	$\eta_{det}^{\mathrm{jet1}}$=0.40	ϕ^{jet1}=5.64
E_T^{jet2}=26.03	η^{jet2}=-0.97	$\eta_{det}^{\mathrm{jet2}}$=-0.83	ϕ^{jet2}=5.51
H_T=123.58	$M_{e\mu}$=74.84	$\Delta R_{e\mu}$=2.37	O_{NN}^{comb}=0.93

Run 1b Candidate Run=90834, Event=5566 (New event from this analysis)

N_{vertex}=1	$z_{vertex1}$=-17.50	mrbs-loss=0	micro-blank=0
mu-ele=1	ele-jet-high=1	mu-jet-high=0	mu-jet-cent=1
$N_{electron}$=1	E_T^e=27.22	η^e=-1.34	η_{det}^e=-15.0
ϕ^e=5.91	χ^2=133.64	isolation=0.06	$\sigma_{trkmatch}$=0.56
dE/dx=0.83	elkl-all=0.2	elkl-notrd=0.44	
N_{muon}=1	P_T^μ=19.57	η^μ=0.56	quad=1.00
ϕ^μ=0.42	N_{trkm}=1.00	calmip=0.36	ifw41=1.00
bdl1=0.75	mtchfrac=1.00	mtcefrh1=0.63	ghfarc=1.00
IP^{3D}=4.55	IP^{bend}=5.37	$IP^{nonbend}$=53.15	T_0^{float}=19.22
muctag=0	scint-active=1.00	χ^2_{gfit}=401.05	
No of hits A layer=4	No of hits B layer=3	No of hits C layer=3	
$\not\!\!E_T$=44.66	$\not\!\!E_T^{cal}$ =25.70	$N^{jets,E_T \geq 15}$=2	
E_T^{jet1}=46.60	η^{jet1}=0.85	η_{det}^{jet1}=0.71	ϕ^{jet1}=3.33
E_T^{jet2}=27.03	η^{jet2}=-1.74	η_{det}^{jet2}=-1.84	ϕ^{jet2}=3.40
H_T=100.86	$M_{e\mu}$=53.78	$\Delta R_{e\mu}$=2.06	O_{NN}^{comb}=0.91

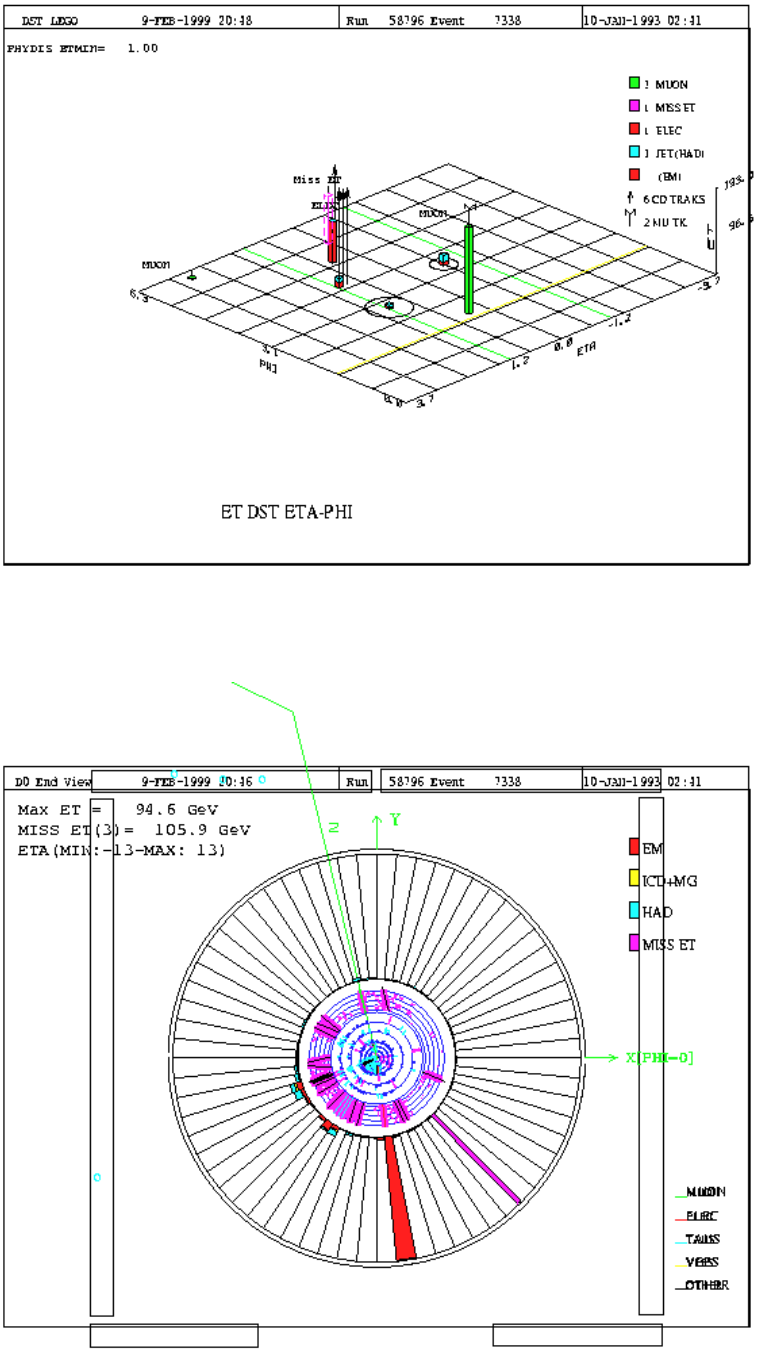

Figure C.1: Event displays of event 58796/7338 (Run 1a, event 417)

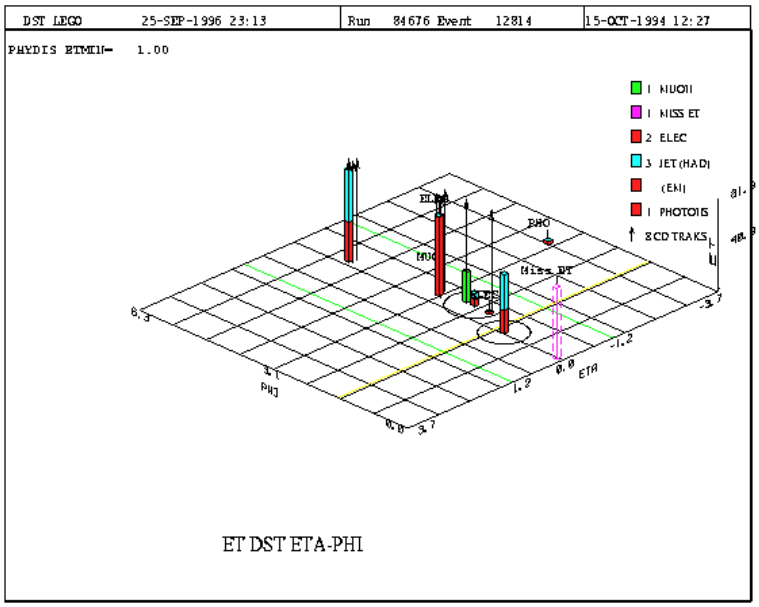

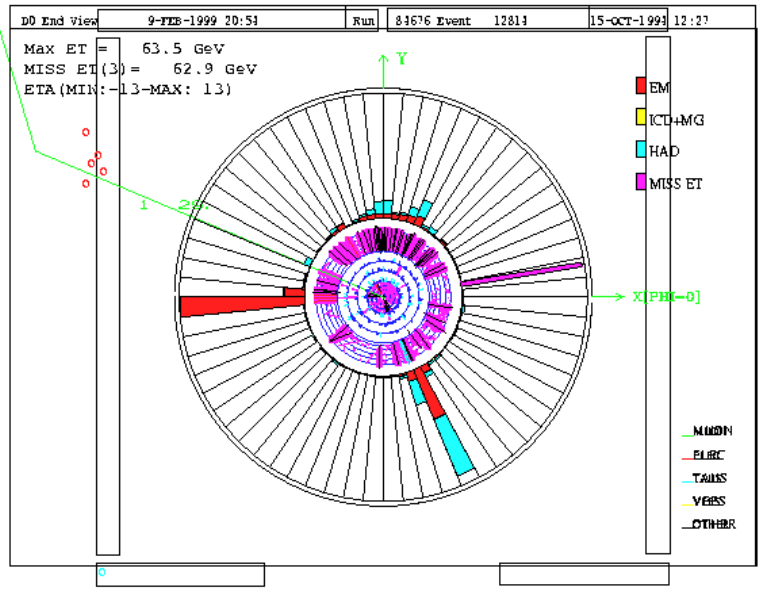

Figure C.2: Event displays of event 84676/12814 (Run 1b)

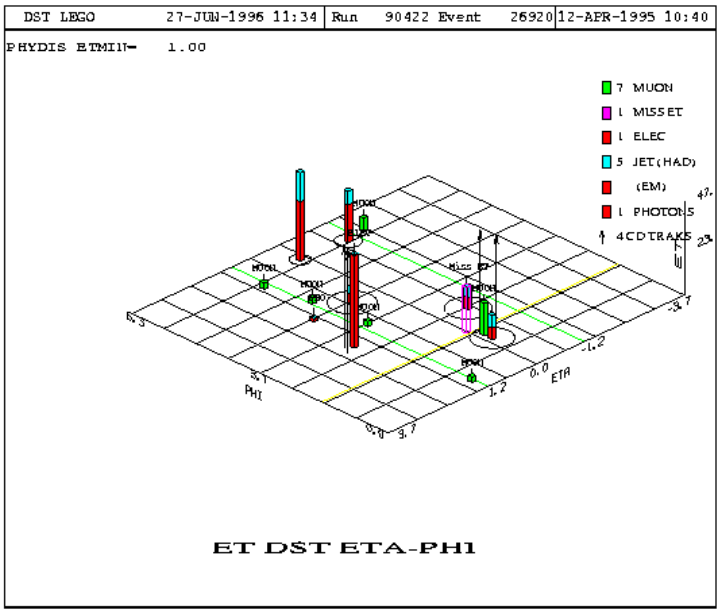

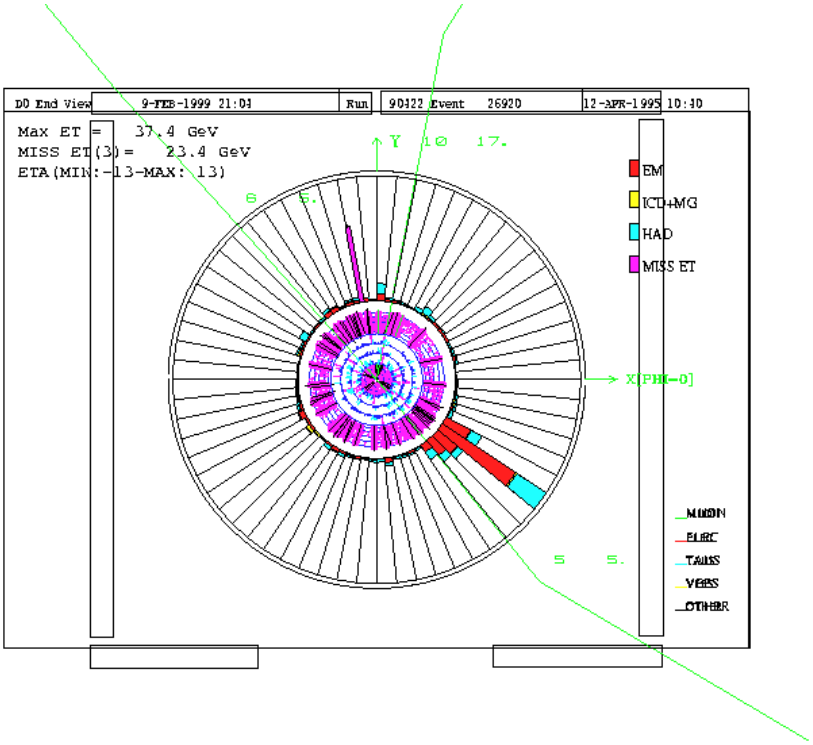

Figure C.3: Event displays of event 90422/26920 (Run 1b)

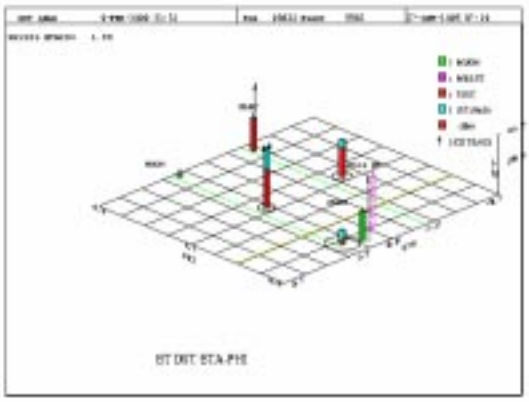

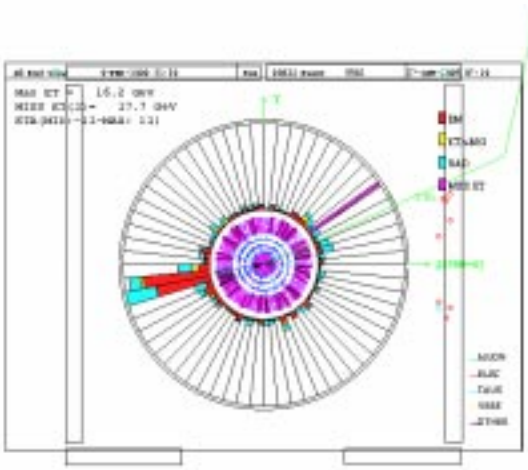

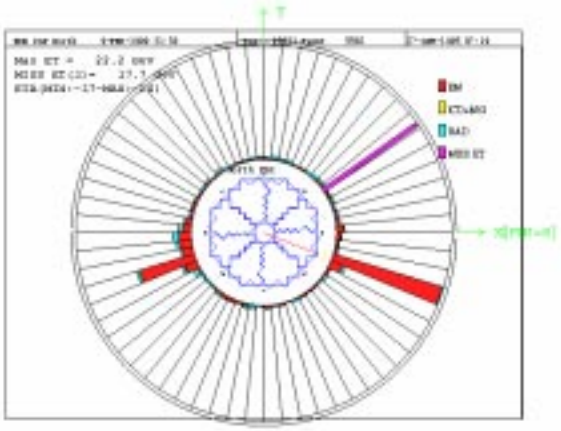

Figure C.4: Event displays of event 90834/5566 (Run 1b)

Appendix D

Combining Neural Networks

The output of a neural net which is trained on a signal (S) and background (B) can be written as:

$$O(x) = \frac{S(x)}{S(x) + B(x)} \tag{D.1}$$

Let there be three neural networks (NN1, NN2, NN3) trained on same signal and three separate backgrounds. NN1 trained on signal (S) and Background (B_1) and its output is

$$O_{NN1} = \frac{S}{S + B_1} \tag{D.2}$$

Similarly the second network is trained on on signal (S) and Background (B_2) and third is on on signal (S) and Background (B_3) giving outputs of:

$$O_{NN2} = \frac{S}{S + B_2} \tag{D.3}$$

$$O_{NN3} = \frac{S}{S + B_3} \tag{D.4}$$

Combining Equation D.2– D.4 gives:

$$\frac{1}{O_{NN1}} + \frac{1}{O_{NN2}} + \frac{1}{O_{NN3}} = \frac{3S + B_1 + B_2 + B_3}{S} \tag{D.5}$$

or

$$\frac{1}{3} \times (\frac{1}{O_{NN1}} + \frac{1}{O_{NN2}} + \frac{1}{O_{NN3}}) = \frac{S + \frac{1}{3} \times (B_1 + B_2 + B_3)}{S} \tag{D.6}$$

which can be further be rewritten as

$$\frac{3}{\frac{1}{O_{NN1}} + \frac{1}{O_{NN2}} + \frac{1}{O_{NN3}}} = \frac{S}{S + \frac{1}{3} \times (B_1 + B_2 + B_3)} \tag{D.7}$$

Now the right hand side of Equation D.7 is equalivalent to right hand side of the Equation D.1. This implies that the Equation D.7 represent a neural network trained on signal (S) and backgrounds (B_1, B_2, B_3). Thus, the three neural networks can be combined algebraically into one neural net O_{NN}^{comb}, such that.

$$O_{NN}^{\text{comb}} = \frac{3}{\frac{1}{O_{NN1}} + \frac{1}{O_{NN2}} + \frac{1}{O_{NN3}}} \tag{D.8}$$

Bibliography

[1] Murry Gell-Mann, Phys. Lett. **8**, 214 (1964).

[2] S. Glashow, Nucl. Phys. **22**, 579 (1961).
A. Salam and J.C. Ward, Phys. Lett. **13**, 168 (1964).
S. Weinberg, Phys Lett. **19**, 1264 (1967).

[3] UA1 Collaboration, Phys. Lett. B **122**, 103 (1983).
UA2 Collaboration, Phys. Lett. B **122**, 476 (1983).
UA1 Collaboration, Phys. Lett. B **126**, 398 (1983).
UA2 Collaboration, Phys. Lett. B **129**, 130 (1983).

[4] DØ Collaboration, Phys. Rev. Lett. **74**, 2632 (1995).
CDF Collaboration, Phys. Rev. Lett. **74**, 2626 (1995).

[5] J. Ellis, Int. J. Mod. Phys. **A12**, 5531 (1997).
G. Altarelli, R. Barbieri and F. Caravaglios Int. J. Mod. Phys. **A13**, 1031 (1998).

[6] F. Wilczek, Int. J. Mod. Phys. **A13**, 863 (1998).

[7] DØ Collaboration, Phys. Rev. Lett. **79**, 1197 (1997).
DØ Collaboration, Phys. Rev. D **58**, 52001 (1998).

[8] M. L. Perl *et al.*, Phys. Rev. Lett. **35**, 1489 (1975).

[9] S. W. Herb *et al.*, Phys. Rev. Lett. **39**, 252 (1977).

[10] C. Berger *et al.*, Phys. Rev. Lett. **76**, 243 (1978).

[11] W. Bartel *et al.*, Phys. Rev. Lett. **146**, 437 (1984).

[12] J. F. Donoghue, E. Golowich, B. R. Holstein, "Dynamics of the Standard Model", Cambridge University press, (1992).

[13] G. L. Kane and M. E. Peskin, Nucl. Phys. B **195**, 29 (1982).

[14] ARGUS Collaboration, Phys. Lett. B **192**, 245 (1987).
CLEO Collaboration, Phys. Rev. Lett. **71**, 1680 (1993).

[15] L. Montanet *et al.*, Phys. Rev. D **50**, 1433 (1994).

[16] L. Montanet *et al.*, Phys. Rev. D **50**, 1433 (1994).

[17] Results from DØ and CDF combined top mass calculations web page, http://www-cdf.fnal.gov/Phys.ics/new/top/results/mass/combine_top_mass.html

[18] T. Hill and S. Parke, Phys. Rev. D **49**, 4454 (1994).

[19] E. Eichten and K. Lane, Phys. Lett. B **327**, 129 (1994).

[20] S. Choi, PhD thesis, "Spin correlations in top-antitop production", Seoul National University, Korea, (1999).

[21] A. Heinson *et al.*, Phys. Rev. D **56**, 3114 (1997).

[22] P. Savard, CDF Collaboration, "Single Top and Top Quark Properties with CDF", FERMILAB-CONF-99/174-E (1999).

[23] J. Collins *et al.*, Nucl. Phys. B **263**, 7 (1986).

[24] Babcock, D. Sivers and S. Wolfram, Phys. Rev. D **18**, 162 (1978).
M. Gluck, J. Owens and E. Reya, Phys. Rev. D **17**, 2324 (1978).
H. Georgi, S. Glashow, M. Machacek and D. Nanopoulos, Ann. Phys. **114**, 273 (1978).
B. Combridge, Nucl. Phys. B **151**, 429 (1979).

[25] P. Nason, S. Dawson, R. Ellis, Nucl. Phys. B **303**, 607 (1988).
G. Altarelli, M. Diemoz, G. Marinelli and P. Nason, Nucl. Phys. B **308**, 724 (1988).
W. Beenakker, H kuijf and W. van Neerven and J. Smith, Phys. Rev. D **40**, 54 (1989).
W. Beenakker *et al.*, Nucl. Phys. B **351**, 507 (1991).
R. Ellis, Phys. Lett. B **259**, 492 (1991).
M. Mangano, P.Nason and G. Ridolfi Nucl. Phys. B **373**, 295 (1992).

[26] E. Laenen, J. Smith and W. van Neerven, Phys. Lett. B **321**, 254 (1994).

[27] E. Berger and H. Contopanagos, Phys. Lett. B **361**, 115 (1995).
E. Berger and H. Contopanagos, Phys. Rev. D **54**, 3085 (1996).
E. Berger and H. Contopanagos, Phys. Rev. D **57**, 253 (1998).

[28] S. Catani, M. Mangano, P. Nason and L. Trentadue, Phys. Lett. B **378**, 329 (1996).
R. Bonciani, S. Catani, M. Mangano and P. Nason, Nucl. Phys. B **529**, 424 (1998).

[29] S. Frixione, M. Mangano, P. Nason and G. Ridolfi, "Heavy Flavors II", World Scientific Publications (1997).

[30] A. Martin, R. Roberts and W. J. Stirling, Phys. Lett. B **306**, 145 (1993).
A. Martin, R. Roberts and W. J. Stirling, Phys. Lett. B **387**, 419 (1996).

[31] D. H. Perkins, "Introduction to High Energy Physics", Addison Wisley Publishing, (1982).

[32] CTEQ Collaboration, MSUHEP-41024.

[33] B. Mele, S. Petrarca and A. Soddu, Phys. Lett. B **435**, 401 (1998).

[34] J. Gunion, H. Haber, G. Kane and S. Dawson, "The Higgs Hunter's Guide", Addison Wisley Publishing, (1990).

[35] E. Smith, PhD Thesis, "Search for Charged Higgs Bosons in Top Quark Decays at DZero", University of Oklahoma, (1999).
CDF Collaboration, Phys. Rev. Lett. **79**, 357 (1997).

[36] P. Bloom, PhD Thesis, "Investigation of Trilinear Vector Boson Couplings through W Boson Pair Production in Dilepton Decay Channels", University of California, Davis, (1998).

[37] DØ Collaboration, Phys. Rev. D **60**, 52003 (1999).

[38] T. Huehn, PhD thesis, "A measurement of bottom quark production in $p\bar{p}$ collisions at $\sqrt{s} =$ 1.8 TeV", University of California, Riverside, (1995).

[39] H. T. Edwards, Ann. Rev. Nucl. Part. Sci, **35**, 605 (1985).
F. T. Cole *et al.*, "A Report of the Design of the Fermi National Laboratory Super-conducting Accelerator", Fermilab internal report (unpublished), (1979).
F. T. Cole *et al.*, "Design Report Tevatron 1 Project", Fermilab Internal report (unpublished) (1984).

[40] DØ Collaboration, Nucl. Instrum. Methods A **338**, 185 (1994).
S. Snyder, "The DØ Detector", DØ internal note 2500 (unpublished), (1995).

[41] J. D. Jackson, "Classical Electrodynamics", John Wiley and Sons, (1975).

[42] S. J. Wimpenny *et al.*, Nucl. Instrum. Methods A **279**, 107 (1989).

[43] C. Brown *et al.*, Nucl. Instrum. Methods A 279, 331 (1989).
J. M. Butler *et al.*, Nucl. Instrum. Methods A 290, 122 (1990).

[44] S. Snyder, Ph.D Thesis, "Measurement of the top quark mass", SUNY at Stony Brook, (1995).

[45] ZEBRA, CERN program library long write up, Q100 and Q101 (1995).

[46] T. Behnke, Ph.D Thesis, "The CDC for the DØ detector", SUNY at Stony Brook, (1989).
D. Pissuto, Ph.D Thesis, "The DØ central tracking performance," SUNY at Stony Brook, (1991).

[47] S. Youssef, Comp. Phys. Comm. **45**, 423 (1987).

[48] M. Narain, "Electron identification in the DØ detector", Proceeding of DPF'92, World Scientific, (1992).
M. Narain, "Electron identification in the DØ detector", DØ internal note 1548 (unpublished), (1992).

[49] U. Heintz *et al.*, DØ internal note 2355 (unpublished), (1994).

[50] U. Heintz *et al.*, "A Likelihood test for the electron ID", DØ internal note 2386 (unpublished), (1994).

[51] J. A. Guida, Proceedings of the 4th International Conference on Advanced Technology and Particle Physics, Italy, (1994).
J. Kotcher, Fermilab Report No. FERMILAB-CONF-95/007-E (unpublished), (1995).

[52] C. Gerber *et al.*, "Muon momentum determination", DØ internal note 2140 (unpublished), (1994).

[53] Bhatnagar *et. al*, "Study of Hadron Punch-through in Dzero", DØ internal note 1858 (unpublished), (1993).

[54] E. Gallas, "The MTC Package", DØ internal note 2066 (unpublished), (1994).
E. Gallas, "Testing MTC", DØ internal note 2068 (unpublished), (1994).

[55] UA1 collaboration, Phys. Lett., B **123**, 115 (1983).

[56] J. Yu, PhD Thesis, "Determination of the Strong Coupling Constant and a Test of Perturbative QCD Using W + jets Processes in the DØ detector", SUNY at Stony Brook, (1993).
A. J. Milder, PhD thesis, "Dijet Angular Distributions at Using the DØ detector", University of Arizona, (1993).

[57] R. Kehoe and R. Astur, DØ internal note 2052, 2908 (unpublished), (1994,96)

[58] J. H. Cochran, PhD Thesis, "Search for the truth in the eμ channel", SUNY at Stony Brook, (1993).
V. Bhatnagar, PhD Thesis, "Search for the top quark in the $e\mu$ channel", Panjab University at Chandigarh, (1998).

[59] C. Peterson and T. Rognvaldsson, "An introduction to Artificial Neural Networks", 1991 CERN school of computing, (1991).

[60] Eunil Won, PhD Thesis, "Top quark production in multijet final state", University of Rochester, (1996).

[61] Harpreet Singh *et. al*, "Top via eμ using neural nets (1992-93 data)", DØ internal note 3071 (unpublished), (1996).

[62] P. Bhat, "Search for the Top Quark at DØ Using Multivariate Methods", FERMILAB-Conf-95/211-E, (1995).

[63] R. Beale and T. Jackson, "Neural Computing: An Introduction", Adam Hilger, (1990).

[64] M. Nelson and W. Illingworth, "A practical guide to neural networks", Addison Wesley Publishing, (1991).

[65] Harrison Prosper, "Some mathematical comments on feed forward neural nets", DØ internal note 1606 (unpublished), (1994)

[66] J, Hertz, A, Krogh and R. Palmer, "Introduction to the theory of Neural Computation", Addison Wesley Publishing, (1990).

[67] D. Rumelhart, G. Hinton and R. Williams, "Learning internal representations by error propagation", MIT press, (1986).

[68] C. Peterson, T. Rognvaldsson and L. Lonnblad, "JETNET 3.0 A versatile Artificial Neural Network Package", Lund University Preprint, (1993).

[69] Bhat P. and A. Mirles, "Studies of the effect of architecture and training parameters on the performance of neural networks", DØ internal note 2669 (unpublished), (1995).

[70] J. Linnemann, "Triggering the DØ Experiment", Proceeding of DPF'92, (1992).

[71] J. Bantly *et. al*, "Improvement to the DØ Luminosity Monitor Constant", DØ internal note 2544 (unpublished),(1995).

[72] S. J. Wimpenny, "The TOP-LEPTONS Analysis Package (Version 6.01)", DØ internal note 2144 (unpublished), (1994).

[73] S. J. Wimpenny, B. Kehoe, M. Narain, J. Thompson and P. Quintas, Bad Run Rcp File located at /d0sgiucr2/exports/data0/jc/shappy/topdilep2/bad_run.rcp (version 3.0), (1996).

[74] J. Butler *et. al*, "Measurement of the Top Quark production cross section using lepton+ jets events", DØ internal note 2978 (unpublished), (1995).

[75] J. Cochran, "eμ truths in Run 1", DØ dilepton web page (1997), http://www-d0.fnal.gov/~cochran/d0private/topemu.html

[76] S. J. Wimpenny, "Muon efficiency corrections for single top analyses", DØ internal note 3282 (unpublished), (1997).
M. Mason and S. J. Wimpenny, "Studies of Mu-Smear corrections factors for the Run 1b/c single top analysis", DØ internal note 3281 (unpublished), (1997).

[77] F. Paige and S. Protopopescu, Proceedings Summer Study on the Phys.ics of SSC, Snowmass Colorado, (1986).

[78] T. Sjostrand, PYTHIA and JETSET Physics and Manual, CERN TH 6488/92, (1992).

[79] G. Marchesini *et al.*, Comp. Phys. Comm. **67**, 465 (1992).

[80] G. Altarelli and G. Parisim Nucl. Phys. B **126**, 298 (1977).

[81] R. Field and R. Feynman, Nucl. Phys. B **136**, 1 (1978).

[82] B. Anderson, G. Gustafson, G. Ingelman and T. Sjostrand, Phys. Rep. **97**, 33 (1988).

[83] R. Brun and F. Carminati, CERN program library long writeup, W5013, (1993).

[84] W. Dharmaratna, R. Raja and C. Stewart, "DØ shower library", DØ internal note 1730 (unpublished), (1993).

[85] T. Diehl and P. Quintas, "The MU-SMEAR package documentation", (1994).

[86] DØ Collaboration, Phys. Rev. Lett. **75**, 1456 (1995).

[87] J. McKinley, PhD Thesis, "A Measurement of the Inclusive Drell-Yan e+e- Cross Section in the Invariant Mass Range 30-60 GeV/c^2 from $p\bar{p}$ Collisions at $\sqrt{s}$. = 1.8TeV", Michigan State University, (1996).

[88] DØ Collaboration, "Determination of the Absolute Energy Scale in the DØ calorimeters", Fermilab-Pub-97/330E, hep-ex/9805009 (1997).

[89] DØ Collaboration, Phys. Rev. D **60**, 57001 (1999).

[90] H. Greenlee's Web Site, "http://www-d0.fnal.gov/~greenlee/d0_private/top2_41_run1.ps"

[91] E. Varnes, PhD Thesis, "Measurement of the top quark mass, PhD Thesis", University of California, Berkeley, (1997).

[92] M. Kruse, PhD Thesis, "Observation of top quark pair production in the dilepton decay channel from proton-antiproton collisions at $\sqrt{s} = 1.8$ TeV, CDF PhD thesis", Purdue University, (1996).

[93] Particle Data Book, Review of Particle Physics, Physics Review D54, (1996).

About the Author

Harpreet Singh was born in Amritsar, India on February 26, 1971. After living in Amritsar for about 2 years, his parents moved to Chandigarh, the City Beautiful, where his father was working in the technical staff at the Panjab University. Being from the family of engineers, he was always fascinated by science and started building electronic projects in the school. Harpreet attended Panjab University-Chandigarh, earning his B.Sc.(Honors School) and M.Sc.(Honors School) in Physics with specialization in Electronics. He was University swimming champion for four years successively and also held positions in National tournaments. He started his research career in experimental high energy physics with Panjab University and later moved to University of California, Riverside where he did his doctoral dissertation.